Università degli Studi di Cagliari

DOTTORATO DI RICERCA

INGEGNERIA INDUSTRIALE

Ciclo XXXI

TITOLO TESI

METHODOLOGIES FOR THE INVESTIGATION OF THE MECHANICAL BEHAVIOUR OF POLYVINYLCHLORIDE FOAMS

Settore/i scientifico disciplinari di afferenza

ING-IND/14

Presentata da: FRANCESCA CONCAS

Coordinatore Dottorato: FRANCESCO AYMERICH

Tutor: ANTONIO BALDI

Esame finale anno accademico 2017 – 2018

Tesi discussa nella sessione d'esame Gennaio 2019

Università degli Studi di Cagliari

DOTTORATO DI RICERCA

INGEGNERIA INDUSTRIALE

Ciclo XXXI

TITOLO TESI

METHODOLOGIES FOR THE INVESTIGATION OF THE MECHANICAL BEHAVIOUR OF POLYVINYLCHLORIDE FOAMS

Settore/i scientifico disciplinari di afferenza

ING-IND/14

Presentata da: FRANCESCA CONCAS

Coordinatore Dottorato: FRANCESCO AYMERICH

Tutor: ANTONIO BALDI

Esame finale anno accademico 2017 – 2018

Tesi discussa nella sessione d'esame Gennaio 2019

Contents

Abstract

Closed-cell polyvinylcloride (PVC) foams are used as core materials for sandwich composites in challenging applications such as wind turbine blades, in which a wide range of multiaxial loads are involved. By a review of the relating literature, still more analyses are needed for a throughout understanding of the mechanical behaviour of PVC foams and particular attention has to be dedicated on the concerning methodologies.

The present work aims to give a contribution in this field by the execution of a great amount of experimental tests on different types of closed-cell PVC foams.

The first part of this work focuses on the study of the compressive properties of PVC foams and, more precisely, several methods for the determination of the compressive modulus are described and conducted. Such methods are closely linked to the procedure for the strain measurement, that is achieved either by the digital image correlation or by the output displacement data of the universal testing machine, which give back the local strains and the global strains, respectively.

The second part addresses the multiaxial behaviour of PVC foams by proposing a yield function which has been successfully applied for other materials. The deformation mechanism under multiaxial loading has been analysed through the three-dimensional digital image correlation performed by a new 8-camera system. The enhancement of this method is described in great detail and the resulting deformation bands are explained for each loading case.

The present work focuses on the understanding of the mechanical behaviour of the material as well as on the application of methodologies.

Acknowledgements

I wish to thank my supervisor Prof. Ing. Antonio Baldi for his advice during my PhD and for leading me into the experimental activity.

I wish to thank Prof. Ing. Francesco Aymerich, my second supervisor and coordinator of the PhD course for his support and his contribution to my research.

I wish to thank PD Dr.-Ing. Dr. rer. nat. Anne Jung and Prof. Dr.-Ing. Stefan Diebels for allowing me to be a guest PhD student at the Chair of Applied Mechanics, Saarland University. Thanks to their guidance, this period has been crucial for my growth as a researcher.

I am grateful to the staff and the colleagues at the Chair for their helpfulness and kindness.

List of Figures

List of Tables

List of Abbreviations

DIC: **D**igital **I**mage **C**orrelation

DSP: **D**igital **S**peckle **P**hotography

FEA: **F**inite - **E**lement - **A**nalysis

IP: **I**n - **P**lane

LVDT: **L**inear **V**ariable **D**isplacement **T**ransducer

PMI: **P**oly**M**ethacryl**I**mid

PVC: **P**oly**V**ynil**C**hloride

ROI: **R**egion **O**f **I**nterest

UTM: **U**niversal **T**esting **M**achine

TT: **T**hrough - **T**hickness

Chapter 1

Introduction and motivation

1.1 Applications of the material and motivations of the work

Sandwich composites meet demanding requirements for many industrial applications, in which features such as higher strength and lower weight are needed. A sandwich composite is characterised by the presence of two skin layers, which are connected to the upper and the lower side of a thick lightweight core material [17, 98]. Different types of core were reported for sandwich composites [1]:

- honeycomb
- cross-banded
- corrugated
- waffle-type
- foams
- woods (e.g. balsa wood)

The preference of a specific core type rather than another type is linked to the application field. Mechanical properties of sandwich composites depend on the intrinsic characteristics of the core material as well as to the manufacturing procedure and, more precisely, which method is used to bond skins to the core [31]. A sandwich structure can be equalised to an I-beam [17, 37]. By taking into account a flexural loading, skins of the sandwich are set at the upper and lower side of the beam, in order to bear the highest tensile and compressive loads, whereas the core

at the centre carries out-of-plane shear and compression loads [28]. A typical failure case for cores is the "core shear failure" [106]. As can be seen from the table in Fig. 1.1, the bending stiffness and strength of the sandwich composite depend on the thickness of its core.

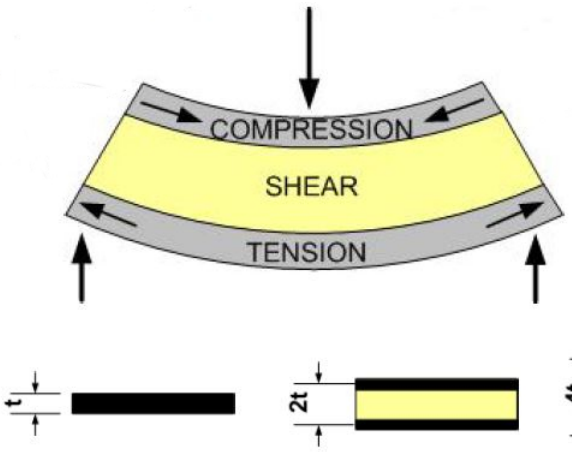

Weight	**1**	⟶	**~1**	⟶	**~1**
Bending stiffness	**1**	⟶	**~12**	⟶	**~48**
Bending strength	**1**	⟶	**~6**	⟶	**~12**

Figure 1.1: Loads occurring in a sandwich panel subjected to bending loads and increase of the bending stiffness and strength linked to the sandwich thickness [7].

As stated in the *Composite Materials Handbook* [1], foams offer advantages such as a uniform bonding layer between skins and core and "flexibility in manufacturing", in comparison with other core types.
According to Zenkert and Bäcklund [122], polymer foams were used for any application but not in the aeronautics and the aerospace. However, Dyson [40] reported the example of a helicopter rotor blade made by sandwich composites with a PVC foam core. Herbeck et al. [54] described the usage of foams for aerospace applications in terms of the structural performance as well as manufacturing procedures. They reported the PVC foam to be "comparably inexpensive", having "low moisture absorption and great impact strength". Furthermore, manufacturers developed polymeric foams specifically for the aeronautic industry [35, 41]. The Divinycell® HT grade is a PVC foam [70] dedicated to aerospace applications [35]. PVC foams find their main application in sandwich composites for the marine industry [5, 15, 48]. Veazie et al. [113] investigated the effect of seawater, high temperatures and humidity in the fracture of the PVC foam core and the interface between face and core. Toftegaard and Lystryp [108] presented a study on T-joints

for naval ship. T-joints having PVC foam as core were analysed by means of the FEA and experimental tests. According to Imielińska [58], PVC foams have a remarkable impact strength, which is an appreciated feature for applications such as boat hulls. A sandwich composite with a PVC foam core and glass-fibre polyester laminates is mentioned again by Imielińska [58] as a "typical" sandwich composite in the shipbuilding industry. PVC foams exhibit a better conservation of mechanical properties by immersion in seawater [91] in comparison with the balsa wood, which is also widely used because of its lower price [5]. Sirikuk et al. [96] evaluated the degradation of the mechanical behaviour of a PVC foam subjected to torsion and tension under the effect of seawater. May-Pat and Avilés [79] performed an immersion of a PVC foam both in distilled water and sea water for 6 and 12 months. They investigated the absorption of water on the foam, the changing on the microstructure (in terms of cell sizes) and the detrimental effect of water on mechanical properties.

Another typical application of PVC foams concerns wind turbine blades [6, 23, 107]. In Fig. 1.2 a cross-section of a blade is depicted, in which parts made of foam are highlighted. It can be seen that both the aerofoil contour and the main spar are made by sandwich composites. Balsa wood [80, 114] is also used as alternative to foams. A comparison between balsa wood and polymeric foams was done by Sloan [97], that weighted advantages and disadvantages of the different core materials. Furthermore, a list of the literature dealing with the confrontation of core materials for wind turbine blades was presented by Stoll [100].

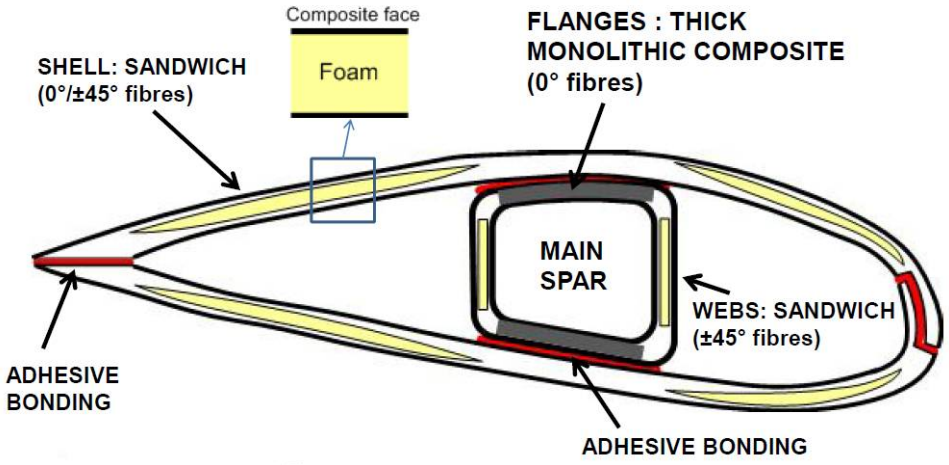

Figure 1.2: Schematic of a wind turbine blade cross-section [7].

Due to the gradually lower availability of fossil fuels and issues concerning the environmental pollution, engineers and scientists have an increasing interest

in improving performances and reducing costs and maintenance of plants for the production of energy from renewable sources, e.g. the wind. Hence, the present Section focuses on design concerns of PVC foams in wind turbine blades.

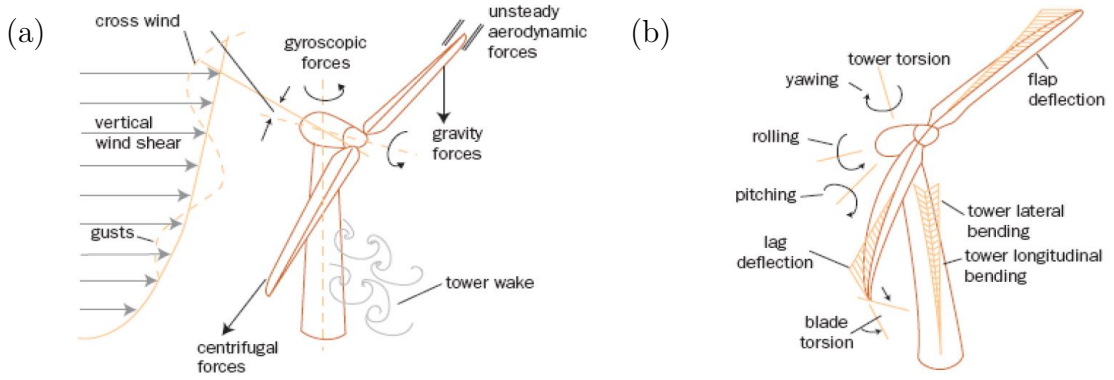

Figure 1.3: Wind energy towers, blades and nacelles undergo different loads (a) and movements (b) [55].

By taking into account the case of a wind turbine rotor (Fig. 1.3), the PVC foam core would be subjected to a wide range of loads and movements. Hence, the knowledge of the deformation mechanism should not be limited to shear and compressive loading, but must include combined shear-compressive loads, as well as tensile loading and combined shear-tensile loading. The direction of loads occurring in sandwich composites of wind turbine blades has been addressed by many works, with a focus on the core. Taher et al. [106] mentioned how the core can be subjected to normal loads (tensile and compressive loads), that would eventually have a greater influence on the core failure than shear loads. Normal loads occur near supports and in case of geometrical discontinuities [106]. Further multiaxial loads arise in case of a tip deflection of the blade and the Brazier effect on the main spar of the blade [60, 71]. The Brazier effect [14] concerns the resulting tensile and compressive stresses in a thin-walled tube, which undergoes a bending loads. Bending loads lead to a flattening of the tube section [95]. A schematic representation of this issue is depicted in Fig. 1.4.
Arising of multiaxial loads is linked also to the size of the blade. More precisely, wind turbine blades with a greater size would be subjected to more complex loads than small-sized blades [20, 59].

Grid-scoring is one of the available procedures for allowing the core material to be inserted in a curved mould for the manufacturing of the aerofoil [50]. This procedure involves the insertion of a stiff resin grid, which would lead to local stress concentrations [73]. Few images of the grid-scored foam panel and its application

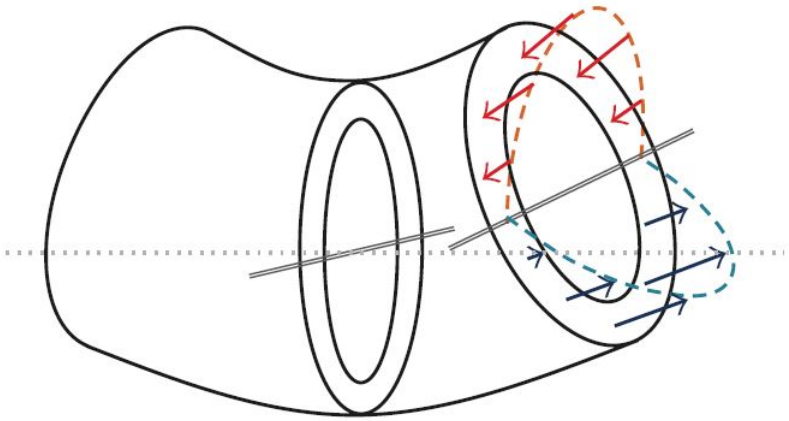

Figure 1.4: Schematic of the Brazier effect [95].

on the aerofoil are shown in Fig. 1.5. All above-mentioned considerations reinforce the urgency of a deep understanding of the PVC foams' multiaxial response. Such an investigation needs to be focused on the prediction of failure. That could be achieved by doing:

- several tests on specimens for gathering failure data,
- searching a suitable failure function to be adapted to collected failure data,
- inspecting deformation bands.

Based on the loading case, the failure of the foam may involve either only the yielding or both yielding and fracture.

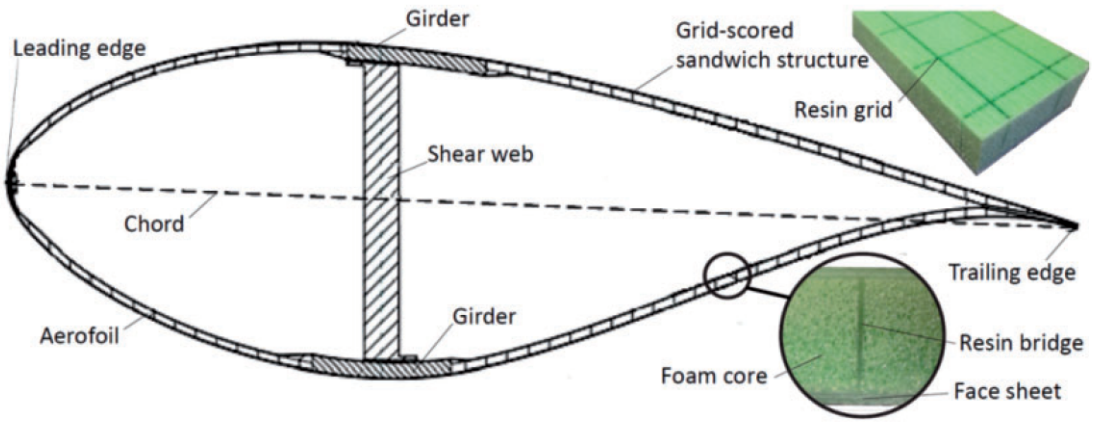

Figure 1.5: Schematic of a wind turbine blade cross-section, with magnification of a detail made by a grid-scored foam [73].

The inspection of deformation bands is crucial, since they are useful for the prediction of the failure in several loading cases. Deformation bands are detectable by means of full-field optical methods. One of the most popular method in the current times is the DIC[1] (Digital Image Correlation). It appears as a well-suited technique for measuring strains on foams, mainly due to their intrinsic structure that would impede the application of strain gauges [62]. More details on the DIC method can be found in the work of Sutton et al. [101]. A large amount of literature has been dedicated to polymeric foams, concerning the multiaxial testing or the strain measurement by the DIC method. Further details on the state-of-the-art for multiaxial testing of PVC foams are mentioned in Section 2.3. Nonetheless, based on the knowledge of the author, only two works ([57, 106]) have been focused so far on using both multiaxial testing and strain measurement by the DIC for the mechanical characterisation of PVC foams. Moreover, none of the above-mentioned works covered a wide range of loads. For example, results of combined tensile-shear tests were not reported by Taher et al. [106] and Hoo Fatt et al. [57], although their test rigs, that were inspired by the Arcan concept [3], were theoretically able to perform such tests.

The application of the DIC for the mechanical characterisation of PVC foams can be efficient or not depending on the features of the studied foams as well as the size and the shape of the related specimen. More precisely, if the specimen undergoes displacements in a direction perpendicular to the plane surface exposed to the camera, the related DIC strain measurement cannot be considered reliable. Jin et al. [62] presented the usage of the 3D-DIC with a 2-camera system for obtaining strain maps during the compression test of a closed-cell polyurethane foam as cubic specimen. They avoided the application of the DIC with a single camera because the reliability of strain measurements by the DIC is strictly linked to the absence of out-of-plane displacements [62]. Nevertheless, the usage of a single camera for performing the DIC on cubic specimens during compression tests has been reported by several works for PVC foams (e.g. [123]), in order to measure strains or also for the subsequent calculation of the compressive modulus, although the several methods available for measuring strains leads to greatly different values of the compressive modulus [88]. Hence, a comparison of the methods for the calculation of the compressive modulus is needed by assessing the contribution of different factors,

[1] In the present work, the nomenclature "DIC" is referred by the author to the "two-dimensional digital image correlation". Whereas the three-dimensional digital image correlation is referred as "3D-DIC"

e.g. the portion of the stress-strain curve considered or rather the size and the position of the ROI (Region Of Interest).
Thus, it is evident that more investigations have still to be done on PVC foams with a particular attention on the set of methods. Two main issues emerge from the aforesaid considerations:

- the prediction of the failure on PVC foams under a multiaxial stress state and
- the advantageous application of the DIC for the determination of the compressive modulus.

1.2 Outline and objective of the work

The present work aims to bring a contribution on the current state-of-the-art of the mechanical characterisation of PVC foams and, particularly, to find a solutions for the issues presented in the previous Section. The structure of the present work is described below.
In Chapter 2 details on the studied PVC foams are listed, including descriptions of the trade name and manufacturing procedures. The importance of the investigation of the microstructure of the material is presented by mentioning the scaling separation concept. The microstructure of the material is inspected and compared with analogous studies on the same material, which were previously published. Through the microstructure of the foam, the orthotropic behaviour of the foam is explained. Finally, an overview of the literature dealing with the compressive and multiaxial testing of PVC foams is described. Because of the great amount of available fixtures, some works concerning the multiaxial testing of metal foams are mentioned as well.
Chapter 3 describes the research activity at the Department of Mechanical, Chemical and Materials Engineering, University of Cagliari (Italy) and addresses the problem of the determination of the compressive modulus of the PVC foam by the DIC method. The knowledge of the compressive properties is fundamental for a preliminary design of sandwich composites. In the present work, compression tests are performed on cubical specimens of different nominal densities of the PVC foam, i.e. Divinycell® HP60 and HP160. Compressive moduli are evaluated for both main directions of the foam. Strains are obtained by using the DIC method and the calculation from the actuator stroke as registered by the UTM. Weaknesses in currently-accepted methods for the calculation of the compressive modulus in PVC

foams are highlighted by

- the elimination of the compliance contribution given by the UTM and
- the strain measurement by considering several ROIs, which are variously positioned on the specimen surface exposed to the camera.

Chapter 4 describes the research activity at the Chair of Applied Mechanics, Saarland University (Lehrstuhl für Technische Mechanik, Universität des Saarlandes, Germany), which is summarised also in the work of Concas et al. [23] and focuses on a throughout multiaxial investigation of the Divinycell® HP100 PVC foam grade. The procedure includes:

- the description of an 8-camera system for the execution of the 3D-DIC with relating issues;
- the execution of uniaxial tests in either displacement or rotational control of the actuator: tension, compression and torsion for determining respective failure stresses;
- the execution of tensile and compression tests in load control of the actuator up to a percentage of the previously calculated failure loads and the subsequent superposition of torsion. Failure stresses are obtained also for such loading cases;
- the collecting of failure data in the invariants plane and the presentation of a failure function to be adapted to failure data;
- discussion on strain maps and the arising of deformation bands, which are obtained by the 3D-DIC

Chapter 5 expresses the main results pertaining to the previous chapters.

Chapter 2

Structural and mechanical characterisation of the material

2.1 Structural characterisation

The nomenclature "cross-linked PVC foam" refers actually to a combination of polyurea and PVC [37], i.e. an interpenetrating polymer network [29]. The present work focuses on the Divinycell® HP100 PVC foam core grade (DIAB, Laholm, Sweden), which were supplied as panels with a thickness of 40 mm. According to a communication from the manufacturer, the nomenclature HP means "High Performance", since it is an improved version of the general purpose H grade. Further PVC foam grades of Divinycell® are the HPC [33, 56] and the already mentioned HT. A great amount of scientific works was dedicated to the investigation of mechanical properties of the H grade, since most of the literature cited in the following two sections deals with the analysis of the H grade, whereas much less works were focused on the HP grade. The number on the nomenclature refers to the nominal density of the foam, e.g. 100 kg/m^3 for the Divinycell® HP100 foam.
Manufacturing of cross-linked PVC foams are distinguished in two main procedures: extrusion and moulding [94]. More details concerning the extrusion method can be found in the works of Lee [74] and Sauceau et al. [92], whereas Shi et al. [94] presented a method for producing cross-linked PVC foams by moulding.
Previously published works (e.g. [19, 51]) demonstrated how the morphology of cells and pores is paramount for determining mechanical properties of the foam [120]. This feature leads to the research of manufacturing methods for generating a particular cell morphology and for obtaining subsequently the sought characteristics [120]. The cell morphology and mechanical properties of the specimen are linked

by means of the scaling separation concept or macro-meso-micro-principle (MMM principle), for which a description can be found in the works of Jung et al. [65, 66, 67]. Further details can be found in the work of Hashin [53]. From Fig. 2.1, the above-mentioned three scales are represented. Investigations on the macroscale are linked to the specimen size and shape. The mesoscale involves a group of few cells or pores, whereas the microscale concerns the single cell or pore, as well as the single wall or strut [67].

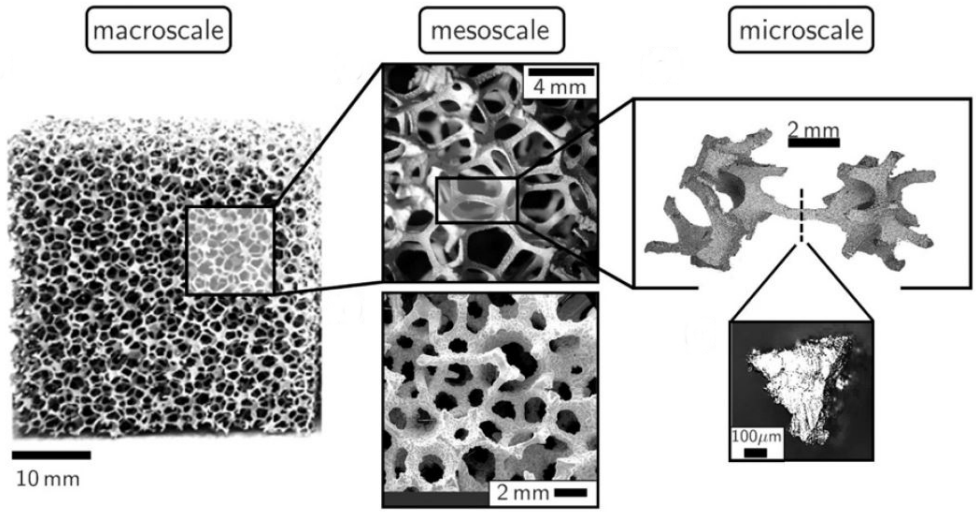

Figure 2.1: The scaling separation on metal foams [67].

It is widely known that PVC foam panels are orthotropic because of manufacturing processes. Hence, properties of the material are related to the two following directions [104, 106, 123], which are depicted in Fig. 2.2 (a):

- *through-thickness*
- *in-plane*

The *through-thickness* direction is mentioned also as *out-of-plane* in other works [16, 43, 44, 81].

In order to evaluate properly mechanical properties of the material, an inspection of the lowest scale, i.e. the microscale is needed. Based on the knowledge of the author, a throughout inspection of the Divinycell® HP foam microstructure, i.e. measuring the cells' size for four different nominal densities (60, 100, 200 and 250 kg/m^3), has been done so far only by Colloca et al. [22] and Luong et al. [77].

An analysis of the microstructure of the Divinycell® HP100 foam has been performed by usage of a digital microscope VHX-500 F (Keyence Ltd., Osaka, Japan). Images have been acquired from two planes:

- a plane perpendicular to the in-plane direction, in order to inspect cells in the through-thickness direction and
- a plane parallel to the in-plane direction, for inspecting cells in the in-plane direction

in order to quantify the elongation of cells. For this purpose, a piece of foam has been cut by a band saw along the above-mentioned planes. The acquired images are shown in Fig. 2.2 (b)-(c).
From Fig. 2.2 (a), three characteristic sizes are identified:

- a: longest size of cells, as visible from a piece of foam cut perpendicular to the in-plane direction;
- b: shortest size of cells, as visible from a piece of foam cut perpendicular to the in-plane direction;
- c: size of cells, as visible from a piece of foam cut parallel to the in-plane direction, in which no elongation of cells is visible.

20 measurements of each characteristic size have been done for statistics. Subsequently, average values and standard deviations are calculated and listed in Table 2.1.

characteristic size	measure mm		
a	568.07	±	144.65
b	344.43	±	106.67
c	334.96	±	83.30

Table 2.1: Average values and standard deviations of the characteristic sizes measured on 20 cells by the microscope, according to Concas et al. [23].

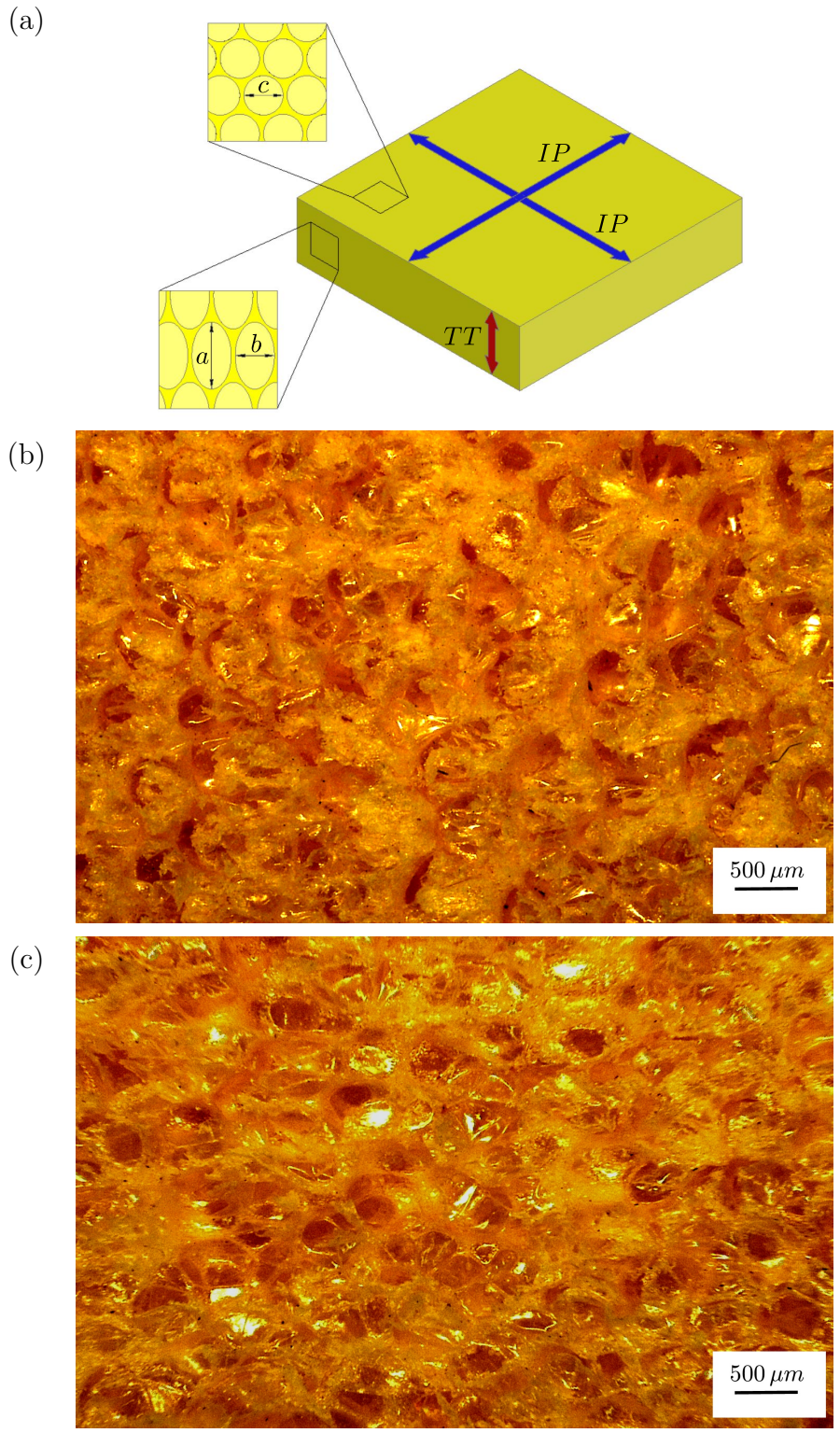

Figure 2.2: Schematic of a panel with magnification of the different cell morphologies along the two main directions (a), images obtained by the digital microscope of a foam piece cut by a band saw along the in-plane (IP) (b) and the through-thickness (TT) (c) direction. All images are taken from Concas et al. [23]

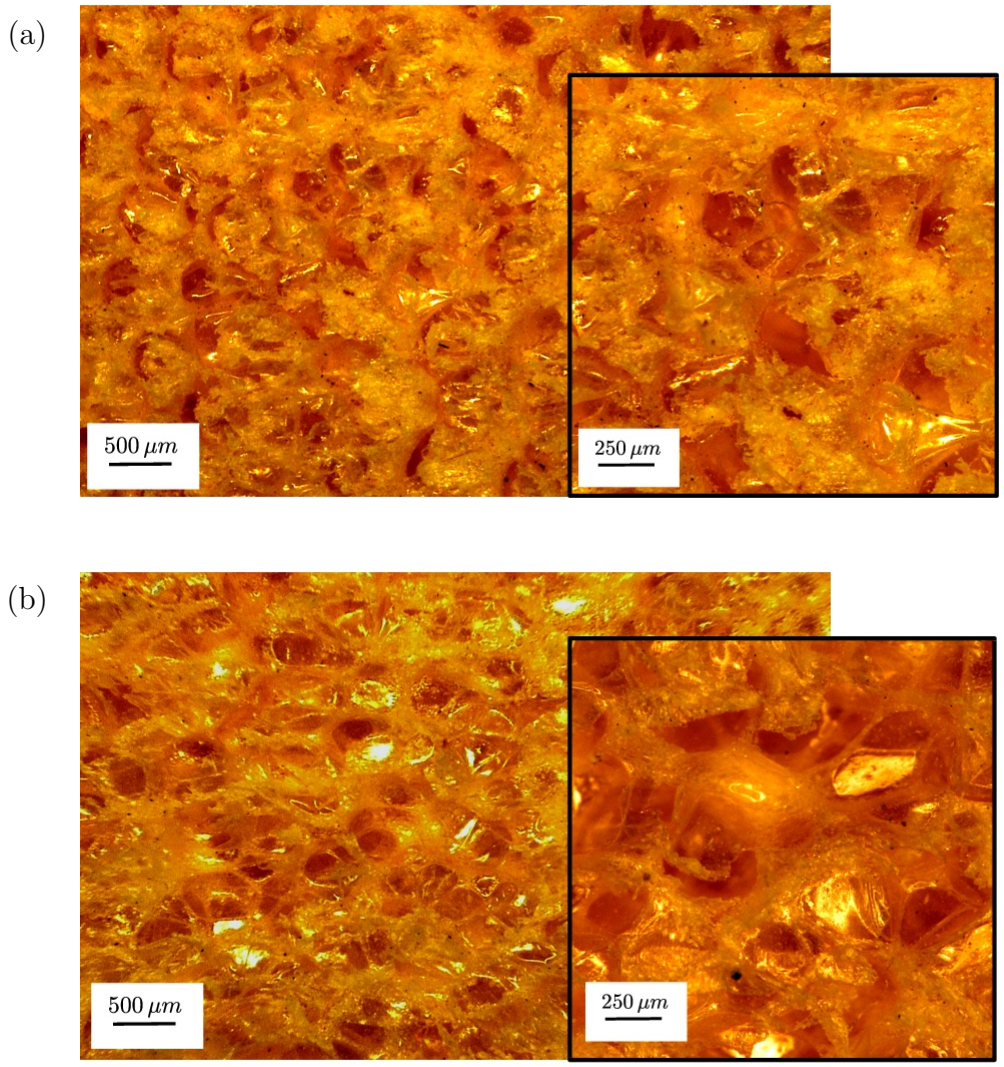

Figure 2.3: Magnification of images obtained by the microscope in the in-plane (a) and the through-thickness (b) direction. All images are taken from Concas et al. [23]

Colloca et al. [22] and Luong et al. [77] did not consider the elongation of cells, then only a characteristic size for each foam density is reported. Mean values and the corresponding standard deviations of the characteristic sizes b nd c are consistent with values obtained by Colloca et al. [22]. The average value of the characteristic size a is less than twice the other two characteristic sizes. This feature is consistent with the inspection of the Divinycell® H100 foam, as performed by Zhang et al. [123]. Furthermore, the characteristic size a is within the range reported by Zhang et al. [123] for the length of cells in the through-thickness direction.

Fig. 2.3 shows the magnifications of cells done by the digital microscope. It is evident the difficulty in distinguishing the cells' contours. Fig. 2.3 (a) depicts cells parallel

to the foam panel surface (in-plane) and cut by a band saw. The walls of the cells tend to bend up to cover the cells cavities. Whereas in Fig. 2.3 (a) it can be seen the elongated cells in the through-thickness direction, in which the identification of cells is made difficult by the high reflectance of their cavities.

2.2 Uniaxial compression testing of the material

Great attention had been paid to the compressive behaviour of PVC foams and factors, which influence their main compressive properties, i.e. the peak yield stress and the compressive modulus. Particularly the estimation of peak yield stresses and compressive moduli is mostly influenced by:

- the chemical structure of the PVC [61, 76];
- the nominal density;
- the direction, in which the foam is loaded, i.e. orthotropy of foams.
- the strain rate;
- the method for the strain measurement and related uncertainties.

The method for measuring strains does not affect obviously the determination of the peak yield stress but only the calculation of the compressive modulus. It is the main topic of Chapter 3. A brief summary on the scientific literature dealing with the compressive characterisation of PVC foams is reported below.
In Lim et al. [76], the morphology and the compressive properties of linear and cross-linked PVC foams are compared. Different densities for both types were taken into account. Furthermore, the influence of water during compression testing of foams was investigated. Another study on the chemical structure of PVC foams and the relating influence on the mechanical response was recently presented by Jiang et al. [61]. They varied the content of epoxy resin in the cross-linked PVC foam matrix and analysed the consequent influence on the tensile, compressive and shear mechanical parameters.
Caliri Jùnior et al. [16] performed compression tests on Divinycell® H60 foams in the through-thickness and the in-plane directions. Among other topics, their work disclosed that the method for measuring displacements could determine the compressive modulus value with a great deviation. More precisely, Caliri Jùnior et al. [16] measured displacements by means of two methods, i.e. the DIC

software *Correli* and the UTM *EMIC*. Strains were calculated from displacement data and subsequently the compressive moduli were determined through the two above-mentioned methods. Hence, the compressive modulus calculated from DIC strain data are 30 % higher than the compressive modulus calculated from UTM displacement (strain) data. They explained this difference as an effect of the UTM flexibility, which can be connected to the procedure of *compliance correction*. This procedure is described in the ASTM D1621-10 [25].

Kidd et al. [69] applied simultaneously the DIC and ultrasonics techniques on the Divinycell® H foam grade with different densities for investigating the changing of the compressive modulus and the yielding behaviour. They applied the model presented by Gibson and Ashby [45] for clarifying the transition of deformation modes of foams with lower and higher densities.

Zhang et al. [123] focused on sources of uncertainties during compression testing of the Divinycell® H foam grade at higher temperatures. Uncertainties were mainly related to the fixture, which included the jigs and the thermal chamber for high temperature testing. Strain fields over the specimen surface were obtained by using the DIC technique. They developed a methodology that is based on the FEA of the specimen, in order to link bulk strain values with strain maps over the surface. The methodology gave back correction factors, that depended on the compressive modulus for both the through-thickness and the in-plane directions. Zhang et al. [123] described also an analysis on the degradation of the compressive modulus for increasing temperatures. Luong et al. [77] presented a comprehensive study on compression tests at different strain rates by means of the split-Hopkinson pressure bar method. The failure mechanism for different densities of the Divinycell® HP foam grade was investigated. Namely, the buckling of cell walls arises during compression tests on higher density foams. Whereas the wrinkling of cell faces appeared in compression tests on lower density foams. Studies about the strain rate influence on a few Divinycell® H grade foams were previously presented by Tagarielli et al. [103] and Daniel and Cho [26]. Further contributions of authors on the influence of the strain rate were summarised again by Luong et al. [77].

From a general overview on works dealing with strain rate sensitivity [26, 77, 103], it can be concluded that the peak yield stress increases with higher strain rates. Whereas the compressive modulus seems to be mostly not conditioned [26] for lower density foams, i.e. H100. A gradual increase of the compressive modulus for higher density foams, i.e. H250, was observed by Tagarielli et al. [103] up to a threshold, beyond which the compressive modulus decreases to values similar to

those concerning lower strain rates. All authors [22, 69, 77] dealing with different nominal densities, reported the increment of the compressive modulus and strength with the density.

Rajput et al. [88] focused on the measurement of the compressive modulus of polymeric foams, including the Divinycell® H60 grade. As already mentioned in Section 1.1, the available scientific literature reported greatly different values of the compressive modulus for the respective polymeric foam. This is due to the absence of an univocal applied procedure for compression testing, as well as to the different formulas for the strains calculation. Rajput et al. [88] discriminated between "gross" strain and "net" strain measurements. The *gross* strain measurement was done by means of an extensometer applied between the loading platens. The *net* strain was obtained by means of the DSP (Digital Speckle Photography) method, which is distinguished by the DIC technique because the speckle pattern is applied by the laser [63, 99, 116]. A further extensometer was applied on the specimen surface for measuring the *net* strains. They found different compressive moduli, as determined also by Caliri Jùnior et al. [16]. This difference was explained by the possible presence of damaged cells on the specimen surface. Thus, a vinylester resin was applied on the specimen surface in order to stiffen the cells. The resin induced in the foam a moderate but still insufficient increment of the compressive modulus, which had been evaluated from the so-called gross strain. Rajput et al. [88] concluded that the difference in compressive moduli may be due to the localisation of strains near the boundary of the specimen, that would decrease the compressive modulus value, if included in the ROI.

Miyase and Wang [81] aimed to develop procedures for compression and shear testing of the Divinycell® H80 foam, focusing on the specimen shape as well as the ratio of characteristic sizes of the specimen.

2.3 Multiaxial testing of the material

For the sake of designing sandwich composites, the development of yield and failure surfaces is essential. Failure surfaces can be obtained by gathering results from a wide range of multiaxial tests. Several studies were done on the multiaxial behaviour of polymer foams, such as PMI (polymethacrylimid) foams [2, 9, 42]. More details on the above-mentioned works can be found on the introductory part of Concas et al. [23].

Multiaxial states of stress on both metal and polymer foams have been obtained

mostly by usage of:

- UTM on tubular specimens, e.g. [121];
- UTM equipped with particular clamps or other rigs, e.g. [27, 86, 90];
- UTM, which can drive torsional loads and, if needed, equipped with particular clamps, e.g. [13, 23, 64, 65];
- fixtures based on the Arcan specimen [3], e.g. [39, 82, 83, 117, 124];
- fixtures based on a bending test device, e.g. [9, 75];
- new developed fixtures, e.g [38, 47, 72, 109].

Alongside these studies, several works paid attention on the development of the failure surface for PVC foams and therefore, to the execution of multiaxial tests. Deshpande and Fleck [32] performed a wide range of tests including uniaxial tension, compression and shear, hydrostatic, biaxial and triaxial tests on Divinycell® H100 and H250 foams . They adapted the yield function presented by Gibson et al. [46] to the collected yield data. Despite of the evident brittle behaviour of the foam under tensile and shear loading, they defined an artificial yield point by extrapolation. Gdoutos et al. [43, 44] conducted uniaxial and multiaxial tests on the Divinycell® H100 and H250 foams with several test rigs and specimens. They presented the prediction of the failure surface by the Tsai-Wu failure criterion [110], which was used recently also by Hoo Fatt et al. [57]. Christensen et al. [21] performed tensile, compression, torsional tests and further combined axial-torsional tests on tubular specimens of the Divinycell® H200 foam grade. They developed a yield criterion which is fitted to yield data. Concerning tensile tests, they considered the load, for which fracture in the specimen occurs as yield limit. Moreover, they assessed the torsional response as ductile and thus the torsional test was not conducted up to the failure of the specimen.
In all above-mentioned works [21, 32, 43, 44], glue or adhesives are mostly used for fixing the position of the specimen and for attaching strain transducers. However, the usage of such methods in relatively soft foams could have a great influence in the determination of mechanical properties. For combined axial-torsional loading, only tubular specimens were used with their axis oriented in the through-thickness direction [21, 43, 44]. Furthermore, these works lacked any in-situ inspection of the specimen during tests in order to study the deformation mechanism, which could be achieved by using the DIC method.

More recently, Shafiq et al. [93] presented a comprehensive set of yield data of the Divinycell® H100 foam grade (including also triaxial tests), on which the yield criterion of Ayyagari et al. [8] is fitted.

In Section 1.1 works of Taher et al. [106] and Hoo Fatt et al. [57] have been quoted for associating the opportunity of conducting multiaxial tests with the DIC. Nonetheless, Taher et al. [105, 106] described only the tensile, compressive and shear response of the PVC foam, without any mention to the combination of two loads. Hoo Fatt [57] conducted compression, shear and combined compression-shear tests on the Divinycell® H100 foam by using butterfly-shaped specimens, a fixture based on the Arcan specimen and a pressure vessel apparatus. According to Hoo Fatt [57], results of triaxial tests, which would be feasible with the aforesaid equipment, will be described in a later work, that at the current time has not been published yet. Strains for compression tests are calculated by the displacements between platens. Strains for the shear test and the combined compression-shear test are likely to be obtained by the DIC.

Chapter 3

Compressive characterisation

3.1 Experimental set-up

Compression tests were performed using the equipment available at the Department of Mechanical, Chemical and Materials Engineering, University of Cagliari (Italy):

- MTS 370 servo-hydraulic universal testing machine (MTS System Corp.)
  - load cell capacity: 100 kN
  - LVDT (Linear Variable Displacement Transducer) sensor
- two aluminium plates ($80 \times 80 \times 15$ mm^3)
- camera Pike F421B (Allied Vision GmbH), equipped by a IEEE 1394b connector
- USB-6009 data acquisition device (National Instruments Corp.)

According to the work of Zhang et al. [123], cubic specimens with sizes of $40 \times 40 \times 40$ mm^3 are used. Cubic specimens were obtained from PVC foam panels by band saw cutting and subsequent smoothing of the specimen surface by sandpaper. The specimen size was chosen also taking into account the thickness of available panels (40 mm).
Compression tests were conducted by placing the aluminium plates onto the grips of the actuator. The specimen was positioned between the two aluminium plates without using glue or an adhesive. Two types of aluminium plates were available, which are depicted in Fig. 3.1: the type (a) owned a pin for each plate in order to be clamped by the grips; the type (b) could be simply leaned against the lower grip, as

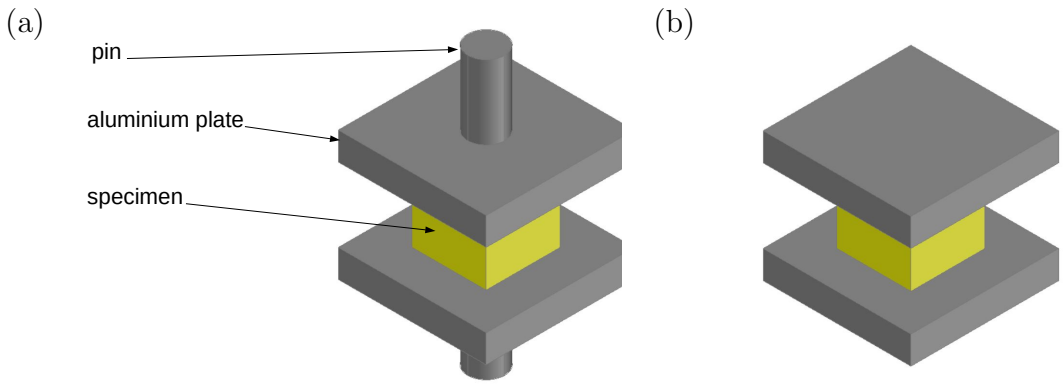

Figure 3.1: Available aluminium plates: with pins (a) and without pins (b).

shown in Fig. 3.2. Based on preliminary tests executed by the author, compressive stress-strain curves, which were obtained by using the two different types of platens, did not exhibit any difference, therefore the type (b) of platens was chosen for all compression tests.

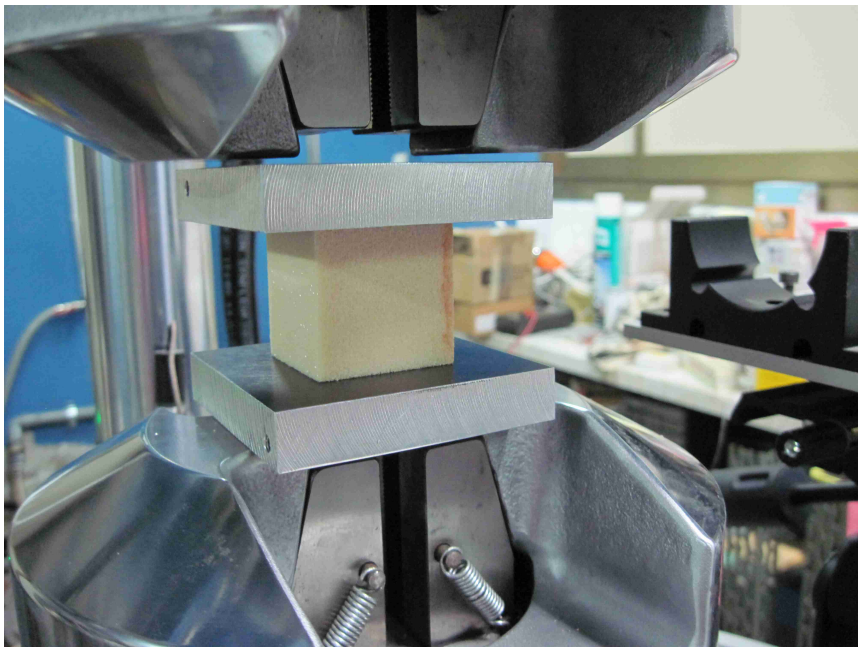

Figure 3.2: The aluminium plates and the specimen placed on the lower grips.

The actuator of the universal testing machine was driven by displacement control at a speed of 3.973 mm/min in accordance with the ASTM D1621-10 [25]. During the test, the specimen underwent a decrease of the thickness up to 87.5 % of the initial value, i.e. from 40 mm up to 5 mm, in order to make the specimen reach an advanced stage of densification.

Given displacement data from the LVDT sensor, strains were calculated by the

Green-Lagrange formulation in Eq. 3.1, taken from [112]:

$$\varepsilon = \frac{1}{2}\left[\left(\frac{H}{H_0}\right)^2 - 1\right] \tag{3.1}$$

H_0 and H denote the initial and the current height of the cubic specimen, respectively. Images were recorded during tests by the above-mentioned camera as Portable Network Graphics (PNG) format with the following features:

- acquisition frequency: 1 Hz
- resolution: 2048×2048 px

Driving and control of image recording was conducted by running a *Virtual Instrument* file written by the supervisor (Prof. Ing. Baldi) and modified by the author using LabView™ (National Instruments Corp.). Images were acquired in order to evaluate displacements and strains by the DIC method. DIC was achieved by the *NCorr* v. 1.2.1 open-source software [12] developed in the MATLAB® environment (MathWorks, Inc.).
The specimen surface exposed to the camera was covered by a thin coating of watercolour in order to use cells as a speckle pattern and to avoid the reflection of the light incident on the specimen surface, which would affect the validity of the DIC analysis.

3.2 Strain measurement

Compression tests were performed in accordance with the ASTM D1621-10 [25] on Divinycell® HP foams labelled as HP60, HP100 and HP160. The number in the nomenclature refers to the nominal density, i.e. 65, 100 and 160 kg/m^3, respectively [36]. It should be mentioned that the actual nominal density of the HP60 grade (65 kg/m^3) is higher than the reported number in the nomenclature. The specimen geometry was defined in Section 3.1. Strains were evaluated by readings of the LVDT sensor in the universal testing machine and the usage of Eq. 3.1. Compressive stress-strain curves are shown in Fig. 3.3 and obtained yield stress values are listed in Tab. 3.1. As preliminary test, only one specimen for each foam grade was studied.

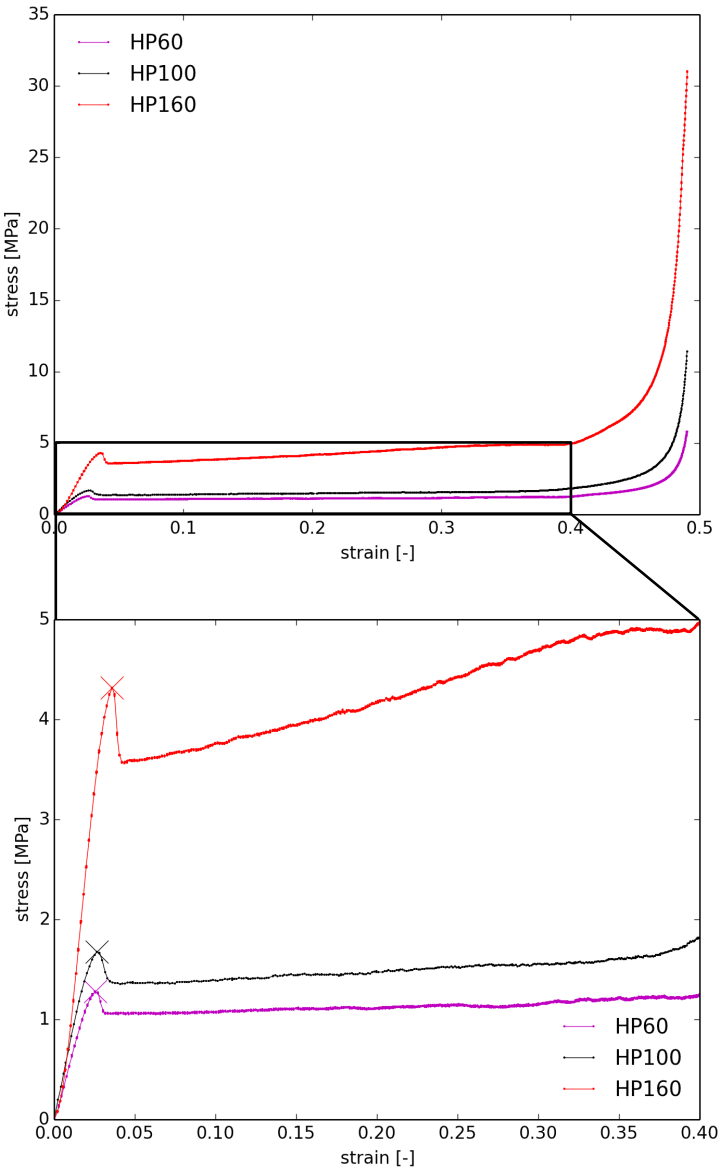

Figure 3.3: Compressive stress-strain curves for the three densities of the HP foam and magnification of the diagram in the elastic field and the plateau, with marking of peak yield stresses by crosses.

Foam grade	Yield stress [MPa]
HP60	1.28
HP100	1.68
HP160	4.32

Table 3.1: Yield stress values for HP60, HP100 and HP160 foams (one specimen for each foam grade).

From the above-mentioned preliminary tests, the yield stresses of the HP100 and the HP160 foams are respectively 31.3 % and 237.5 % higher than the yield stress of the HP60 grade.

As demonstrated in Section 2.1, the size and the shape of cells observed in the through-thickness and the in-plane directions are different. This involves different stress values for specimens subjected to compressive loading in the two main perpendicular directions.

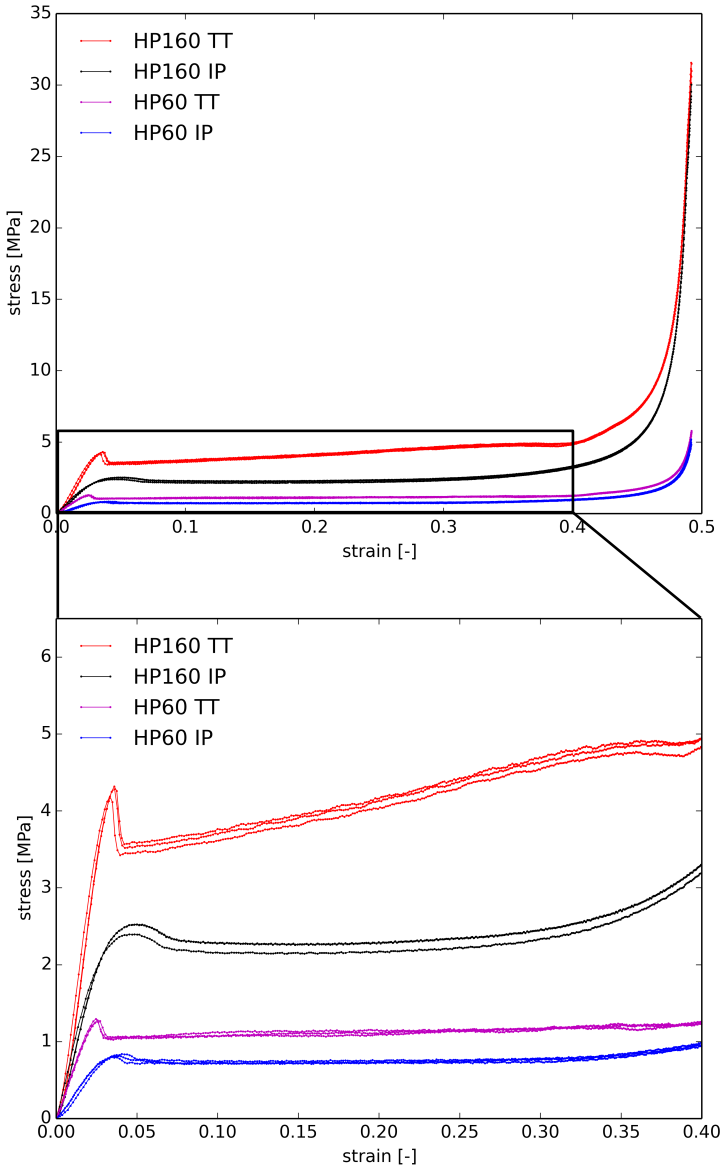

Figure 3.4: Compressive stress-strain curves for the HP60 and HP160 foams along the *through-thickness* (TT) and *in-plane* (IP) directions and magnification of the diagram in the elastic field and the plateau.

Foam grade (direction)	Yield stress $[MPa]$
HP60 (TT)	1.28 ± 0.015
HP60 (IP)	0.82 ± 0.017
HP160 (TT)	4.26 ± 0.056
HP160 (IP)	2.48 ± 0.060

Table 3.2: Average values and standard deviations of the HP60 and HP160 foams referring to the *through-thickness* and the *in-plane* direction.

In Fig. 3.4 compressive stress-strain curves show that foams have higher strength when loaded in the through-thickness direction. More specifically, the ratio between compression yield stresses in the through-thickness and the in-plane direction can be calculated from values in Tab. 3.2 and is equal to 1.37 for the HP160 and 1.15 for the HP60. In through-thickness compression tests of both HP60 and HP160, the peak yield stress is followed by a steep decrease of the stress value and the subsequent beginning of the plateau stage. The peak and the following steep decrease are more noticeable for the HP160 grade. For in-plane compression tests of the HP60 and HP160, no peak yield stress is evident between the elastic and the plateau stage. Hence, the point of the curve in-between the elastic stage and the plateau is defined as yield stress if its tangent is horizontal, i.e. the derivative is equal to 0.
Vertical strain maps were obtained by means of the DIC analyses performed by NCorr and are depicted in Figs. 3.5-3.6 for the HP60 and the HP160 foams, respectively. All strain maps refer to time steps when yielding arises in each specimen, i.e. the peak yield stress is reached. In accordance to the work of Zhang et al. [123], a ROI of $20 \times 20\ mm^2$ (centred to the specimen surface) was considered in all DIC analyses for preventing undesired contributions, that come from the contact between the cubic specimens and both aluminium plates, as well as the involvement of small-size cells near the surface of the cubic specimen. For compression tests of the HP60 foam in the through-thickness direction, strain contour lines appear very coarsely horizontal in the upper part of the ROI for the first two specimens (see Fig. 3.5). Whereas the horizontal trend of the strain contour lines is detected in a delimited area at the lower-right part of the ROI in the third specimen. The location of horizontal strain contour lines appears to be mostly random, especially for compression tests of the HP60 in the in-plane direction. In such tests, the strain gradients are much higher than the strain gradients relating to through-thickness compression tests.

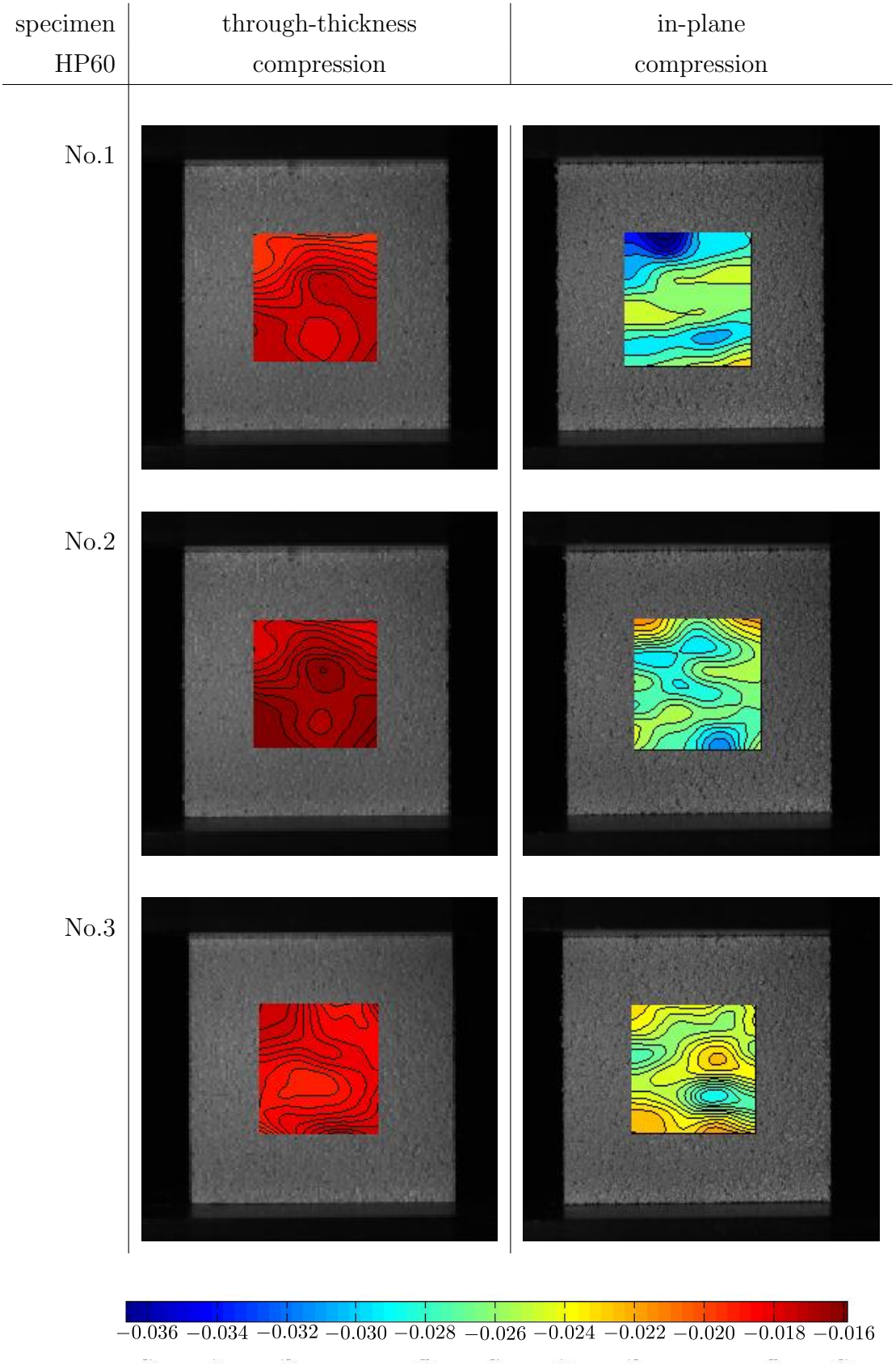

Figure 3.5: Vertical strain fields calculated by NCorr at the peak yield stress for three specimens of the HP60 foam subjected to through-thickness (left) and in-plane compression (right).

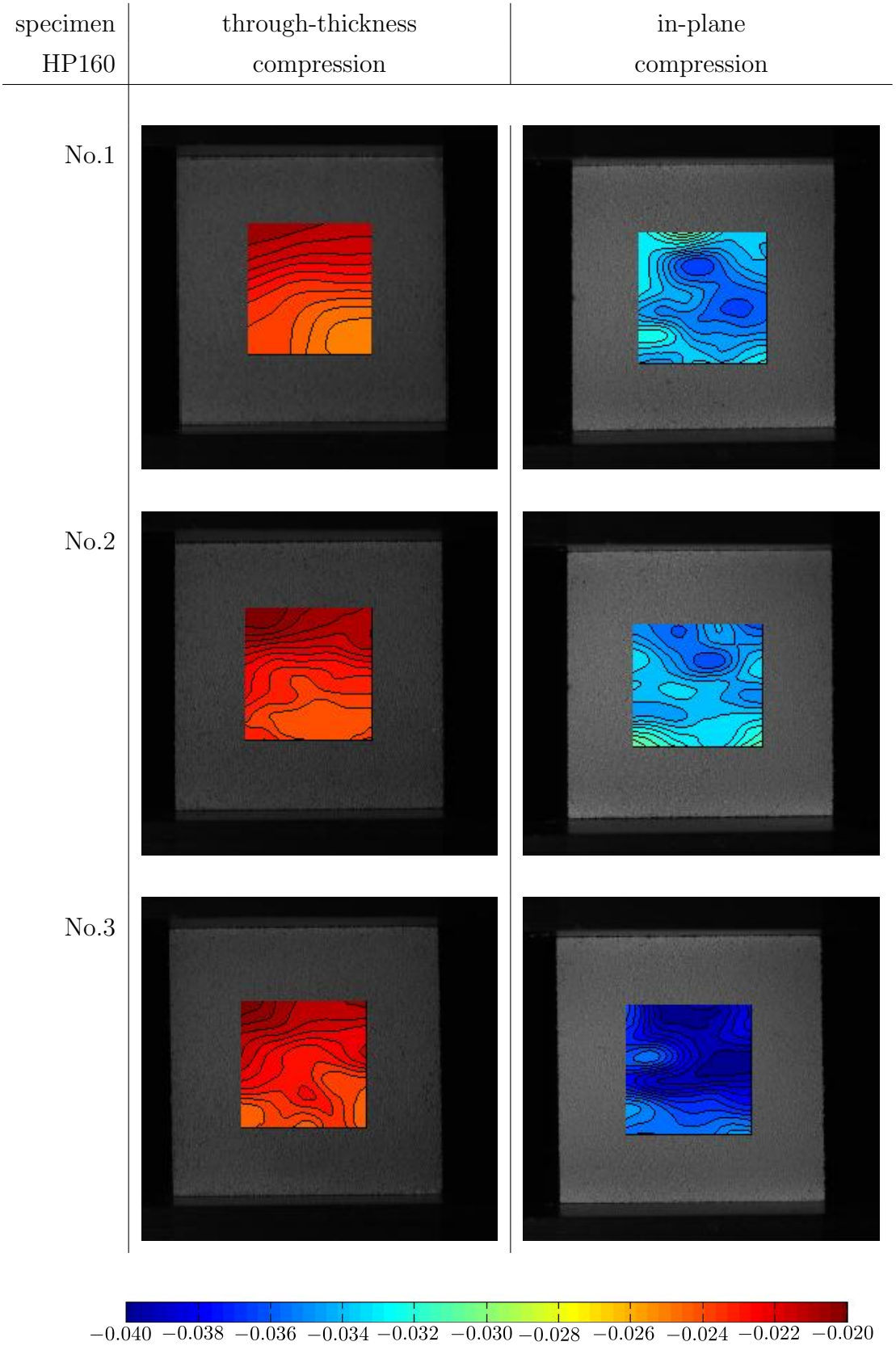

Figure 3.6: Vertical strain fields calculated by NCorr at the peak yield stress for three specimens of the HP160 foam subjected to through-thickness (left) and in-plane compression (right).

Fig. 3.6 shows vertical strain maps for compression tests on the HP160 foam. In the case of through-thickness compression, strain contour lines are more uniform and horizontal if compared with strain contour lines for the HP60 foam. A lower presence of closed contour lines is also observed, namely, only for the third specimen a closed strain contour line is clearly seen and another one is partially closed in the second specimen. Such feature is likely to be due to the lower size of the cells for the HP160 foam. Nonetheless, by observing the strain map for the in-plane compression of both HP60 and HP160, the strain contour lines exhibits similar trends, with occurrence of several closed contour lines and higher absolute strain values in comparison with through-thickness compression for both nominal densities.
The above-mentioned considerations on the strain fields introduce the option of strain measurement by means of the DIC. A correct measurement of strains is of crucial importance for the evaluation of the compressive modulus. Taking into account the two grade HP60 and HP160 and the two main directions, a comparison of stress-strain diagrams is presented in Figs. 3.7-3.10, whose strains are calculated by:

- using Eq. 3.1 with displacements values given by the LVDT sensor
- averaging strain fields obtained by the DIC (using the already mentioned NCorr software),

respectively. The mentioned procedures are similar to those presented by Rajput et al. [88], who compared averaged strain values resulting from the DSP method with strain values obtained by extensometers applied on the specimen surface and between plates. As reported by Caliri Jùnior et al. [16] and Rajput et al. [88], the compressive modulus, which is calculated by taking into account strains from the full-field optical method, is higher than the obtained compressive modulus by considering strains from readings of the UTM sensor or the applied extensometer between the load platens. According to preliminary DIC analyses, a ROI covering the whole surface of the specimen exposed to the camera, i.e. $40 \times 40\ mm^2$ leads to the same value of the compressive modulus, which is obtained by taking into account the smaller ROI. Hence, the size of the ROI does not influence the average value of strains.

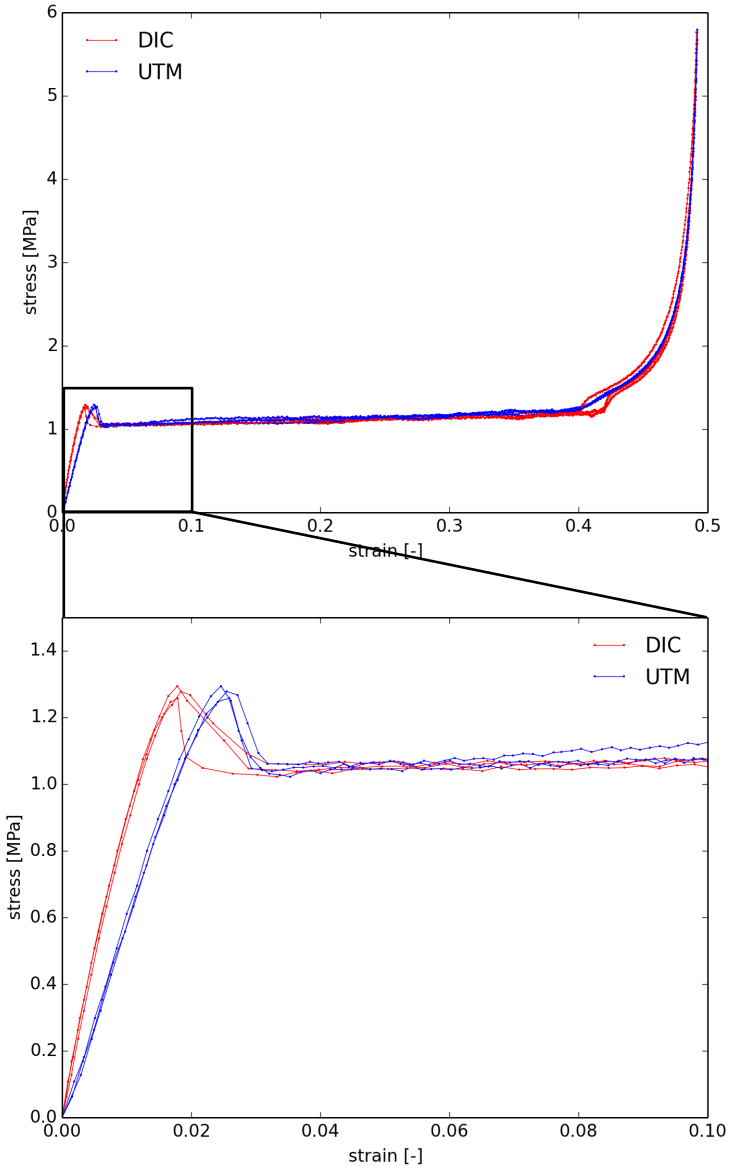

Figure 3.7: Compressive stress-strain curves for three specimens of the HP60 foam loaded in the through-thickness direction with magnification of the diagrams in the elastic field and plateau starting.

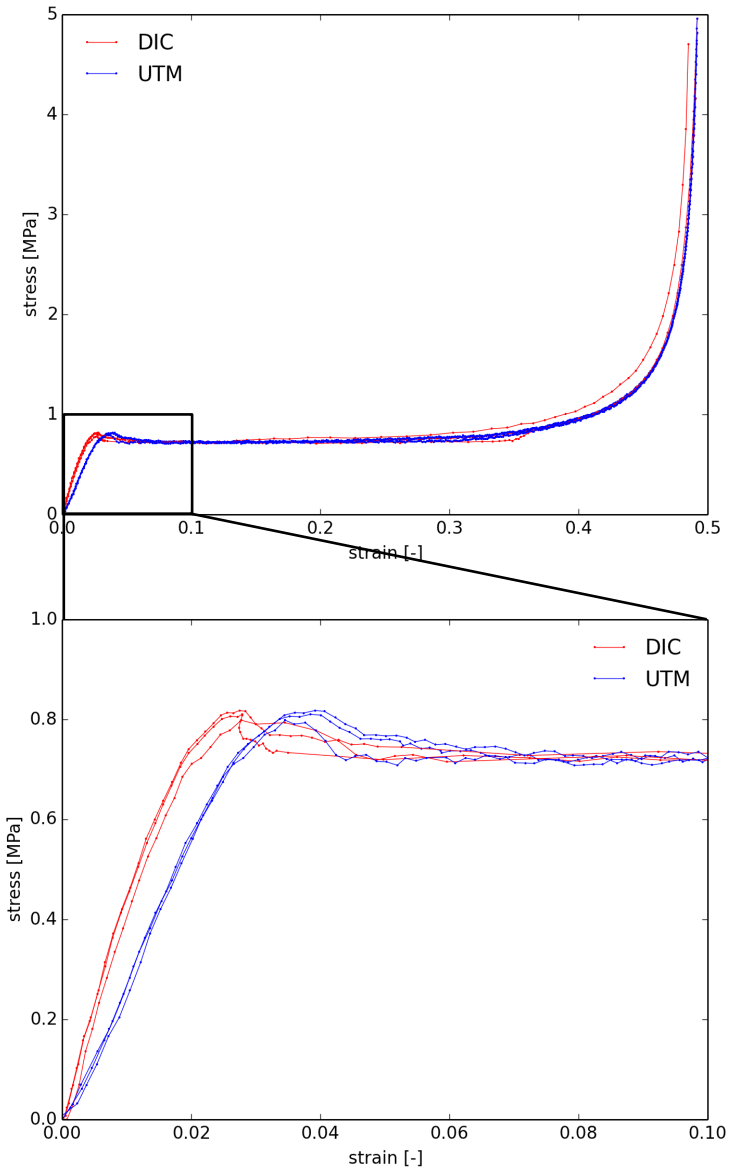

Figure 3.8: Compressive stress-strain curves for three specimens of the HP60 foam loaded in in-plane direction with magnification of the diagrams in the elastic field and plateau starting.

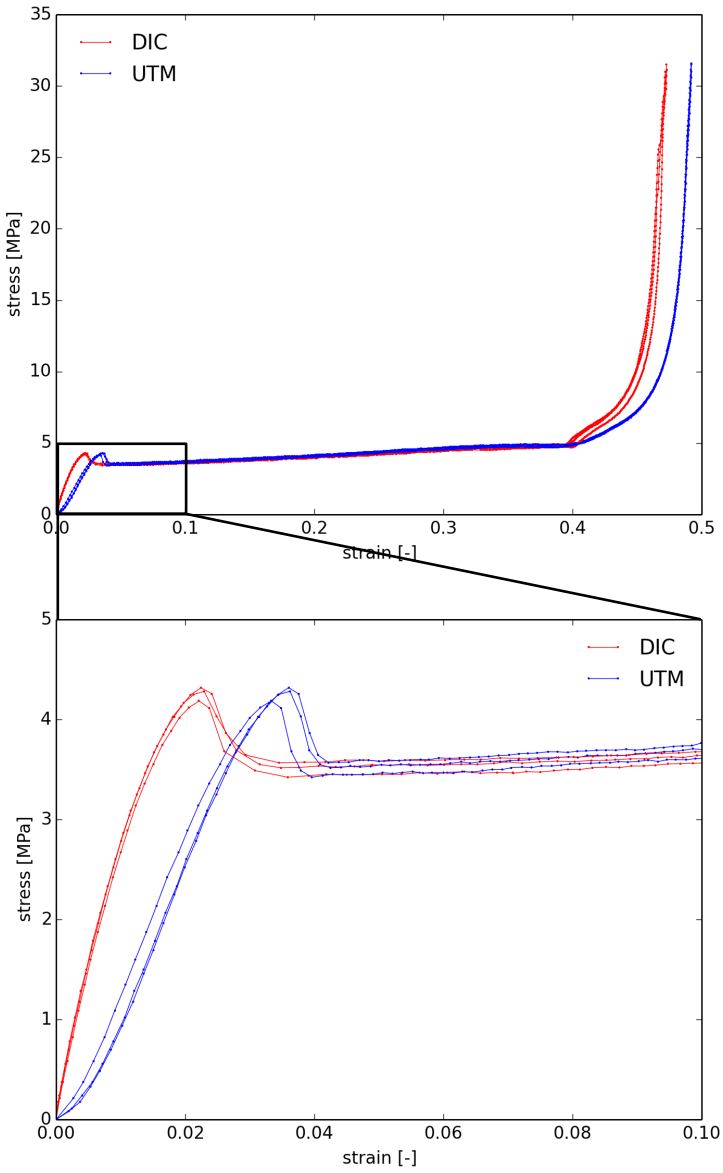

Figure 3.9: Compressive stress-strain curves for three specimens of the HP160 foam loaded in the through-thickness direction with magnification of the diagrams in the elastic field and plateau starting.

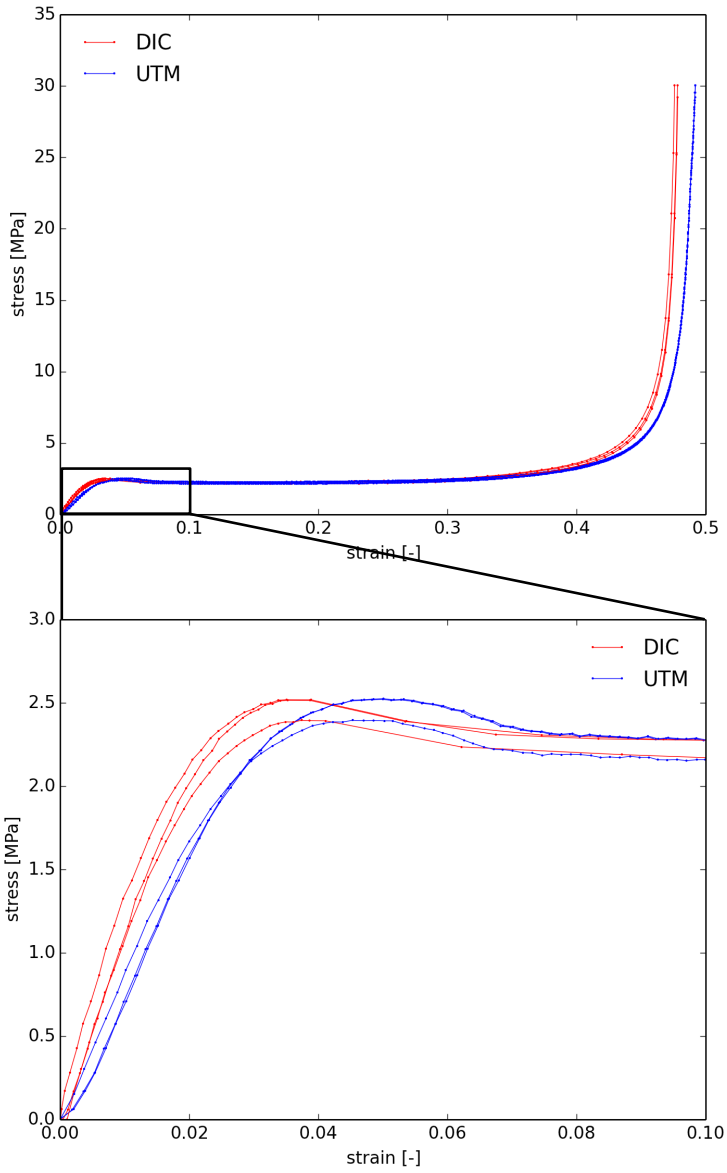

Figure 3.10: Compressive stress-strain curves for three specimens of the HP160 foam loaded in in-plane direction with magnification of the diagrams in the elastic field and plateau starting.

3.3 Compressive modulus

The compressive modulus was evaluated for three specimens of the HP60 foam, which were tested in the through-thickness direction. During compression tests, images were recorded with an acquisition frequency of 2 Hz, in order to obtain the compressive stress-strain diagram with a larger amount of data. Compressive stress-strain diagrams are depicted in Fig. 3.11. As in the previous Section, strain values are calculated by the DIC for the first curve, i.e. averaging the vertical strain

values obtained by the DIC and considering a ROI centred to the specimen and large $20 \times 20\ mm^2$. For the second curve strains are calculated by means of the Eq. 3.1 from UTM output data, i.e. recorded displacement data of the LVDT sensor.
According to ASTM D1621-10 [25], the compressive modulus is calculated from "any convenient point along the steepest straight line portion of the load-deflection or load-strain curve". Because of the evident *pseudo-elastic* behaviour [4, 45], two parts of both diagrams exhibit straightness, which are highlighted in Fig. 3.11 by adapting a straight line to each curve. Therefore, the compressive modulus could be defined by adapting the above-mentioned straight line on two different parts of the curve:

- the part, where the curve is smoother. The calculation of the compressive modulus in this part of the diagram is denoted as *1st method* in Fig. 3.11;
- the "steepest straight portion" of the stress-strain diagram, as suggested by the ASTM D1621-10 [25]. This part exhibits a low scattering, therefore a linear fitting between compressive stress-strain data is needed. The calculation of the compressive modulus in this part of the diagram is denoted as *2nd method* in Fig. 3.11.

The steepest straight portion follows the *toe*, which was mentioned by Rajput et al. [88]. A very slight *toe* occurs in the 2nd specimen in Fig. 3.11 and is visible in the diagram, where strains were determined by UTM data.
In Tables 3.3-3.4 compressive moduli calculated by the two methods, i.e. from the two different straight parts of diagrams, are reported for each specimen. Resulting compressive moduli by DIC strain data exhibit a greater deviation between the two methods (Table 3.3). Whereas compressive moduli calculated by applying the two methods on the UTM strain data are consistent with each other (Table 3.4).

Specimen	Compressive modulus DIC data (1st method) [MPa]	Compressive modulus DIC data (2nd method) [MPa]
No. 1	88.60	108.82
No. 2	85.31	111.22
No. 3	81.22	100.32
Average	85.04 ± 3.02	106.78 ± 4.68

Table 3.3: Values of the compressive modulus determined by taking into account the two methods and DIC strain data.

Specimen	Compressive modulus UTM data (1st method) [MPa]	Compressive modulus UTM data (2nd method) [MPa]
No. 1	63.98	57.33
No. 2	65.84	57.38
No. 3	52.74	66.53
Average	60.85 ± 5.79	60.41 ± 4.33

Table 3.4: Values of the compressive modulus of the HP60 foam grade, which is determined by taking into account the two methods and strain calculated from UTM displacement data.

As stated also by Rajput et al. [88], greatly different values of the compressive modulus are obtained, depending on which method has been used for its determination. The compressive modulus provided by the manufacturer [36] is $74\,MPa$, i.e. a value in-between the compressive moduli listed in Table 3.3 (taking into account the aforesaid 1st method) and in Table 3.4, although all values are determined in accordance with the ASTM D1621-10 normative [25].

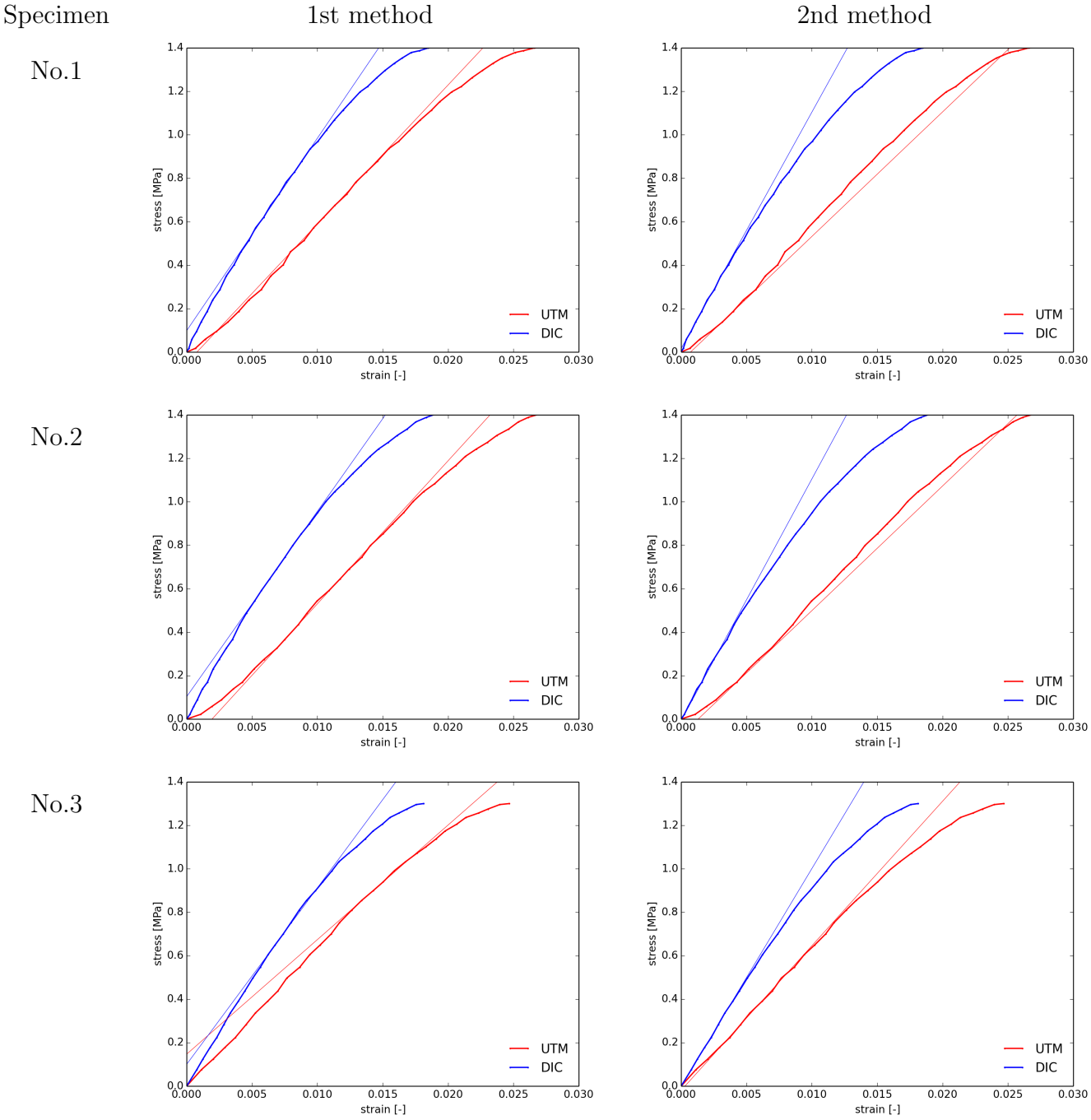

Figure 3.11: Compressive stress-strain diagrams for three specimens of the HP60 foam grade, whose strains are determined by the DIC and from UTM output data, respectively. The straight lines highlight the part of the diagram, that is considered for the calculation of the compressive modulus.

3.3.1 Compliance contribution

The compliance of the machine is defined by ASTM D1621-10 [25] as "the displacement difference between test machine drive system displacement values

and actual specimen displacement" and is partly due to the stiffness of the UTM components, which is mentioned by Caliri Jùnior et al. [16] as the main cause of the difference between the compressive moduli calculated from DIC data and UTM data, respectively.

An evaluation of the compliance contribution is conducted in this Section, according to the procedure described by the ASTM D1621-10 [25], but it is also adapted to the peculiar behaviour of the HP60 foam. The procedure based on ASTM D1621-10 [25] consists in moving the platen connected to the crosshead (i.e. actuator) onto the other platen, in order to execute in effect a mutual compression of the platens. Despite the fact that the procedure of the ASTM D1621-10 [25] imposes a displacement controlled test and a prescribed speed of the crosshead (i.e. actuator), the test was performed on the available aluminium plates by the UTM switched in load control with a rate of 150 N/s up to reach 2000 Ns, in order to obtain a compressive load-displacement diagram which would be consistent with the compressive load-displacement diagram of a HP60 foam grade. The diagram is depicted in Fig. 3.12. A linear fit of the highly scattered displacement data is shown as well.

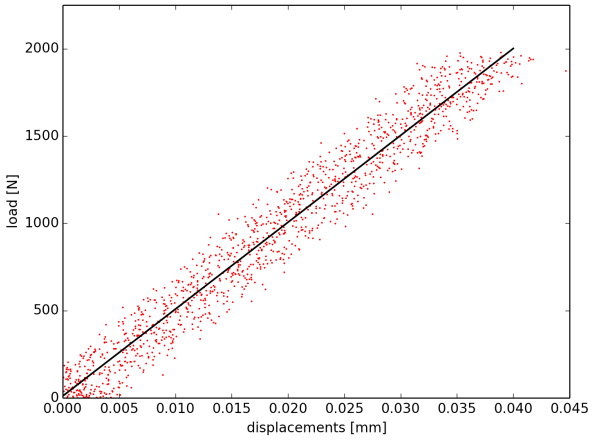

Figure 3.12: Linear fitting of compressive load-displacement data for the mutual compression of the aluminium plates.

According to ASTM D1621-10 [25], displacement data obtained by the mutual compression of the platens have to be subtracted from displacement data related to the HP60 foam. Both types of displacement data are recorded from measurements of the LVDT sensor. In Fig. 3.13 the compliance is subtracted for each specimen. From Fig. 3.13, the compliance gives evidently a scarce contribution in the measurement of displacements by the LVDT sensor for all tests. This is also evident from Fig. 3.14 and from Table 3.5, where the compressive moduli are evaluated

and summarised taking into account compliance corrected strains. The reason of different values of compressive moduli can be further investigated by a deeper inspections on strain maps in the whole specimen surface exposed to the camera and within the elastic stage. This study is performed by using the DIC and is the topic of the following Section.

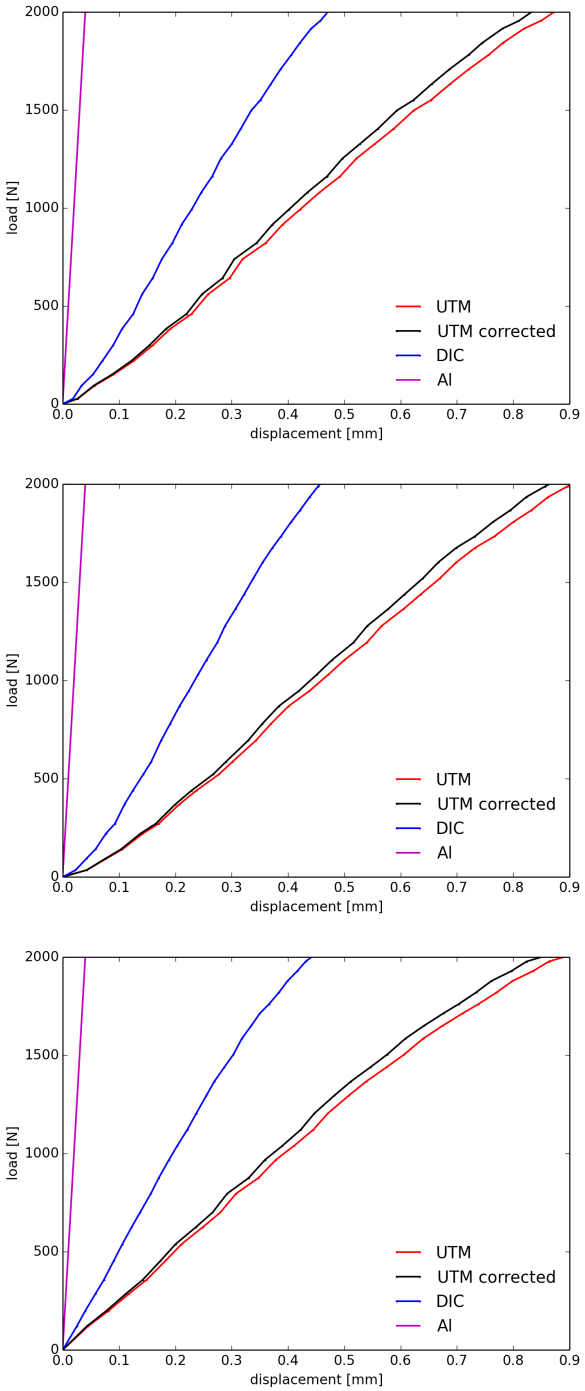

Figure 3.13: Compressive load-displacement diagrams for three specimens relating to DIC displacement data, UTM displacement data and compliance corrected data.

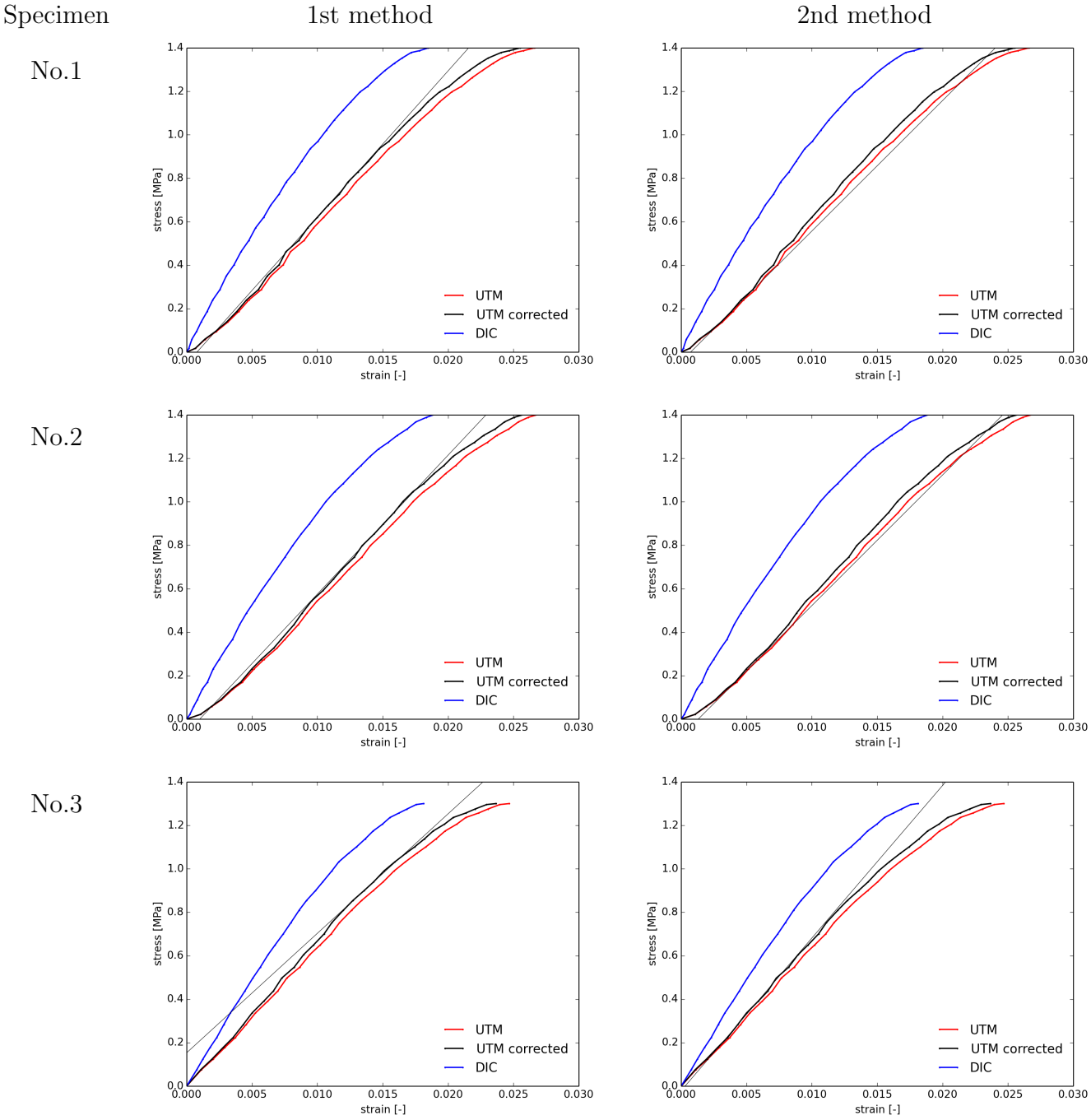

Figure 3.14: Compressive stress-strain diagrams for three specimens relating to DIC strain data, UTM strain data and compliance corrected data and depiction of the compressive modulus by means of the two methods.

Specimen	Corrected compressive modulus (1st method) [MPa]	Corrected compressive modulus (2nd method) [MPa]
No. 1	67.38	60.08
No. 2	63.95	60.12
No. 3	55.00	70.25
Average	62.12 ± 5.22	63.48 ± 4.78

Table 3.5: Values of the compressive modulus with compliance correction.

3.3.2 Strain inhomogeneity

The strain fields during yielding of the specimens are shown in Section 3.2 in Figs. 3.5-3.6. A ROI centred to the specimen surface was considered, which is thus far from contributions of the compression platens and specimen borders. Nonetheless, current strain fields appear inhomogeneous particularly in the case of foams with lower density and bigger cell size, i.e. HP60 foams.

The distribution of strains for a foam under compressive load and monitored by an optical full-field method was briefly mentioned by Rajput et al. [88] for a PMI foam grade, known with the trade name of R200H (Rohacell® 200 Hero). The R200H foam has a higher nominal density than HP60 foam, i.e. 205 kg/m^3 [87, 88] and 65 kg/m^3 [36], respectively. For such cases, deformation fields exhibit homogeneity with deformation bands near the contact between the specimen and compression platens. An analogous study was previously presented by Wang and Cuitiño [118] for open-cell PU foams. They compared strain values for lower and higher density foams by means of histograms and they observed also a more pronounced inhomogeneity of deformation contour plots for lighter foams. Nevertheless, they did not attribute strain values to areas of the specimen surface.

Thus, the whole area of the specimen exposed to the camera has been subdivided into eighteen ROIs, as shown in Fig. 3.15. Since Rajput et al. [88] found higher strains occurring near the platens, the ROIs, which are placed in the bottom of Fig. 3.15, namely, near the moving actuator, are narrower than the other. This is done in order to make possible higher strain gradients more perceivable. A DIC analysis is performed by means of the DIC software NCorr for each ROI. Afterwards, displacements and strains are averaged for each ROI and each time step, as done in the previous Sections, and finally plotted in Figs. 3.16-3.17.

In Fig. 3.16 the compressive load-displacement curves concerning the three ROIs of each single row from Fig. 3.15 are compared to the compressive load-displacement

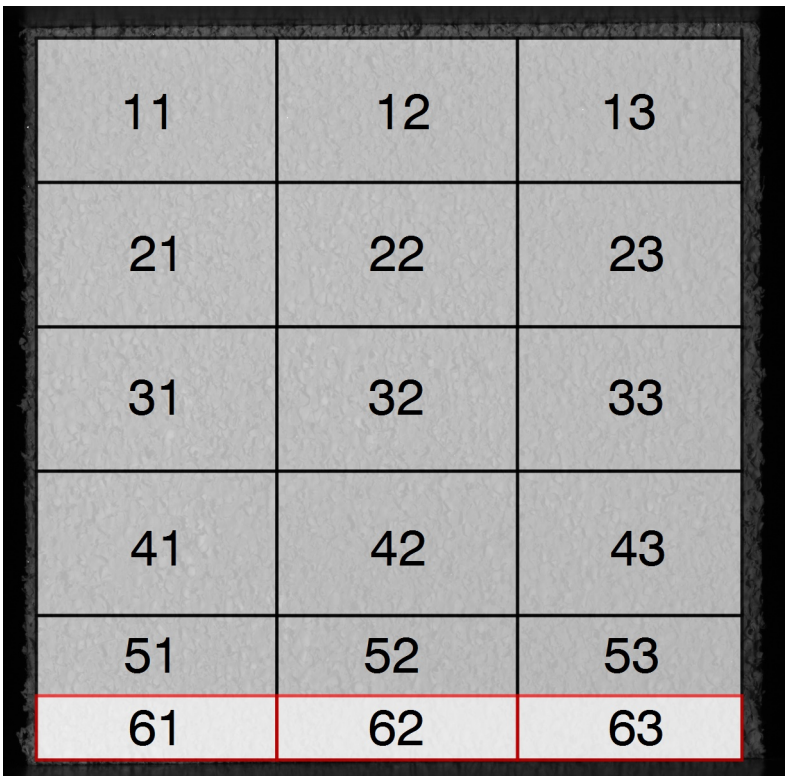

Figure 3.15: Acquired image of the specimen and localised ROIs. Each ROI is uniquely determined by two numbers, relating to the row position and the column position, respectively. The sixth row of ROIs (*61*, *62* and *63*) is highlighted due to its proximity to the moving actuator.

curves calculated by readings of the LVDT sensor in the UTM. Considering a single row *n*, the three ROIs *n1*, *n2*, *n3* are localised at the left side, the centre side and the right side of the specimen, respectively.

The transversal positioning of the ROI at the left side or rather the right side of the specimen give back analogous results in terms of displacements. It can be easily seen that displacement values obtained by the DIC are more similar to displacement values given by UTM output data, i.e. reading of the LVDT sensor, if the considered ROI gradually approaches the lower side of the specimen, namely, near the moving actuator. In other words, displacements obtained by using ROIs in the sixth row, as shown in Fig. 3.16 (f) are more similar to UTM output displacements than using ROIs taken from the first or the second row, as depicted in Fig. 3.16 (a)-(b). Areas of the foam specimen, which are near the lower (moving) compression platen, exhibit a lower stiffness than areas of the specimen located near the upper platen.

Concerning strains calculated by means of the DIC, the transversal position of the ROI plays a crucial role, as evident in Fig. 3.17. Analogously to displacements, the stiffness of the specimen decreases by gradually approaching the lower compression platens. In Fig. 3.17 (e), the compressive stress-strain curve related to the ROI *53*

passes through the UTM compressive stress-strain curve approximately at the end of the elastic stage. In Fig. 3.17 (f), the compressive stress-strain curve related to the ROI *62* has analogous values to the UTM compressive curve, whereas the ROI *63* exhibits an even lower stiffness, i.e. higher strains values with equal values of the compressive stress.

Compressive stress-strain curves according to the ROIs *53*, *62* and *63* disclose the occurring of higher strain values for the above-mentioned ROIs, and more specifically, of incipient deformation bands that would be visible in the plateau stage.

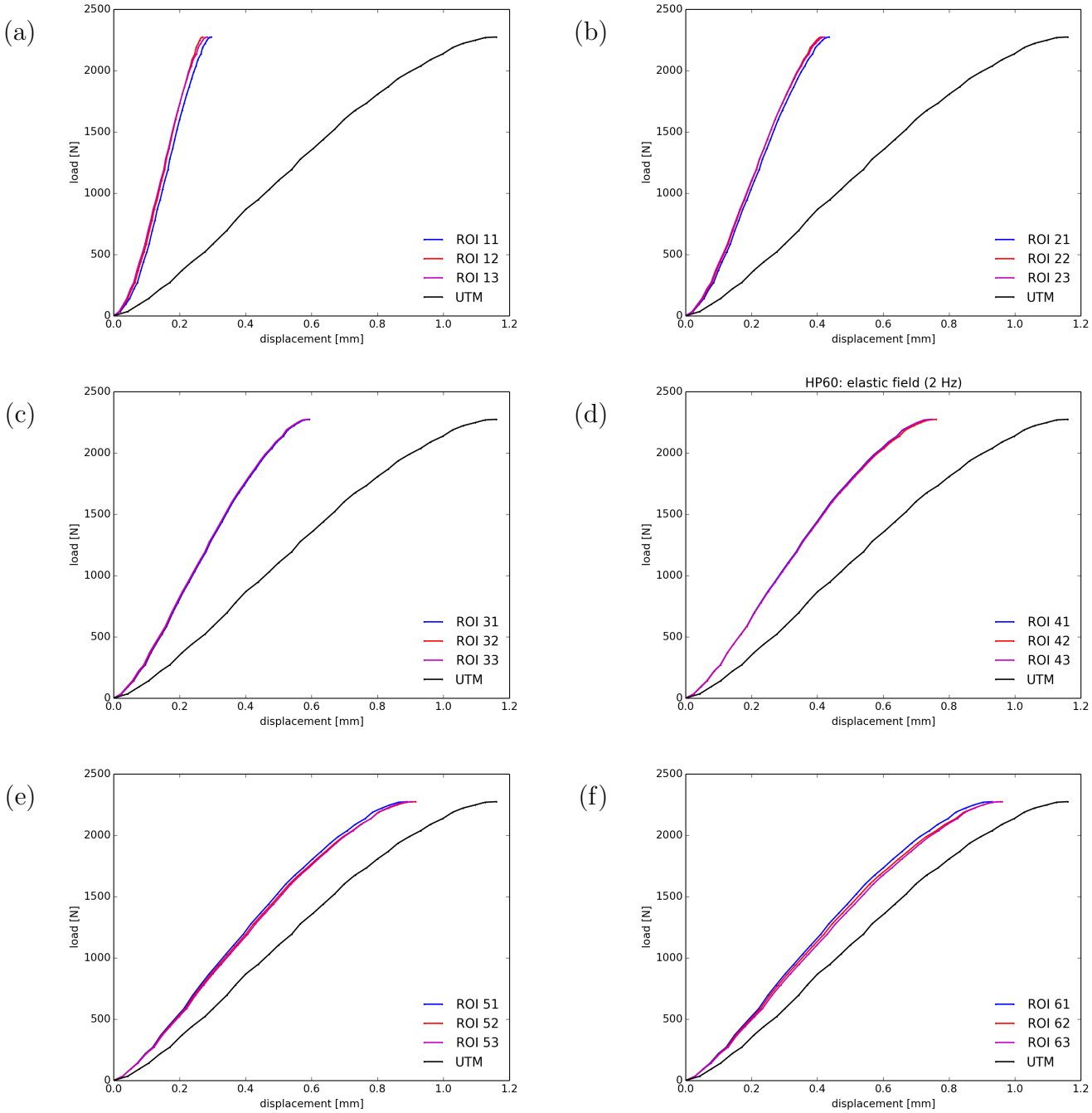

Figure 3.16: Comparison of compressive load-displacement diagrams obtained by UTM recorded data and localised ROIs depicted in Fig. 3.15: (a) first row of ROIs, (b) second row of ROIs, (c) third row of ROIs, (d) fourth row of ROIs, (e) fifth row of ROIs, (f) sixth row of ROIs.

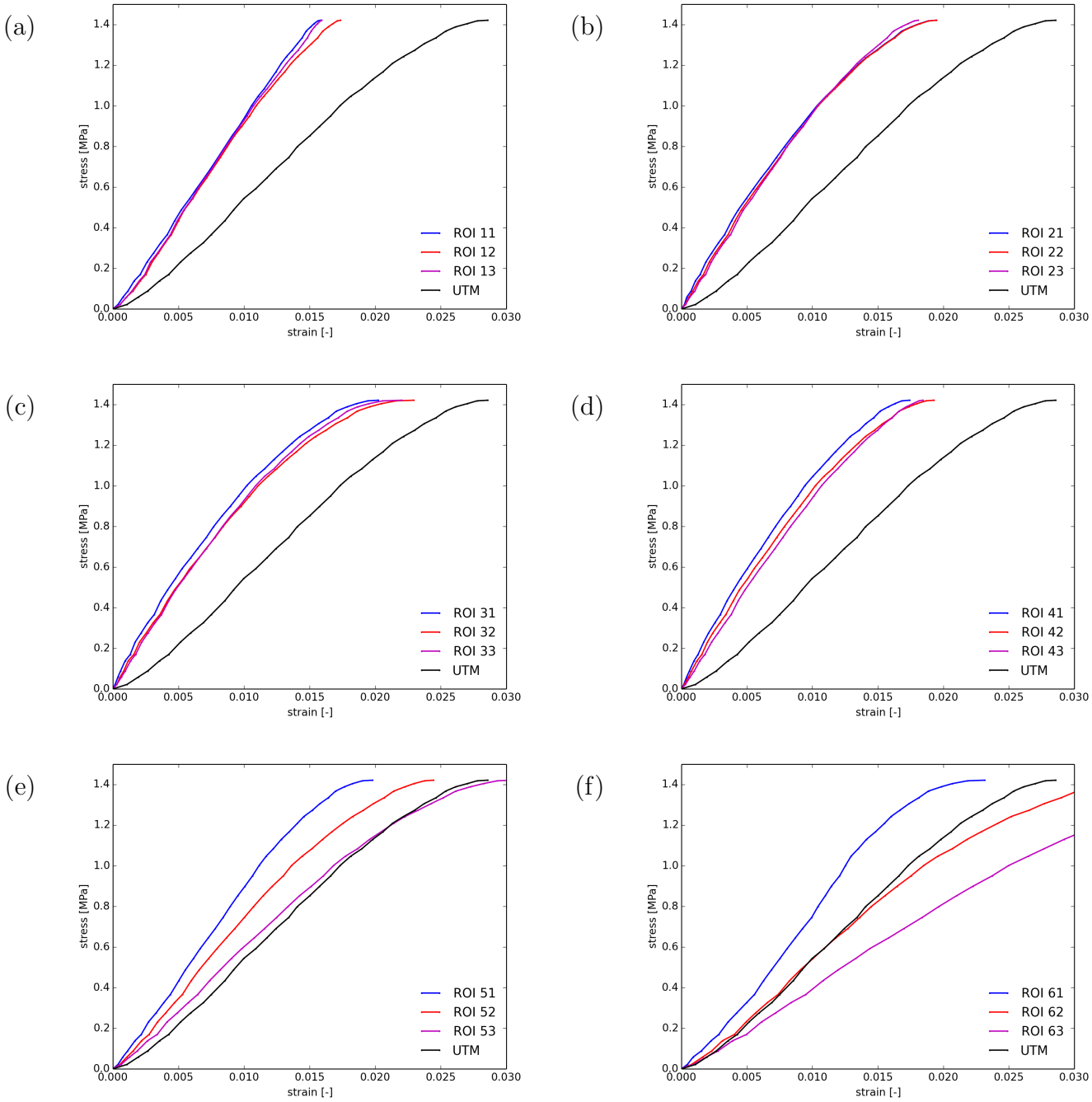

Figure 3.17: Comparison of compressive stress-strain diagrams obtained by UTM recorded data and localised ROIs depicted in Fig. 3.15: (a) first row of ROIs, (b) second row of ROIs, (c) third row of ROIs, (d) fourth row of ROIs, (e) fifth row of ROIs, (f) sixth row of ROIs.

Chapter 4

Failure surface

4.1 Specimen preparation

In order to trace the failure surface, a cylindrical specimen with a heigh/diameter ratio of 2:1 is used for all tests. As mentioned in Section 1.2, such a specimen is subjected to uniaxial loads (tension, compression and torsion) and further torsional loads with a uniaxial preload (either tensile or compressive). The cylindrical shape of the specimen prevents warping, which would occur if a squared cross-section specimen were used [65]. The height to diameter ratio of 2:1, as applied by Jung and Diebels [65], allows the exemplification of the formula for calculating the shear strain, i.e.

$$\gamma = \frac{\theta\,[rad]}{h}\frac{d}{2} \rightarrow \gamma = \frac{\theta\,[rad]}{4} \tag{4.1}$$

The dimensions of the specimen are shown in Fig. 4.1 (a) and have been defined by taking into account the thickness of the available panels (40 mm). The axis of the cylindrical specimen is orthogonal to the through-thickness direction. Hence, multiaxial tests aim to investigate mechanical properties of the material in the in-plane direction.

As shown in Fig. 4.1 (b), both ends of the specimen consist of a conical part and a further cylindrical part with a larger diameter, in order to facilitate the gripping of the specimen. The bushings are inserted in the specimen as shown in Fig. 4.1 (b). The bushings ensure the gripping of the specimen in the three-jaw chuck of the UTM.

The specimen is made from a piece of foam with a squared cross-section, which is cut from the panel by a band saw (Fig. 4.2 (a)). Subsequently, the foam piece is mounted in the lathe with the help of the tailstock, in order to obtain a cylindrical shape. The

cutting tool is a grinding wheel (Fig. 4.2 (b)). One half of the specimen still has a squared cross-section, therefore the specimen part with a new round cross-section is mounted into the lathe chuck for achieving the round cross-section also in the other half. The tailstock is removed at this stage (Fig. 4.2 (c)). Once the whole specimen has a round cross-section with a diameter of 38 mm (which is the maximal diameter of the specimen in Fig. 4.1 (a)), the finishing can be performed with the help of the tailstock (Fig. 4.2 (d)). Each production phase involves the usage of different special bushings for protecting the foam from the gripping of the lathe chuck.
Finally, speckles are made on the specimen surface by applying firstly a matte white varnish as background and subsequently a matte black varnish by an aerosol spray.

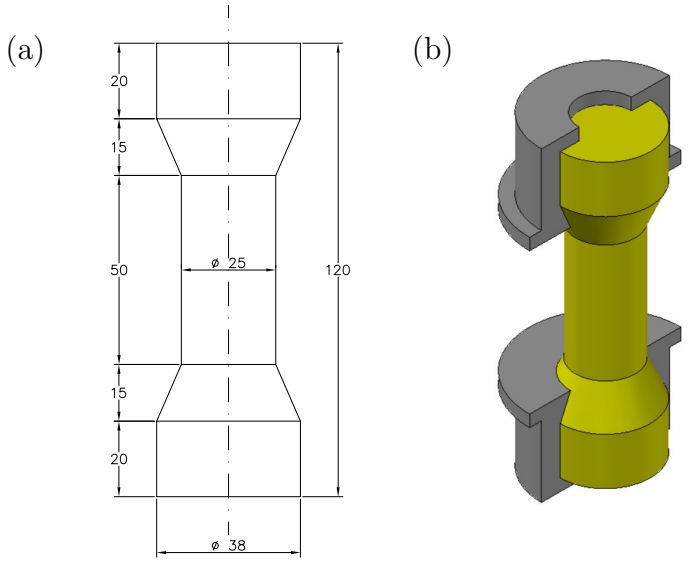

Figure 4.1: Specimen geometry (a) and cutaway of the bushings mounted on the specimen in all tests (b), according to Concas et al. [23].

4.2 Experimental set-up

Multiaxial tests have been performed by using the available equipment at the Chair Of Applied Mechanics, Saarland University (Lehrstuhl für Technische Mechanik, Universität des Saarlandes) in Germany. The equipment comprises:

- UTM Electropuls^{TM} E10000 Electropuls (Instron Ltd.). Load cell of 10 kN for axial loading and 100 Nm for torsional loading. Maximal actuator stroke: 60 mm;

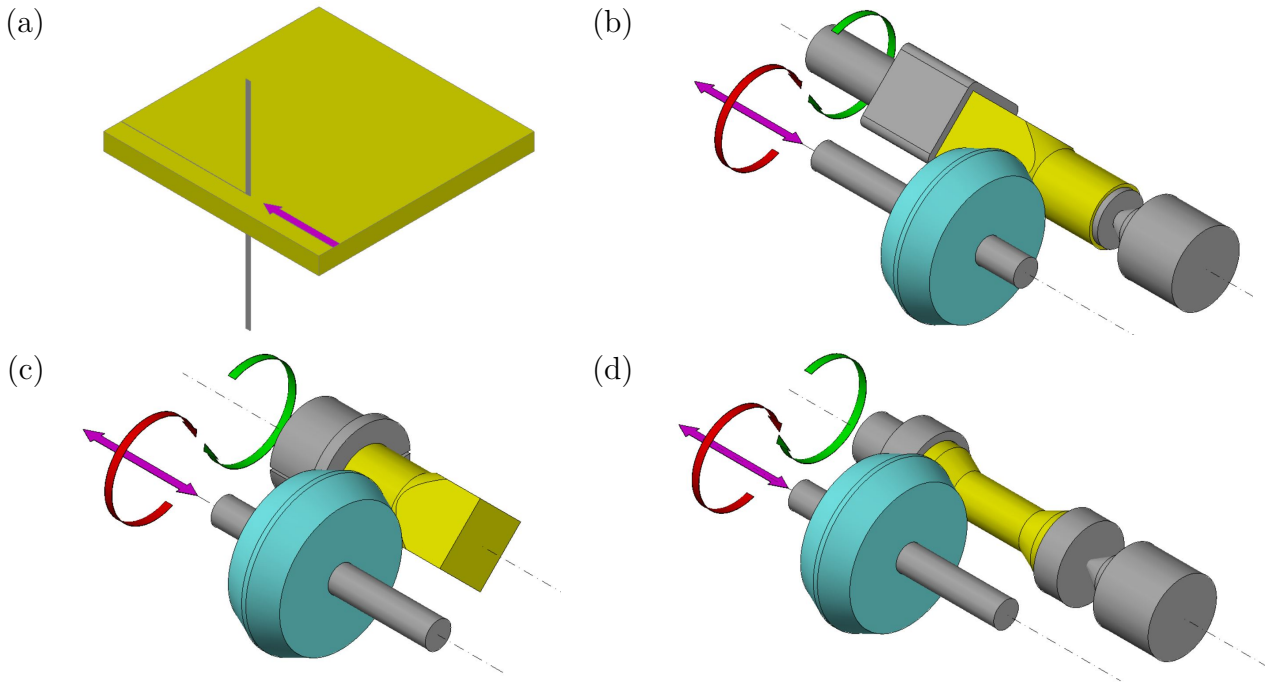

Figure 4.2: Schematic sequence representing the specimen manufacturing phases, according to Concas et al. [23].

- two three-jaw chucks inserted on the UTM for the specimen gripping;
- 8 cameras Manta G-235B (Allied Vision Technologies GmbH). Image resolution: 1936×1216 px;
- triggerbox (LIMESS Messtechnik u. Software GmbH) for transmitting signals from the UTM and the cameras to the laptop, where the 3D-DIC software is installed.

The experimental set-up is shown in Fig. 4.3 (a). The 8 cameras are put onto an aluminium cameras frame. Each camera is set at one vertex of an invisible octagon, as can be seen from the schematic in Fig. 4.3 (b). Such a positioning of cameras allows theoretically the monitoring of 360° of the cylindrical specimen.
Acquisition of images and the subsequent 3D-DIC evaluation is performed by means of the commercial software ISTRA 4D v.4.4.2 (Dantec Dynamics GmbH). The frequency of image acquisition is fixed at 1 Hz through the *Instron Wave Matrix* software, which allows also the setting of loading cycles to be performed by the UTM. ISTRA 4D performs the 3D-DIC by considering 4 pairs of cameras. In order to achieve the 3D-DIC, the calibration of cameras is essential. The calibration is done by rotating a plate with a printed pattern on its surface in the shared field of view of the cameras. The printed pattern is similar to a chessboard, like the

(a)

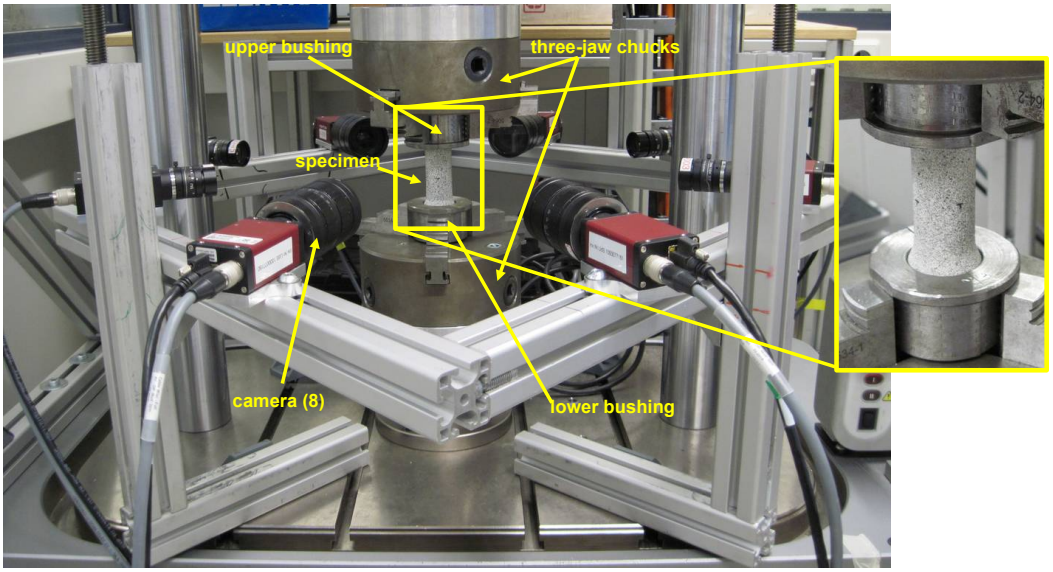

(b)

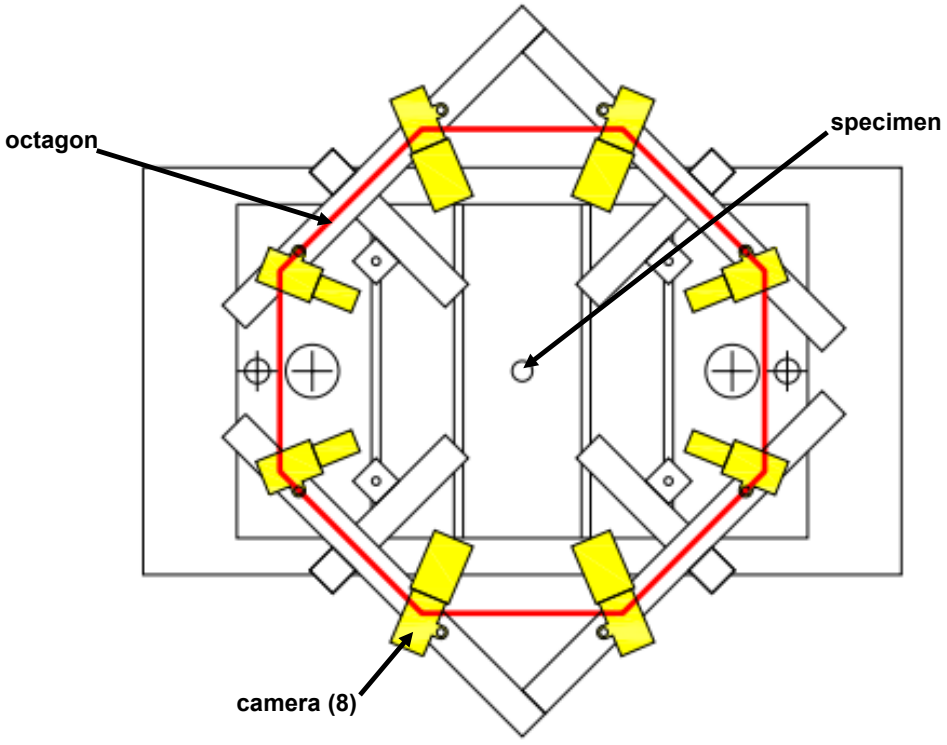

Figure 4.3: Experimental set-up with magnification of the specimen, according to Concas et al. [23] (a) and the schematic top view of the 8-camera system (b).

calibration target shown by Chen et al. [18] and since it is a known geometry by the software, intrinsic and extrinsic parameters are calculated by the software itself. The successive calculation of the failure parameters has been performed by using self-written Python® scripts, which have been tailored for each loading case. The above-mentioned scripts use different Python® modules for carrying out:

- the parsing of raw output data obtained by the UTM (applied module: *Os* and *Pandas*)
- calculation of stresses, strains, elastic parameters and failure parameters (applied module: *NumPy*)
- calculation of parameters for the adaptation of the proposed yield function in Section 4.7 (applied module: *SciPy*)
- the plotting of graphs (applied module: *Matplotlib*)

The 3D-DIC has been performed for the three uniaxial tests (tension, compression and torsion) and for the multiaxial tests (compression-torsion test and tension-torsion test). For both types of multiaxial tests, the uniaxial preload reaches the 50% of the failure load, which was obtained previously for uniaxial tests.

4.2.1 3D-DIC by the 8-camera system

The distance of the cameras from the specimen is not a trivial issue and it is advisable to set the cameras as far as possible away from the specimen, by taking into account the available space around the UTM. If the cameras are put far away from the specimen, they would allow an increased overlap between shared fields of view of each cameras-pair, as can be seen in Fig. 4.4.
The resulting composition of the cylindrical geometry (from the images acquired by each camera) and its unwrapping are shown in Fig. 4.5, in which can be seen that 360° of the specimen surface cannot be effectively monitored, i.e. a wedge of the cylindrical surface appears black, as well as further black spots on the upper part can be seen. The black parts on the map are areas in which the speckle pattern is not detected by the software because of the occurring glares. The unwrapping of the cylindrical specimen is done by the software *h5pyViewer*® developed by Thierry Zamofing (Paul Scherrer Institute, Switzerland). For some tests, the inclusion of the beginning of the specimen conical part in the ROI is advisable in order to identify arising deformation bands more clearly.
The positioning of the cameras in a rectangular frame (as shown in Fig. 4.6) was applied in preliminary investigations of the author. The speckled wedges of the specimen, which are exposed between two adjacent pairs of cameras, are not fully detected. This is mainly due to the rectangular frame, that does not allow a precise positioning of cameras and thus, a proper overlap between the shared fields of view of two contiguous cameras-pairs cannot be accomplished.

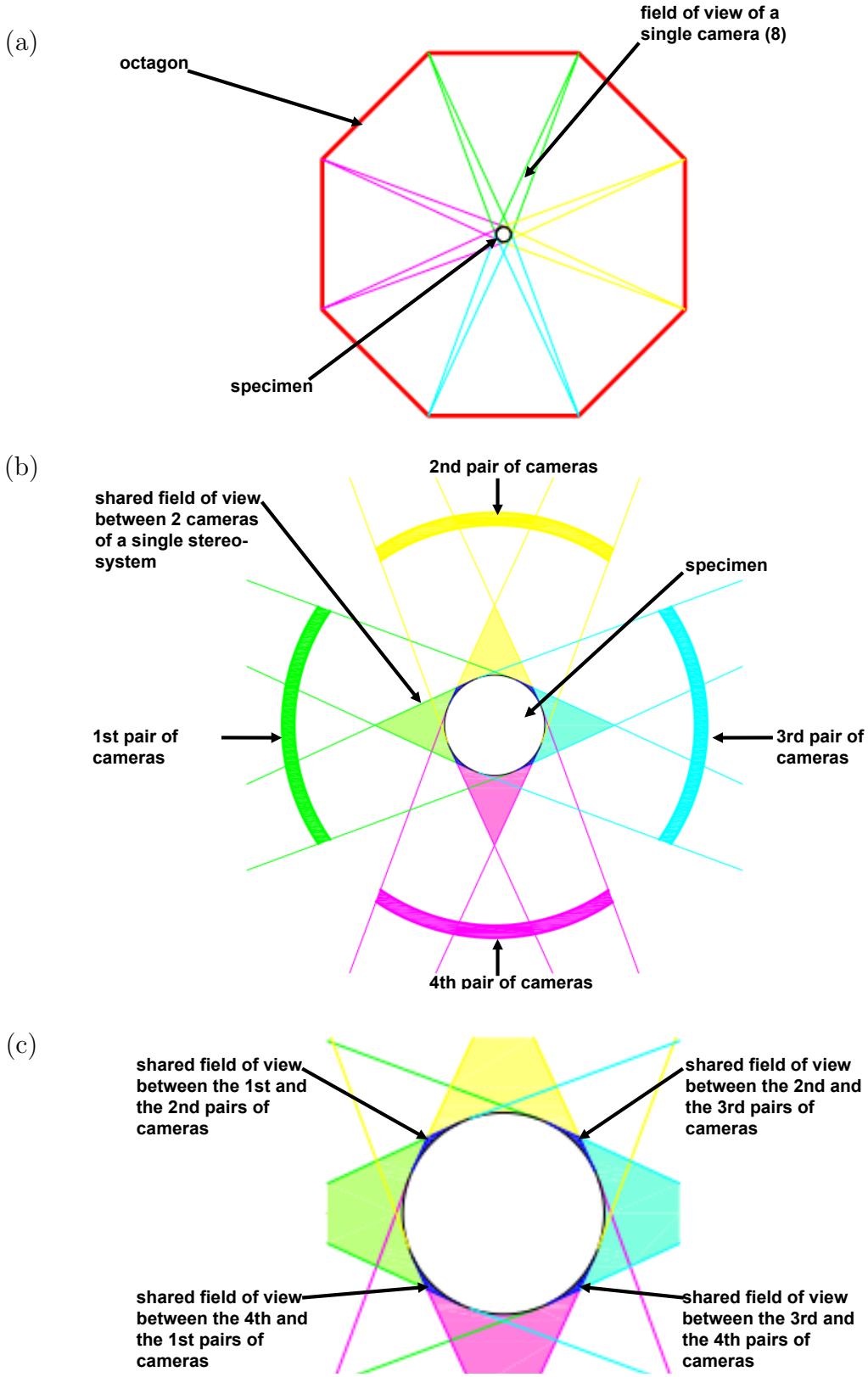

Figure 4.4: The octagon of the experimental set-up with reference to the field of view for each camera (a). The magnification of the specimen with the shared fields of view between the cameras of each pair (b) and the shared fields of view between cameras-pairs (c).

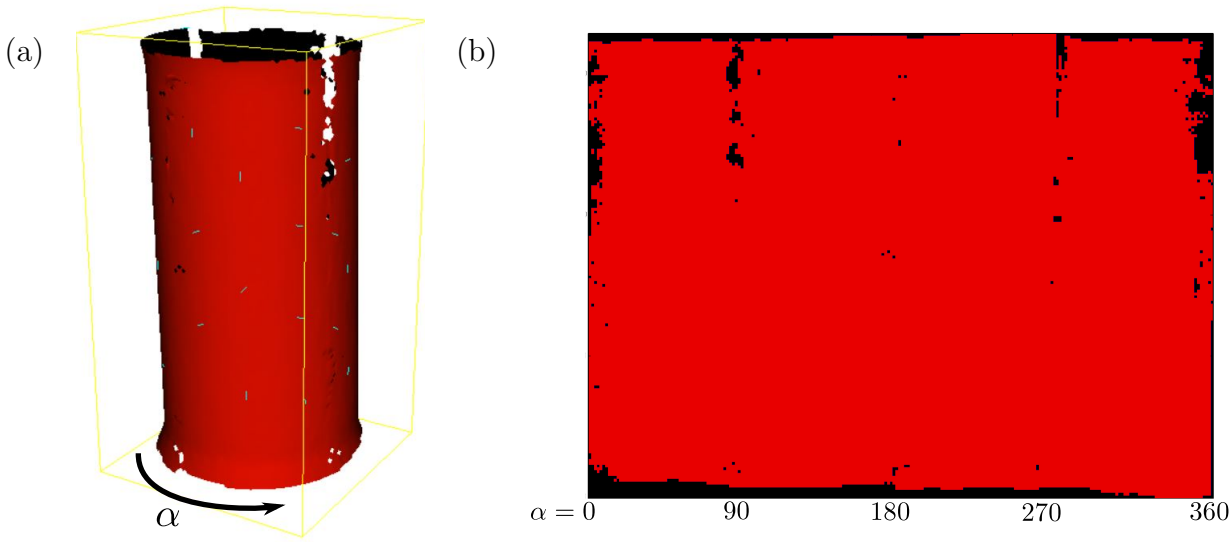

Figure 4.5: Composition of the undeformed specimen geometry by the 8-camera system (a) and its unwrapping (b), taken from Concas et al. [23].

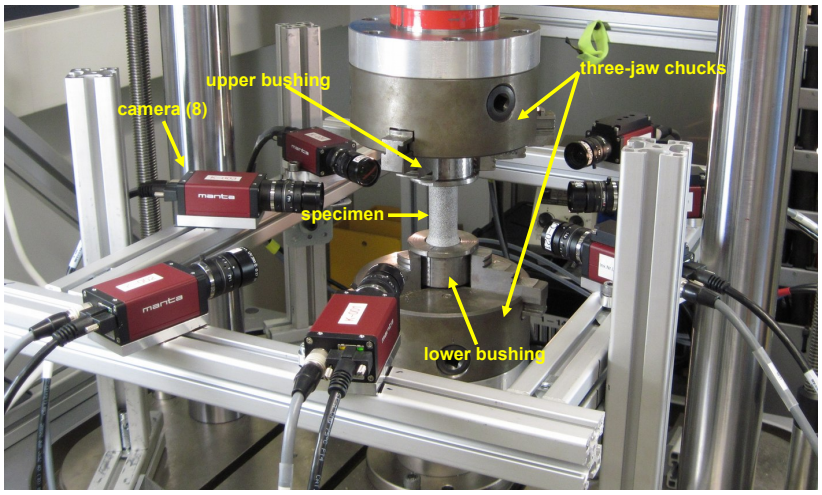

Figure 4.6: Experimental set-up with the rectangular cameras frame for the previous investigations.

Therefore, the author decided to apply the octagonal configuration of the cameras whereby the overlap between the fields of view can be achieved (see Fig. 4.4). However, the positioning of the cameras far away from the specimen leads to concerns on the speckle pattern. More precisely, a commonly used speckle pattern becomes aliased, i.e. by distancing the cameras from the specimen, the size of the speckle is too small to be correctly sampled by the cameras with their resolution [89]. An aliased speckle pattern alters the final strain map by occurrence of several ripples [24], that could be even misinterpreted as deformation bands. In Fig. 4.7 (a)

an aliased speckle pattern applied on a specimen is shown. In preliminary tests, the usage of a similar speckle pattern was acceptable with the rectangular cameras frame, because the cameras were still near enough to the specimen. By using the octagonal cameras frame and the same speckle size, the consequent local Lagrangian vertical strain map for a tension test is shown in Fig. 4.7 (b), where curved strain contour lines bands can be noticed.

(a)

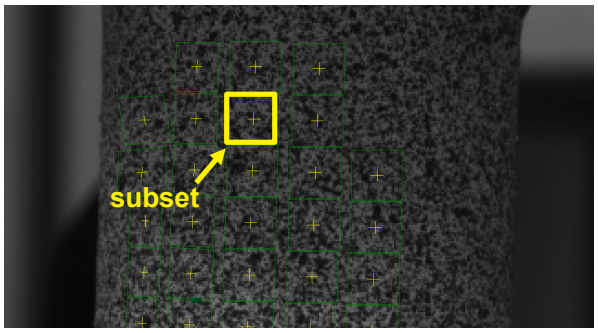

(b)

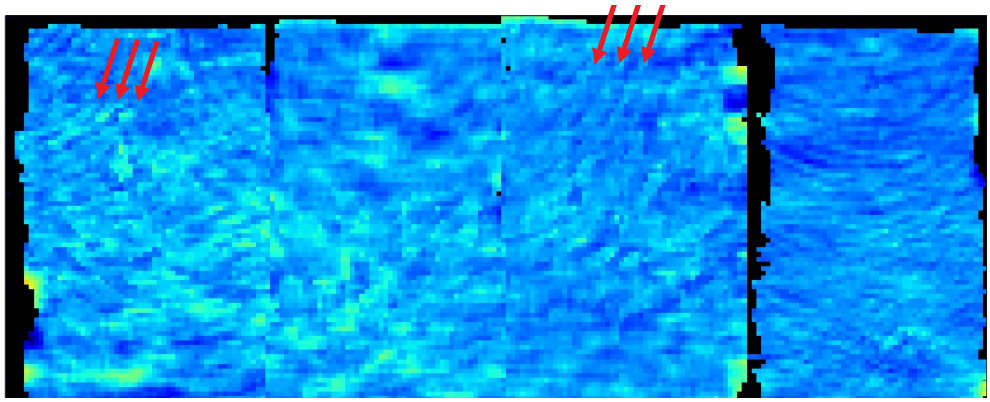

Figure 4.7: A specimen with an aliased speckle pattern, in which a subset is highlighted (a) and the resulting local Lagrangian vertical strain map for the tension test, where the small waves produced by the aliased speckle are highlighted (b).

According to Reu [89], a minimal size of three pixels for each speckle has to be achieved, in order to prevent aliasing. Hence, several attempts have been done for increasing the speckle size. Despite obtaining the desired speckle size, accomplishing such a size uniformly on the specimen surface is very difficult by using the aerosol spray for speckling. Unfortunately, no other speckling methods are suitable for this purpose. After further several attempts, the optimal speckle size appears to be approximately five pixels, as shown in Fig. 4.8 (b).

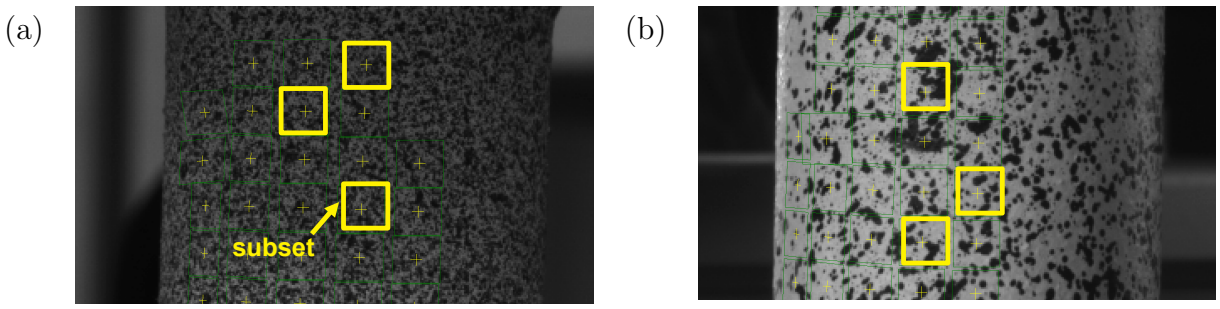

Figure 4.8: The speckle pattern applied previously, which results to be aliased by using the octagonal cameras frame (a) and the final speckle pattern (b). In both images few subsets are highlighted.

A way for weakening effects of an aliased speckle pattern is the application of a Gaussian filter, that is an available tool in Istra 4D [30]. The Gaussian filter removes noise and details by blurring the image, i.e. it is a low pass filter [102, 111]. A 3D-DIC analysis with the application of the Gaussian filter was performed on a specimen subjected to tensile loading with an aliased speckle pattern. By taking into account the last step prior to the failure, Fig.4.9 shows the different results for the local Lagrangian vertical strain map which are obtained by a common 3D-DIC analysis (Fig.4.9 (a)) and an analysis with the application of the Gaussian filter (Fig.4.9 (b)). Effects of the aliasing are visible in the upper part of Fig.4.9 (a), where vertical contour lines can be seen. Vertical contour lines are incompatible with this loading case and the strain considered, i.e. Lagrangian vertical strain. After applying the Gaussian filter, vertical contour lines disappear, strain gradients are minor and deformation bands are smooth and wavy. Furthermore, less black parts are observed in the strain maps and thus, the detection of subsets is also improved. For the sake of achieving more precise results, the Gaussian filter is not applied in the following analyses and aliasing is simply prevented by using the speckle pattern in Fig.4.8 (b). A proper resolution is obtained by a great overlap of the subsets with each other. The application of this new speckle for the 3D-DIC leads as well to wavy deformation bands in local Lagrangian vertical strain fields for the tensile tests, as described in Section 4.4. It is worth noting that a misalignment of the bushing occurred in the tension test, whose strain maps are shown in Fig. 4.9. This can be noticed by the higher strain gradients in the right part of both strain maps of Fig. 4.9

Since the software for the 3D-DIC analysis requires the user to define start points for the evaluation, four cross-shaped marks have been added approximately every 90° on the cylindrical speckled surface, as can be seen in the magnification of the

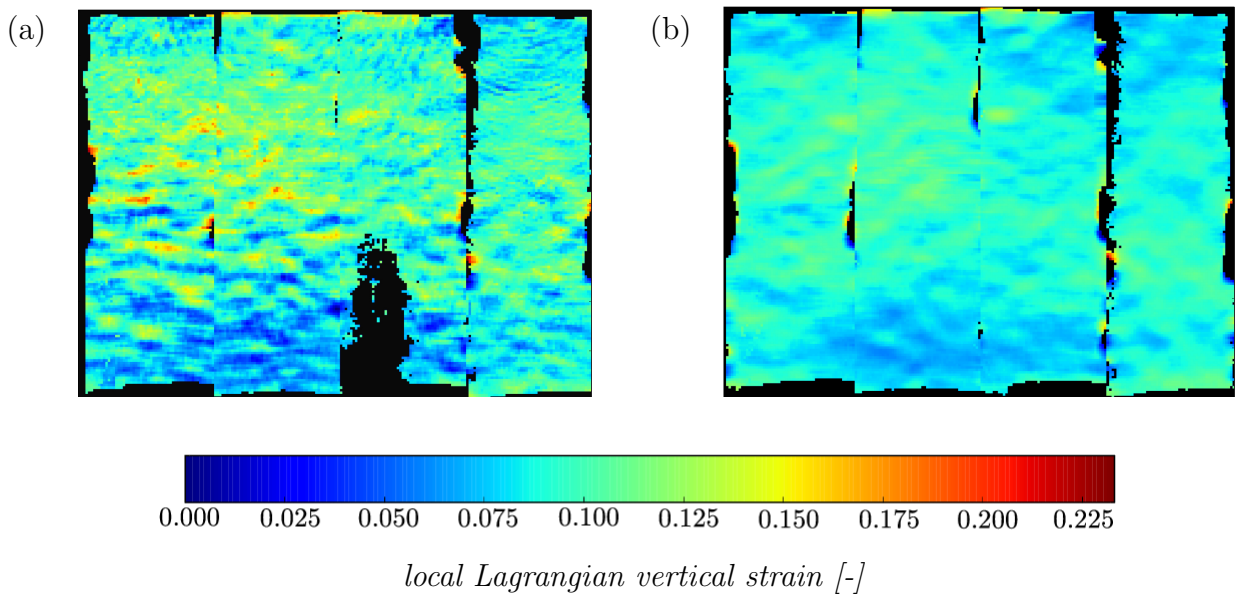

Figure 4.9: Resulting local Lagrangian vertical strain fields from a common 3D-DIC evaluation (a) and a 3D-DIC evaluation with the Gaussian filter.

specimen in Fig. 4.3 (a) and in Fig. 4.8 (b).

Position of light sources is crucial for an efficient 3D-DIC analysis and for avoiding the flickering of the light, which would occur by using only the ceiling light. Light sources are put as shown in Fig. 4.10.

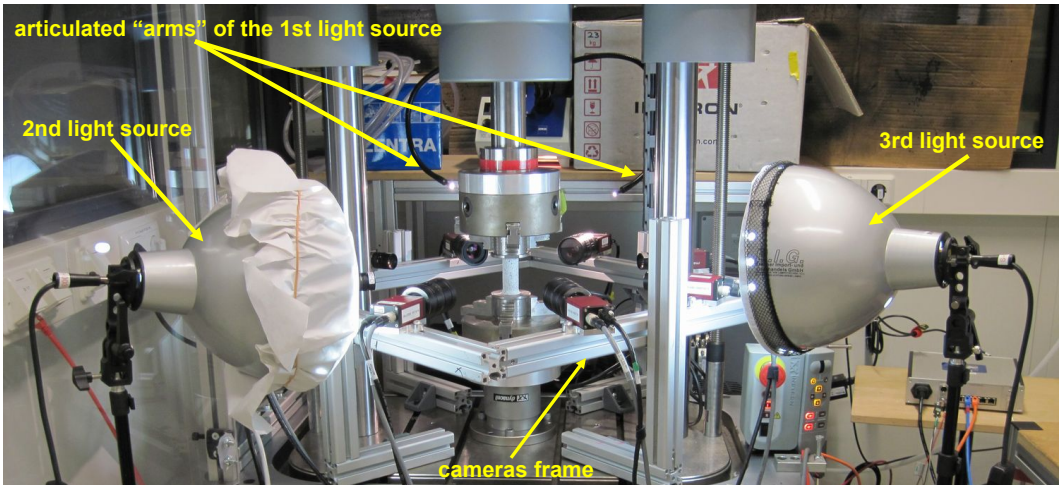

Figure 4.10: Position of light sources.

It allows the most uniform illumination of the specimen surface for this experimental set-up. Nonetheless, few glares persist because of the vicinity of the lamps to the specimen and unavoidable reflections of the light through the test rig.

Fig. 4.11 shows a comparison between the illumination done by ceiling light and lamps. Ceiling lights allow evidently a uniform illumination of the specimen, but they are not used in the following analyses because of the flickering's issue.

(a) (b)

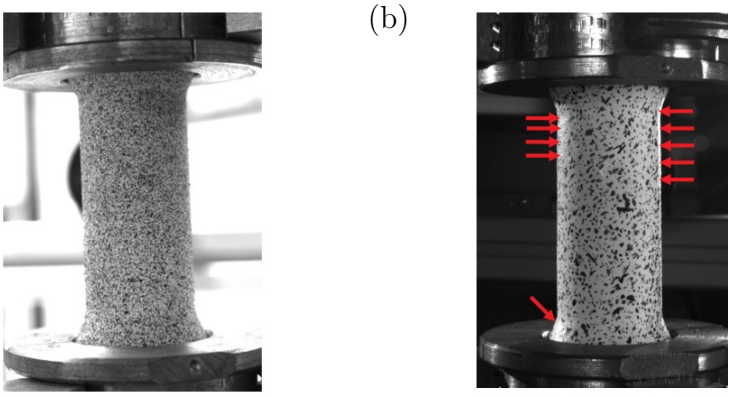

Figure 4.11: Illumination of the specimen achieved by the ceiling lights (a) and lamps free from flickering effects with occurring glares highlighted by red arrows (b). Glares have a detrimental effect on the correlation procedure.

4.3 Calculation of parameters from tests

In case of tensile and compression loading, the average stresses σ are calculated by

$$\sigma = \frac{F}{A}\,. \tag{4.2}$$

F is the applied force to the specimen. A is the cross-section area of the specimen. Global strains are given by the Green-Lagrange formulation, already mentioned in Section 3.1 (Eq. 3.1). The shear stress τ and the shear strain γ at the contour of the specimen's cross-section are obtained for torsional loading by

$$\tau = T\frac{r}{j} \tag{4.3}$$

and

$$\gamma = \pi\theta\frac{r}{L}\,, \tag{4.4}$$

respectively. T is the applied torque, r is the radius of the cylindrical specimen, j is the polar moment of inertia and θ indicates the shear angle. Since the shear stress is calculated for the contour of the specimen's cross-section, the radius is maximum and thus, also the obtained shear stress is maximum. Stress and strain values are obtained from data registered by the *Instron WaveMatrix* software during tests.

The elastic moduli, i.e. Young's modulus, compressive modulus and shear modulus, are calculated from the slope of the initial elastic part of the stress-strain curve [23]. According to the works of Jung and Diebels [64, 65], failure data are collected in the invariants plane $\sqrt{J_2} - I_1$, where I_1 is defined as first principal invariant and $\sqrt{J_2}$ is the squared root of the second deviatoric invariant. Details on the calculation of both invariants are given in Subsection 4.7.1.

4.4 Compression and tensile tests

Both tensile and compression tests have been conducted by displacement control of the actuator with a speed of 0.1 mm/s on a Divinycell® HP100 PVC foam in the in-plane direction. Stress-strain curves for both loading cases are shown in Fig. 4.12 for three specimens, i.e. three tests for each loading case. The failure parameters and the elastic moduli are reported in Table 4.1. Because of the different foam response to a compression load and a tensile load, the peak yield stress (which is evident in Fig. 4.12) is considered as failure limit for compression tests. The tensile stress, that leads to the fracture of the specimen, is taken as failure limit for tensile tests. No fracture of the specimen arises in compressive loading. Therefore, the compression tests are stopped once a distance of 3 mm from the lower limit switch is reached by the actuator.

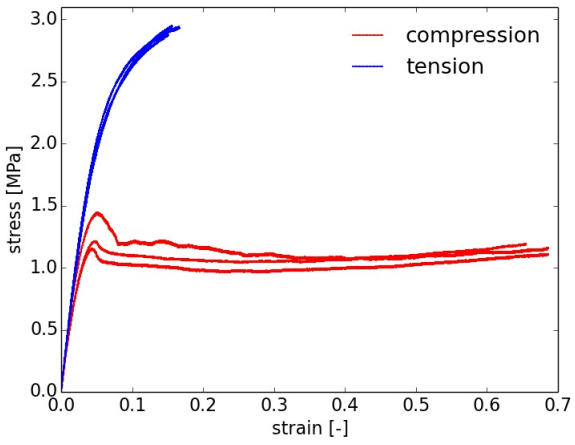

Figure 4.12: Tensile stress-strain curves and compressive stress-strain curves of the H100 foam loaded in the in-plane direction, according to Concas et al. [23]

	Compression	Tension
Failure load $F_F\,[N]$	624.41 ± 61.53	1433.42 ± 14.82
Failure stress $\sigma_F\,[MPa]$	1.27 ± 0.13	2.92 ± 0.03
Elastic modulus $E\,[MPa]$	52.82 ± 5.62	53.24 ± 1.61

Table 4.1: Means and standard deviations of the failure load, the failure stress and the elastic modulus for three specimens subjected to compression and tensile loading, respectively [23].

By comparing the curves of Fig. 4.12, the lower reproducibility of compression tests is evident. From Table 4.1 standard deviations are about 10% of the mean values of the failure limit and the compressive modulus. The low reproducibility is likely to be related to the unavoidable usage of different brands of varnishes, which were applied to the specimens for performing the 3D-DIC. The tensile tests show a better reproducibility than the compression tests. The highest standard deviation is reached for the Young's modulus as 3% of the mean value. The tensile failure load is 230% higher than the compressive failure load. Whereas the elastic moduli are similar for the two loading cases in terms of the mean values and the standard deviations. The reported values concern the in-plane properties. Since the manufacturer [34] provided values regarding the through-thickness direction, a comparison with such data cannot be done.

In Fig. 4.13 an image of the specimen prior to testing and further images related to five different global strain values of the compressive stress-strain diagram are depicted. The five global strain values are taken by considering the elastic stage, the peak yield point and three point in the plateau stage. The buckling of the specimen is observed for the third global strain value, i.e. at the beginning of the plateau.

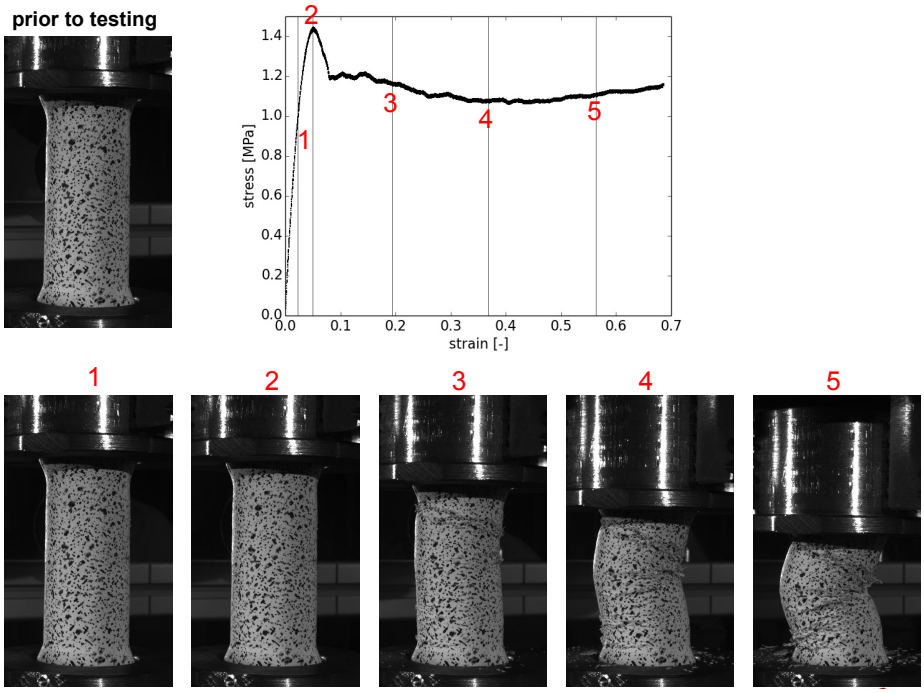

Figure 4.13: Images acquired by one camera during five different stages of the compression test and the relating compressive stress-strain diagram, according to Concas et al. [23].

Fig. 4.14 depicts the Lagrangian vertical strain fields on the unwrapped specimen for the above-mentioned five global strain values. Deformation bands are clearly detected at the third global strain stage (see Fig. 4.14 (c)), which corresponds with the first observation of the buckling. Deformation bands are horizontal in the lower part of the map, where the specimen is not buckled yet. Whereas higher strain gradients and a main curved deformation band can be seen in the upper part of the strain map and reveal the buckling in this part of the specimen. For the subsequent global strain stages (see Fig. 4.14 (d)-(e)), deformation bands merge with each other and areas of the specimen with positive strains can be clearly distinguished by other areas with negative strains, as the buckling of the specimen becomes severe. By inspecting the curving of the deformation bands, it is clear that they are always perpendicular to the generatrix of the cylinder. If the specimen is buckled, curved deformation bands are obtained. Because of the buckling, the subsets are greatly distorted and a gradual loss of the correlation is also noticed.

The 3D-DIC method is used also for the analysis of the tensile test. Fig. 4.15 (a) shows the relating stress-strain diagram and the images of the specimen prior to testing and after the failure. The five global strain values are chosen by dividing the amount of acquired images by five and taking into account also the last acquired image, which directly precedes the failure of the specimen. The specimen has a

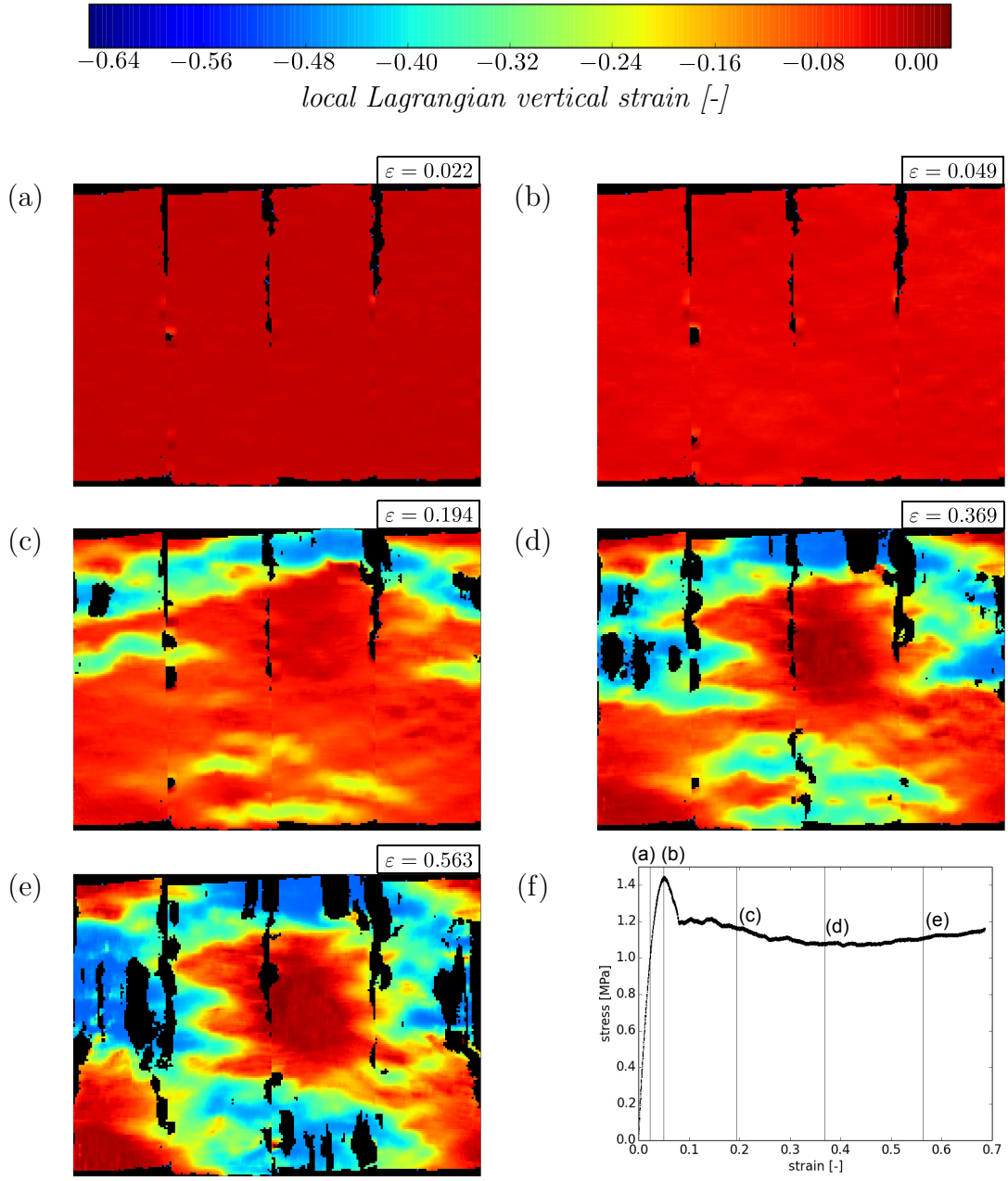

Figure 4.14: Local Lagrangian vertical strain maps (a)-(e) for five global strain values taken from the compressive stress-strain curve (f), according to Concas et al. [23].

typical brittle failure under tensile loading. The fracture is perpendicular to the loading axis, in line with the tests reported by Christensen et el. [21]. Camera images of the specimen during the above-mentioned global strain stages are omitted, because the specimen does not exhibit any clearly visible deformation, due to the brittle response.

In Fig. 4.15 (b)-(f) the local Lagrangian vertical strain maps are depicted for five global strain stages. In all tests, the fracture of the specimen arises approximately

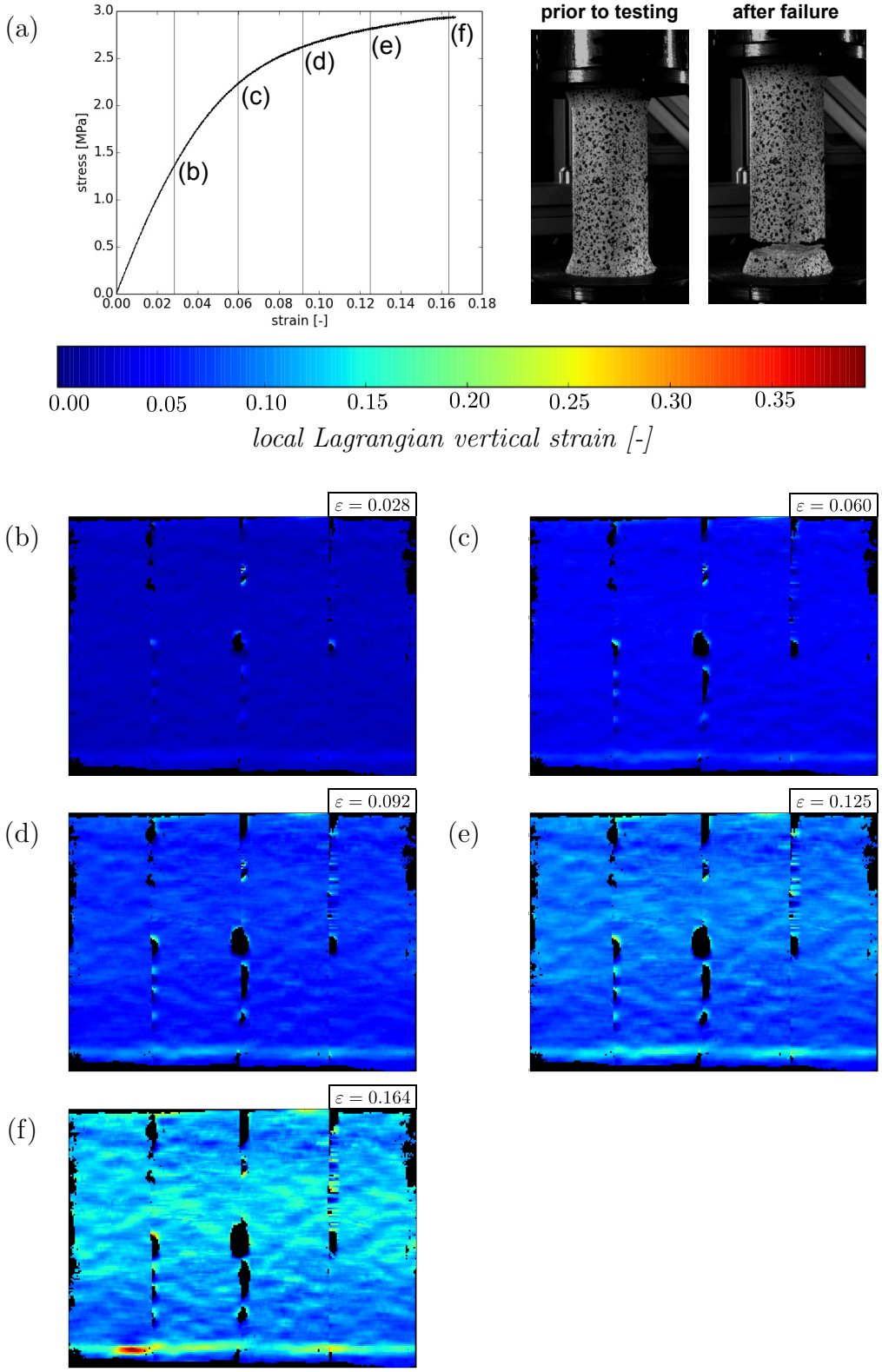

Figure 4.15: The tensile stress-strain curve and images of the specimen prior to testing and after failure (a) with reference to the local Lagrangian vertical strain maps (b)-(f) for five global strain values, according to Concas et al. [23]

at the end of the cylindrical part of the specimen and near the conical part. Thus, the beginning of the conical part of the specimen is included in the ROI for the 3D-DIC analysis, as mentioned in Section 4.2. A main deformation band, that is perpendicular to the specimen axis, is observed in the lower part of the strain maps. Whereas wavy deformation bands with minor strain gradients arise in the upper-central part of the strain map.

A misalignment of the bushing is not uncommon prior to the failure of the specimen under tensile loading. However, no misalignment occurs during the reported tensile tests. An unnoticeable misalignment of the bushings could be detected by examining the local Lagrangian vertical strain maps. More precisely, if the bushing were misaligned or moved from their initial position, the strain map given by a single cameras-pair would be different from the strain map of another cameras-pair. As is evident from Fig. 4.15 (b)-(f), the four cameras-pairs give back strain maps which are consistent with each other. Hence, neither misalignments nor movements of the bushings from their initial position occur for the presented tensile test.

It is worth to mention that the local Lagrangian vertical strain maps in Fig 4.15 (f) cannot be compared with the maps in Fig. 4.9, because in the latter the beginning of the conical part of the specimen was not included in the ROI, therefore the relating scale bars are different. Furthermore, a slight misalignment of the bushings occurs, as mentioned in Subsection 4.2.1.

4.5 Torsion tests

Torsion tests have been performed on the specimen presented in Section 4.1 by rotational control of the actuator with an angular velocity of 0.5 deg/s up to the failure. The shear stress-shear strain diagrams for three tests are shown in Fig. 4.16. The mechanical behaviour under torsional loading is similar to the tensile response, i.e. characterised by a brittle fracture. As can be seen in Fig. 4.16, one of the curves reaches higher shear strains prior to failure in comparison with the others. It is worth to mention that the bushings were neither misaligned nor moved, Indeed, if the bushings were placed correctly on the specimen prior to the test, such misalignments cannot happen during torsion tests unlike tension tests. However, for some specimens the varnish applied on the cylindrical part of the specimen occasionally leaked to its lower conical part. Hence, it is conceivable that this very thin coating of varnish could have a lubricant effect on the contact between bushings and the gripped part of the specimen and thereby allowing a very slight rotation of the specimen into the bushings during torsion. Nevertheless, the shear stress-shear strain curve is consistent with other torsion tests in terms of shear moduli and failure loads. Therefore, the test was accepted.

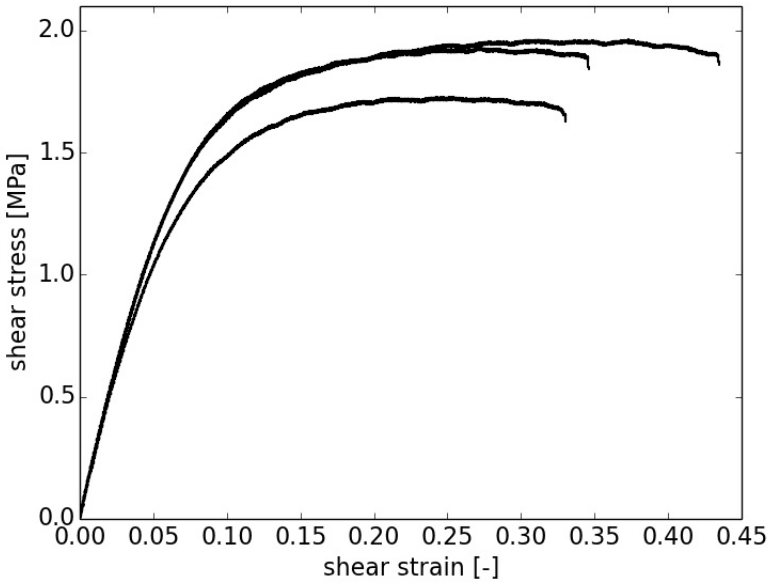

Figure 4.16: Shear stress-shear strain curves for three specimens subjected to torsional loading, according to Concas et al. [23].

Failure and elastic parameters are listed in Table 4.2. The highest standard deviations are found for the failure torque and the failure shear stress, for which the standard deviation is almost the 6% of the average value. However, this

	Torsion
Failure torque $T_F\,[Nm]$	5.44 ± 0.32
Failure shear stress $\tau_F\,[MPa]$	1.77 ± 0.10
Shear modulus $G\,[MPa]$	28.97 ± 1.28

Table 4.2: Means and standard deviations of the failure torque, the failure shear stress and the shear modulus for three specimens subjected to torsion load [23].

demonstrates that torsion tests are more reproducible than compression tests, in which the standard deviations are about 10% of the mean values, as described in Section 4.4.

The torsion test concerning the diagram with the abnormal elongation is monitored by the 3D-DIC method. The relating Lagrangian tangential shear strain maps are shown in Fig. 4.17 (b)-(f) on the unwrapped specimen geometry. Like tensile tests, the five stages are established by dividing the amount of acquired images by five and taking into account the image which precedes failure. The five global strain stages are highlighted in Fig. 4.17 (a). Furthermore, camera images of the specimen for each global strain stage are omitted also for this loading case, since no deformation can be noticed by the eye during the test. Hence, camera images of the specimen prior to testing and after the failure are depicted in Fig. 4.17 (a). As can be seen from the diagram in Fig. 4.17 (a), the fifth strain map does not represent the strain map immediately prior to the failure of the specimen, but it concerns few step earlier. After the fifth global strain stage, the correlation is not achieved anymore.

Deformation bands appear tilted with minor strain gradients in the second global strain stage. From the third stage, deformation bands with increasing strain gradients are clearly gathered in two diametrically opposite wedges of the specimen. By the following stages, the deformation bands become more tilted and it can be also noticed the expanding black areas in the strain maps, i.e. the gradual disappearance of subsets. A large number of subsets are not detected by the software because of their exit from the shared field of view of each cameras-pair.

The failure of the specimen arises in the lower end of the specimen. The fracture propagates as a helix on the specimen surface towards the upper end, as can be seen in Fig. 4.17 (a). Since the highest strain gradients and the deformation bands are found in the upper-central part of the specimen (consistently with the rotating upper actuator), no sign of the incipient fracture of the specimen can be observed

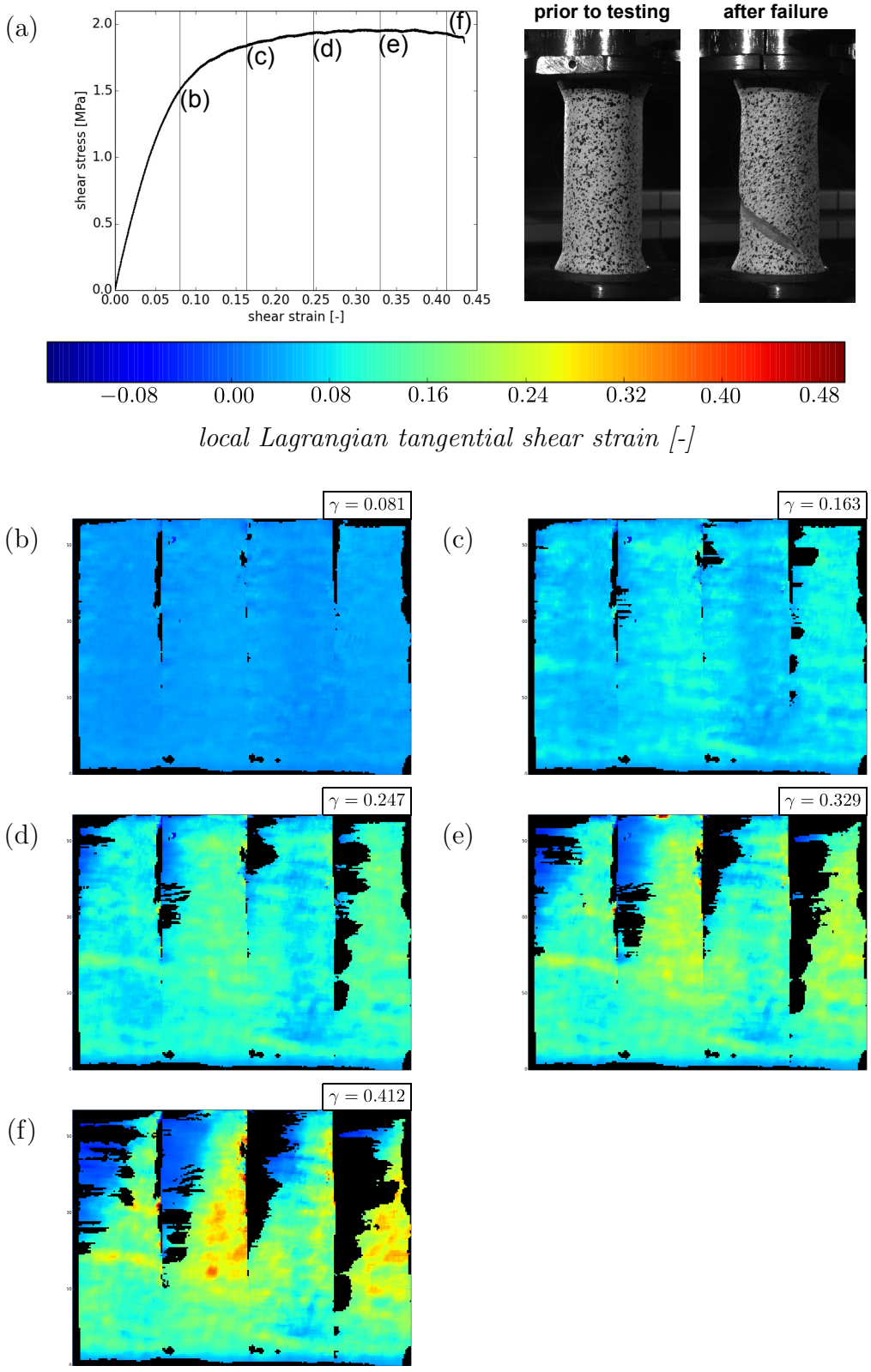

Figure 4.17: The torsion stress-strain curve and images of the specimen prior to testing and after failure (a) with reference to the local Lagrangian tangential shear strain maps (b)-(f) for five global shear strain values, according to Concas et al.[23].

through examination of the strain maps in Fig. 4.17. Thus, it can be concluded that the torsional failure is mainly influenced by distortions, which are linked to surface stresses instead of the torsional loading itself.

4.6 Combined compression-torsion and tensile-torsion tests

In Fig. 4.18 shear stress-shear strain diagrams for combined compression-torsion and combined tension-torsion tests are depicted. For combined compression-torsion tests, a percentage of the compressive failure load obtained from compression tests is applied as preload. Three different percentages are considered: 25%, 50% and 75%. The preload is applied by the actuator driven in load control. Afterwards, the torsional loading is superimposed by the actuator driven in rotational control, keeping the axial load constant.
The procedure is analogous for combined tensile-torsional tests. A further percentage of 90% of the tensile failure load is applied, since preliminary tests showed that the failure surface was extended towards the positive axis of the first principal invariants [23]. Hence, further failure data in this direction would allow to outline properly the failure surface.
For combined compression-torsion tests, a peak prior to the plateau is evident. Thus, the peak yield stress is considered as failure limit for this loading case. Plateau stages in Fig. 4.18 (a) appear greatly scattered also for the same percentage of the preload. A scatter of the peak yield stress is also evident. The growing percentage of the compressive preload causes gradually lower peak yield stresses. Since no fracture occurs in the specimen, the test is stopped once the limit switch is reached.
Combined tensile-torsional tests are clearly more reproducible. Shear stress-shear strain diagrams with percentages of 25% and 50% can be even overlapped to each other. Similar to combined compression-torsion tests, the increasing percentage of the tensile preloading leads to gradually lower failure stresses. Since the material exhibits a brittle behaviour for this loading case (as for tension and torsion tests), the failure limit is the stress which leads the specimen to the fracture.

Fig. 4.19 shows images of the specimen taken during a combined compression-torsional test, in which the preload reaches the 50% of the compressive failure stress. It is evident that the specimen does not undergo buckling for this loading case. Each image is related to a single global strain value. The five global strain stages are taken as follows

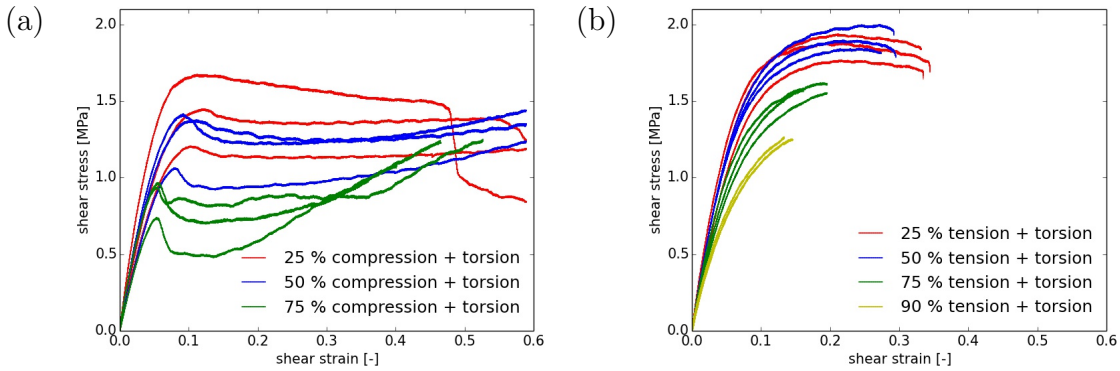

Figure 4.18: Shear stress-shear strain curves for specimens subjected to different percentages of compression loading (a) and tensile loading (b) as preload, respectively and the subsequent torsion, according to Concas et al. [23].

- the first global strain value is taken from the stress-strain diagram concerning the compressive preloading,
- the second global strain value is taken from the elastic stage during superposition of the torsional loading,

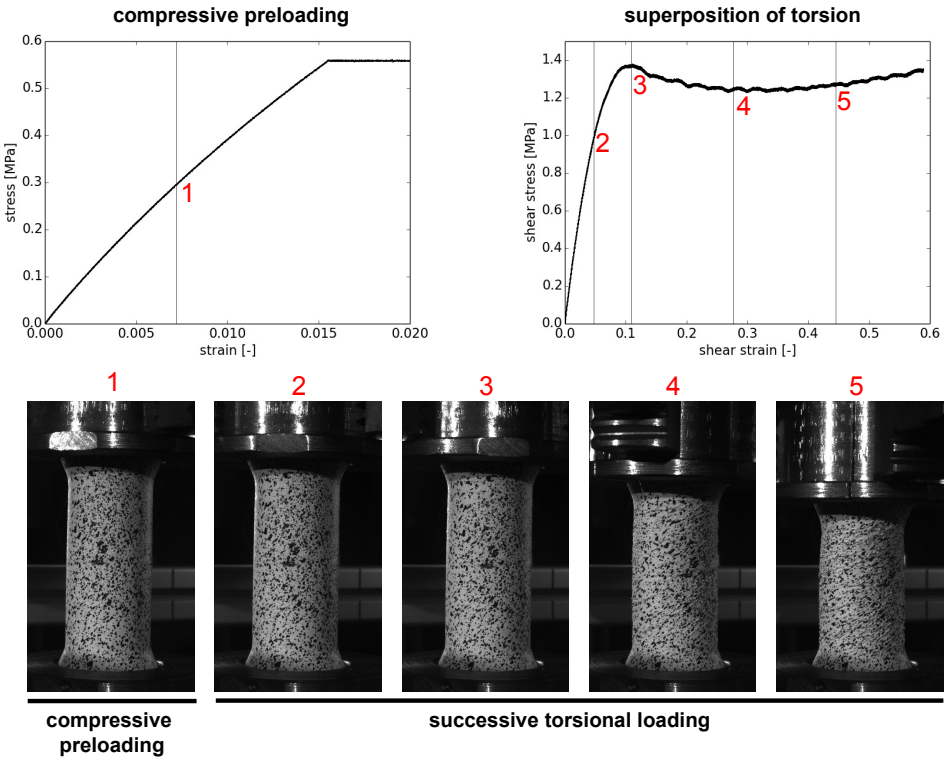

Figure 4.19: Images acquired by one camera for five global strain stages of the combined compression-torsion test, reaching the 50% of the peak yield load, according to Concas et al. [23].

- the third global strain value is set in the peak yield stress,
- the fourth and the fifth global strain values are taken from the plateau.

Strain fields obtained by the 3D-DIC are shown for the above-mentioned global strain values. The strain map for the first global strain stage is depicted in Fig. 4.20. Since only the compressive load is involved, the strain map concerns the Lagrangian vertical strain. Higher strain gradients are observed in the upper part of the specimen.

Fig. 4.21 shows the local Lagrangian tangential shear strain maps for the subsequent global strain values relating to the superposition of torsion. Although the compressive preload is applied, strain fields are similar to the strain fields for a torsional test, i.e. a localisation of deformation bands in the upper part of the specimen (consistently with the rotating actuator) is evident, as well as the gathering of deformation bands mainly in two diametrically opposed wedges of the specimen.

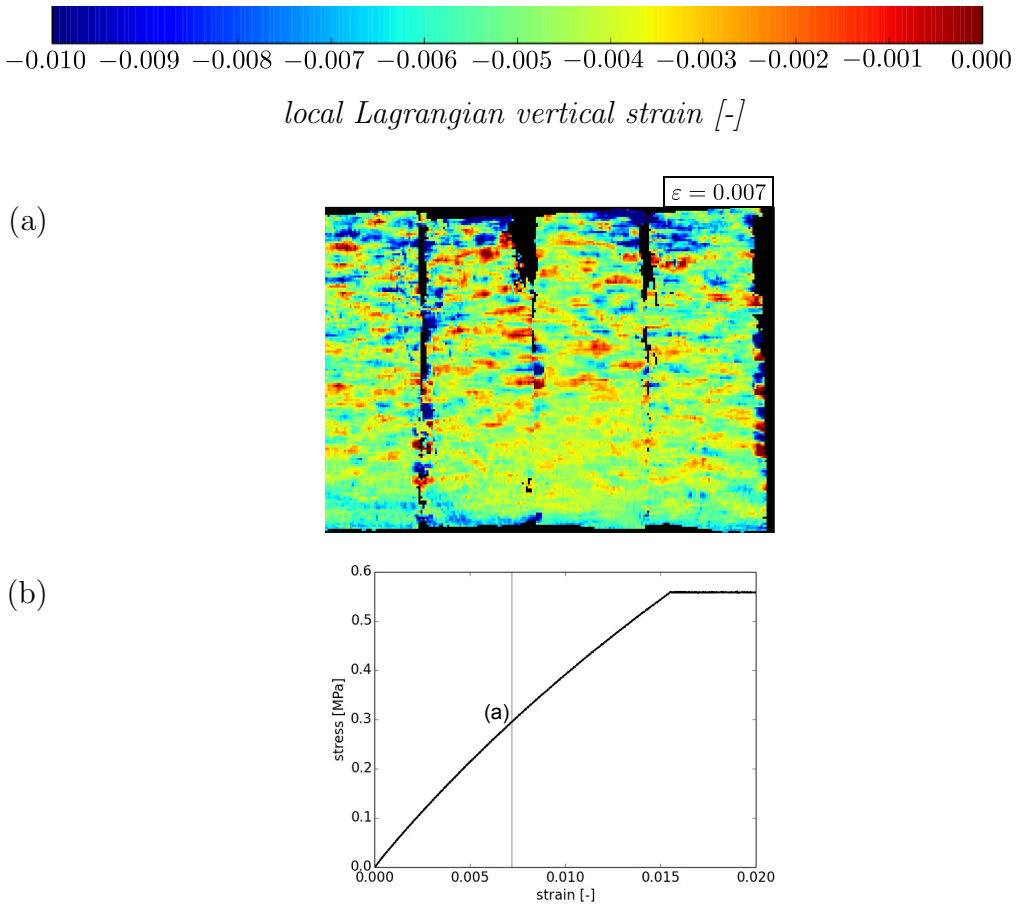

Figure 4.20: Local Lagrangian vertical strain map (a) for a global strain value taken from the compressive stress-strain curve relating to the compressive preloading (b), according to Concas et al. [23].

The gradual loss of detected subsets for the increasing global strain stages is a further similarity to torsion tests and it appears as even more remarkable than for a simple torsional loading because of the greater distortions, which are involved for the combined compression-torsional loading case.

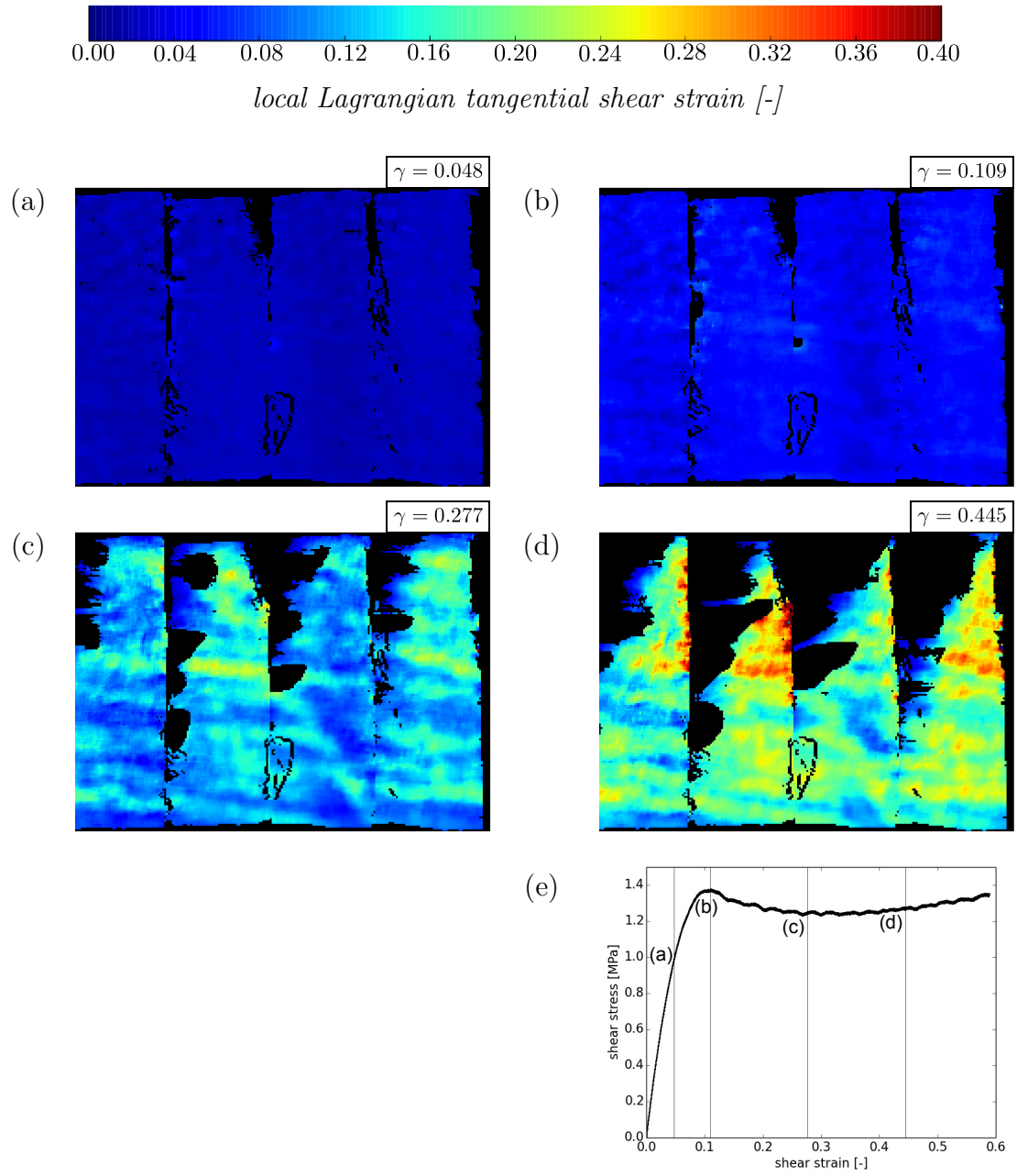

Figure 4.21: Local Lagrangian tangential shear strain maps (a)-(d) for four average shear strain values taken from the shear stress-shear strain curve (e), which concerns the superimposed torsional load, according to Concas et al. [23].

A combined tension-torsion test is monitored by the 3D-DIC method for determining strain fields. The global strain stages have been chosen again by

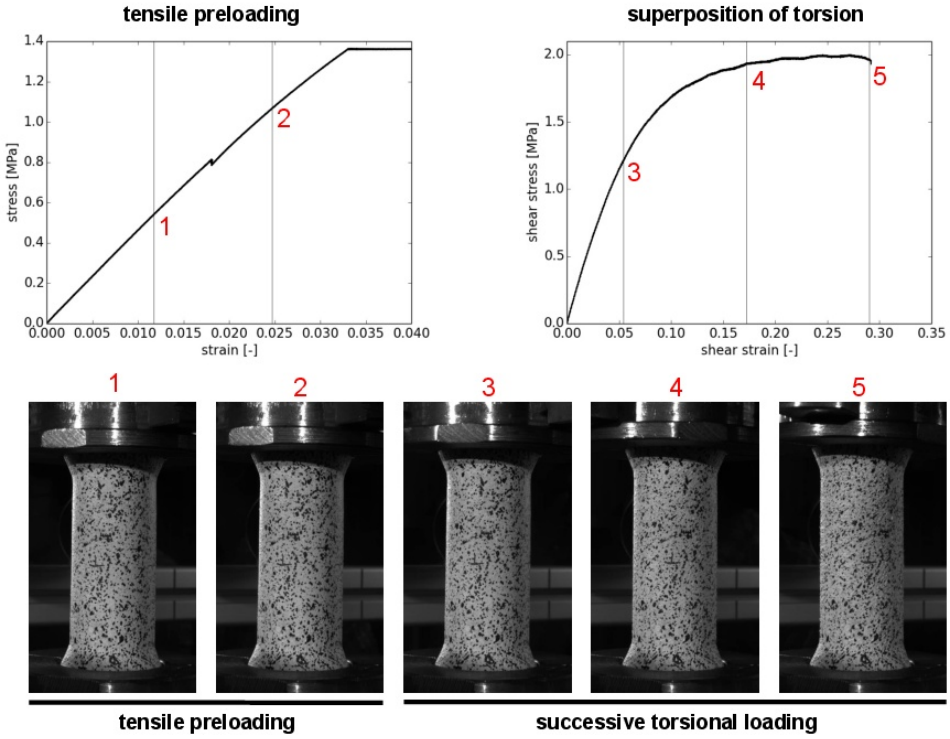

Figure 4.22: Five images acquired by one camera for five global strains values of the combined tension-torsion test, reaching the 50% of the tensile failure load, according to Concas et al. [23].

dividing into five the overall amount of acquired images and taking into account the last image prior to the failure. The images of the specimen acquired by a single camera are shown in Fig. 4.22 for each global strain stage. The two early global strain values concern the tensile preload performed by the actuator in load control up to reach 50% of the tensile failure load. The subsequent three global strain values relate the superposition of the torsion load, by keeping the tensile load constant. Unlike tensile and torsion tests, the gradual deformation of the specimen can be noticed in the above-mentioned camera images by observing the growing distortion of the speckle pattern at the centre of the specimen. The shear stress-shear strain diagram is congruent with torsional shear stress-shear strain diagrams as well as tensile stress-strain diagrams, because of the brittle response to this loading case.

Fig. 4.23 shows local Lagrangian vertical strain fields relating to the tensile preload of the specimen. A main deformation band is observed in the lower part of the specimen (see Fig. 4.23 (b)). It is perpendicular to the specimen axis. Whereas further deformation bands with minor strain gradients are gathered in the upper part. They exhibit a wavy trend, as already seen for the uniaxial tensile test.
A little step is noticed in the ramp of Fig. 4.23 (c). Since this abrupt decrease of the load is unnoticeable in the strain maps, it is likely to be due to a slight movement

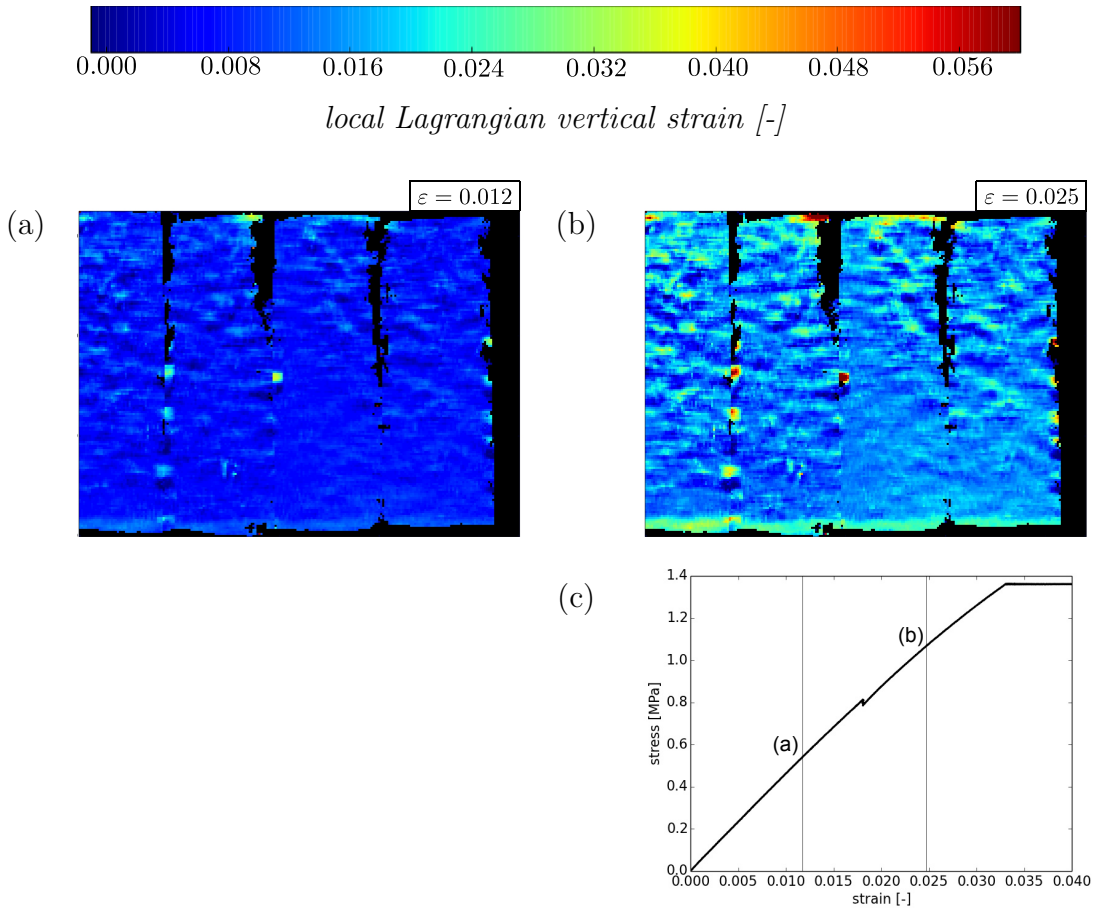

Figure 4.23: Local Lagrangian vertical strain maps (a)-(b) for two global strain values taken from the tensile preloading stress-strain curve (c), according to Concas et al. [23].

of the bushings for adapting into the jaws of the chuck. However, the test has been accepted, because its diagram is consistent with diagrams of others combined tensile-torsion tests, in which 50% of the tensile failure load is reached.

For the successive superposition of torsion, the local Lagrangian tangential shear strain maps are represented in Fig. 4.24. The disappearing of subsets in the strain maps occurs analogously to the strain map of the torsion test. The deformation bands can be detected for minor strain gradients in Fig. 4.24 (b). For this loading case, deformation bands are gathered in two diametrically opposed wedges of the specimen. This feature recurs for every loading case, in which a torsional loading is involved. Nonetheless, the highest strain gradient is observed in the deformation band at the lowest part of the specimen, as can be seen in Fig. 4.24 (c). It finds itself exactly where the fracture of the specimen arises. Fig. 4.25 represents two sides of the specimen after the above-mentioned test. The fracture starts as a typical tensile failure, with the crack propagating perpendicularly to the axis of the specimen. The subsequent propagation follows the path of an helix, i.e. the typical brittle torsional

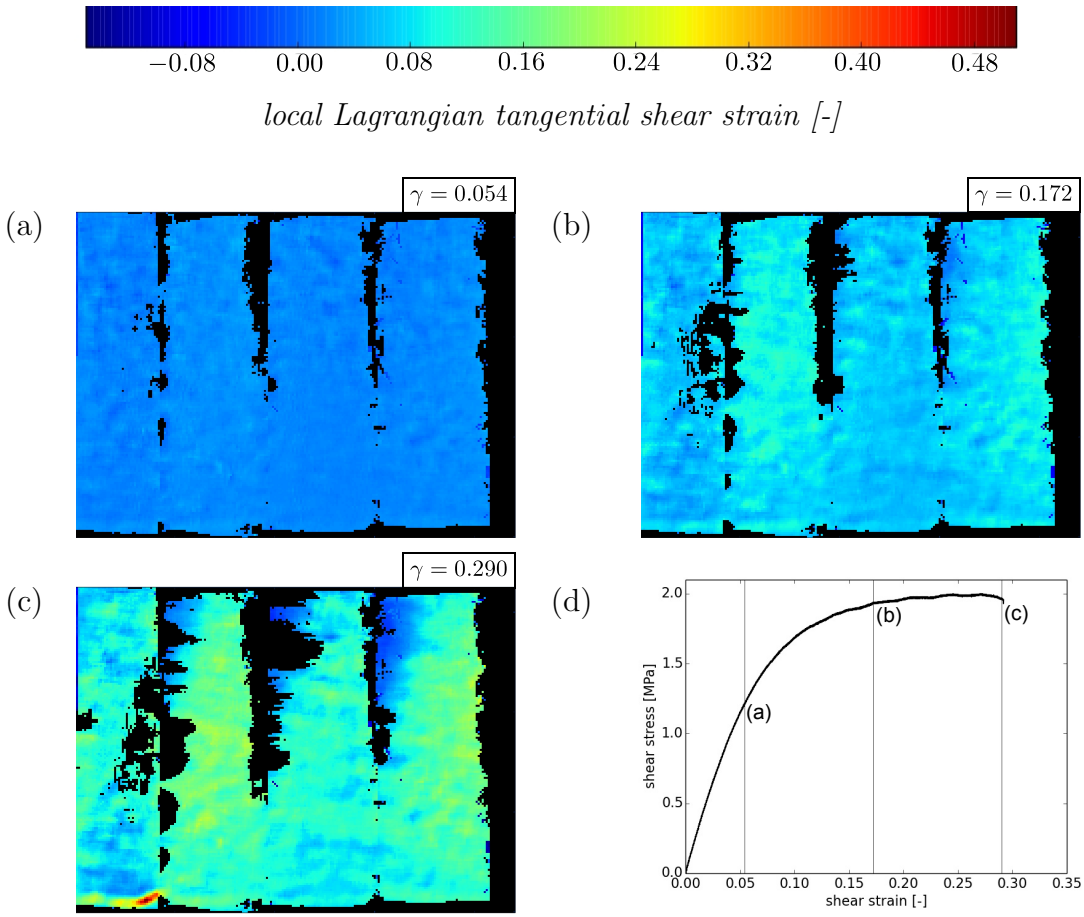

Figure 4.24: Local Lagrangian tangential shear strain maps (a)-(c) for three global shear strain values taken from the shear stress-shear strain curve (d), which concerns the superimposed torsional load, according to Concas et al. [23].

failure, as seen in Section 4.5.

Once the helix reaches the same generatrix of the cylinder, from which the first crack arises, the specimen breaks in three pieces.

By observation of the broken specimens after other combined tensile-torsional tests, it can be noticed that the pitch of the helix decreases for an increasing contribution of the tensile preload (percentages of 75% and 90% of the tensile failure limit as preload). In other words, the helix, on which the crack propagates, becomes more *flat*. For higher contributions of the torsional load (percentage of 25% of the tensile failure limit as preload), the pitch of the helix increases. The maximum pitch of the helix is observed for the torsional tests.

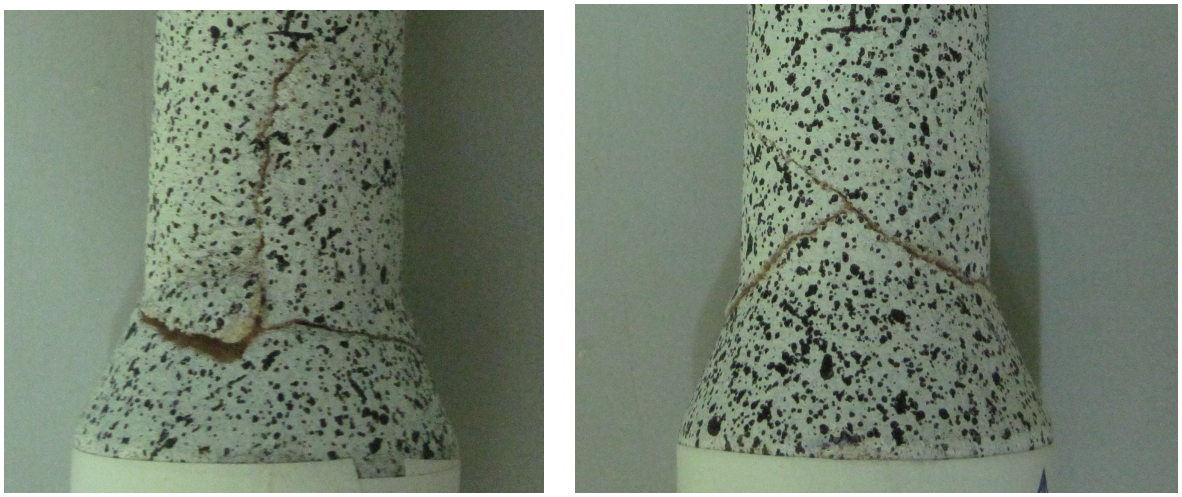

Figure 4.25: Two sides of the specimen's fracture under the combined tensile-torsional loading, preloaded with 50% of the tensile failure load.

4.7 Failure criterion

4.7.1 Stress tensor and invariants

The stress tensor $\boldsymbol{\sigma}$ is shown in Eq. 4.5. The relating axes are named x, y, z [68, 119] or x_1, x_2, x_3 [78]. Zienkiewicz and Taylor [125] defined the first nomenclature as *Cartesian indicial* form and the second nomenclature as *matrix* form. In this work, the *matrix* form is applied.

$$\boldsymbol{\sigma} = \begin{bmatrix} \sigma_{11} & \tau_{12} & \tau_{13} \\ \tau_{21} & \sigma_{22} & \tau_{23} \\ \tau_{31} & \tau_{32} & \sigma_{33} \end{bmatrix} . \tag{4.5}$$

By taking into account the hydrostatic stress σ_0

$$\sigma_0 = \frac{\sigma_{11} + \sigma_{22} + \sigma_{33}}{3} , \tag{4.6}$$

the deviatoric stress tensor $\boldsymbol{s}$ is given by

$$\boldsymbol{s} = \begin{bmatrix} \sigma_{11} - \sigma_0 & \tau_{12} & \tau_{13} \\ \tau_{21} & \sigma_{22} - \sigma_0 & \tau_{23} \\ \tau_{31} & \tau_{32} & \sigma_{33} - \sigma_0 \end{bmatrix} = \begin{bmatrix} s_{11} & s_{12} & s_{13} \\ s_{21} & s_{22} & s_{23} \\ s_{31} & s_{32} & s_{33} \end{bmatrix} . \tag{4.7}$$

The principal normal stress tensor is also introduced, in which the shear stresses are

equal to zero (see Eq. 4.8).

$$\boldsymbol{\sigma} = \begin{bmatrix} \sigma_1 & 0 & 0 \\ 0 & \sigma_2 & 0 \\ 0 & 0 & \sigma_3 \end{bmatrix} . \tag{4.8}$$

Principal normal stress values are obtained by calculating the roots [68, 85] of

$$\begin{vmatrix} \sigma_{11} - \lambda & \tau_{12} & \tau_{13} \\ \tau_{21} & \sigma_{22} - \lambda & \tau_{23} \\ \tau_{31} & \tau_{32} & \sigma_{33} - \lambda \end{vmatrix} = 0 . \tag{4.9}$$

Hence, the following polynomial is obtained [68, 125]

$$-\lambda^3 + I_1\lambda^2 + I_2\lambda + I_3 = 0 \tag{4.10}$$

as well as the polynomial

$$-\lambda^3 + J_2\lambda + J_3 = 0 , \tag{4.11}$$

concerning the deviatoric stresses. The yield function of Bier et al. [10, 11, 52], which is introduced in Subsection 4.7.2, is given as function of the first principal invariant

$$I_1 = \sigma_{ii} = \sigma_{11} + \sigma_{22} + \sigma_{33} = 3\sigma_0 \tag{4.12}$$

and the second deviatoric invariant

$$J_2 = \frac{1}{2} s_{ij} s_{ij} = \frac{1}{2} \left[s_{11}^2 + s_{22}^2 + s_{33}^2 + s_{12}^2 + s_{21}^2 + s_{23}^2 + s_{32}^2 + s_{31}^2 + s_{13}^2 \right] , \tag{4.13}$$

that can be written in this way

$$J_2 = \frac{1}{2} \left[(\sigma_{11} - \sigma_0)^2 + (\sigma_{22} - \sigma_0)^2 + (\sigma_{33} - \sigma_0)^2 + 2\tau_{12}^2 + 2\tau_{23}^2 + 2\tau_{31}^2 \right] . \tag{4.14}$$

In Eqs. 4.12-4.13, the invariants are also given according to the Einstein's summation convention [84].

Taking into account the applied loading cases, i.e. tension, compression, torsion,

combined tension-torsion and combined compression-torsion, the formulation of the hydrostatic stress is thus simplified

$$\sigma_0 = \frac{\sigma_{11} + \sigma_{22} + \sigma_{33}}{3} \rightarrow \sigma_0 = \frac{\sigma_{11}}{3}\,, \tag{4.15}$$

as well as the formulation of the first principal invariant

$$I_1 = 3\sigma_0 \rightarrow I_1 = \sigma_{11}\,. \tag{4.16}$$

The yield function of Bier et al. [10, 11, 52] includes the formulation of the squared root of the second deviatoric invariant

$$\begin{aligned} \sqrt{J_2} = \sqrt{\frac{1}{2}\left[(\sigma_{11}-\sigma_0)^2 + (\sigma_{22}-\sigma_0)^2 + (\sigma_{33}-\sigma_0)^2\right] + \tau_{12}^2 + \tau_{23}^2 + \tau_{31}^2} \\ \rightarrow \sqrt{J_2} = \sqrt{\frac{\sigma_{11}^2}{3} + \tau_{12}^2}\,, \end{aligned} \tag{4.17}$$

In the aforesaid formulations, σ_{11} is given by Eq. 4.2 and τ_{12} is obtained from Eq. 4.3.

4.7.2 Failure data and calculations of the parameters

The failure data presented in the previous Sections are gathered in the invariants plane $\sqrt{J_2} - I_1$, as shown in Fig. 4.26. It can be seen that the failure data concerning compression tests and combined compression-torsion tests exhibit generally a higher scatter than those relating tensile tests and combined tension-torsion tests. As mentioned in Section 4.4, it could be due to the usage of different brands of the varnish, which leads in some cases to the loss of fragments of the varnish coating, especially during the buckling of the specimen. Whereas tension tests feature an overlapping between failure data.

Fig. 4.26 shows the fitting of the failure data by means of the yield function presented by Bier et al. [10, 11, 52]. Such yield surface was conceived for reproducing the material behaviour of metal powder, which undergoes compaction processes [11]. The authors proposed its usage for granular materials, e.g. soils and concrete [11]. Its suitability was recently demonstrated by Jung and Diebels [64, 65] also for aluminium foams with smaller pore sizes, i.e. 20 ppi and 30 ppi. Such foams are characterised by an asymmetric yield surface, that can be fitted by the yield function of Bier et al. [10, 11, 52], unlike the aluminium foam with a greater pore size, i.e. 10 ppi, whose yield data are fitted by the yield function proposed by Green [49].

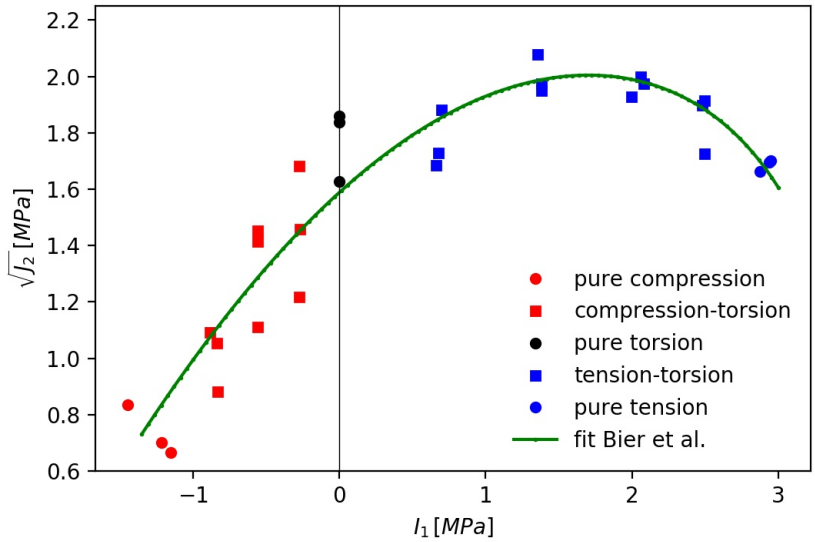

Figure 4.26: Failure data for the HP100 foam depicted on the invariants plane $\sqrt{J_2} - I_1$ and fitted by the yield criterion proposed by Bier et al. [11, 10, 52].

Since the tension-compression asymmetry of the PVC foam failure data is evident, the yield function of Bier et al. [10, 11, 52] is adapted, as shown in Fig. 4.26.

The fitting is done by means of a Python® script written by the author. In the script, the yield function of Bier et al. [10, 11, 52] is implemented as

$$F\left(I_1, \sqrt{J_2}\right) = ck\, ln\left(\frac{e^{g_1\left(I_1,\sqrt{J_2}\right)/(ck)} + e^{g_2\left(I_1,\sqrt{J_2}\right)/(ck)}}{2}\right). \tag{4.18}$$

The two functions $g_1\left(I_1, \sqrt{J_2}\right)$ and $g_2\left(I_1, \sqrt{J_2}\right)$ are defined by Bier and Hartmann [11] as follows:

$$g_1\left(I_1, \sqrt{J_2}\right) = \sqrt{J_2 + \alpha\left(I_1 - 3\xi\right)^2} - k \tag{4.19}$$

and

$$g_2\left(I_1, \sqrt{J_2}\right) = \sqrt{J_2} - A_1 + A_2 e^{A_3 I_1} \tag{4.20}$$

with the following functions defined as

$$\begin{aligned} A_1 &= k\,, \\ A_2 &= \frac{k}{\left(1-\sqrt{1-r^2}\right)^{I_0/((3\xi-I_0)(1+r))}}\,, \\ A_3 &= ln\left(k/A_2\right)/I_0\,, \\ k &= \sqrt{\alpha\left(I_0-3\xi\right)^2}\,. \end{aligned} \tag{4.21}$$

Thus, five independent parameters are identified, i.e. α, c, I_0, ξ, r.
An initial guess on the unknown parameters can be obtained by including trial-and-error values of the independent parameters on the Bier yield function, in order to fit roughly the experimental determined failure data. Once the first guess is obtained, then the above-mentioned self-written Python® script is applied. More precisely, the unknown parameters are evaluated by means of the *scipy.optimize* module, which involves the application of the least squares procedure with the *dogbox* method [115] and the first guess of the five independent parameters.
The resulting parameters are listed in Table 4.3 and the corresponding failure function is depicted in Fig. 4.26

α $[-]$	c $[MPa]$	I_0 $[MPa]$	ξ $[MPa]$	r $[-]$
1.065	-22.094	3.773	0.605	-0.547

Table 4.3: Parameters of the yield function of Bier et al. [10, 11, 52] obtained by the optimisation procedure, according to Concas et al. [23].

Two different types of failure are concerned for the PVC foam, i.e.

- the yielding for the compression and combined compression-torsion loading cases and
- the fracture for the tension, torsion and combined tension-torsion loading cases

(both failure types are preceded by a pseudo-elastic stage [4, 23, 45, 64]). This leads to the shifting of the failure surface towards the axis of the positive first principal invariants I_1. The shifting was demonstrated also by other works [21, 93]. Nonetheless, the failure function of Bier et al. [10, 11, 52] can be extrapolated towards the axis of the negative first principal invariants by means of the above mentioned self-written Python® script, including the parameter's values listed in Table 4.3. Fig. 4.27 shows the extrapolated curve with the experimental determined

failure data. The curve goes beyond the compressive failure data and it is related to the field of biaxial and triaxial compression tests, based on Shafiq et al. [93].

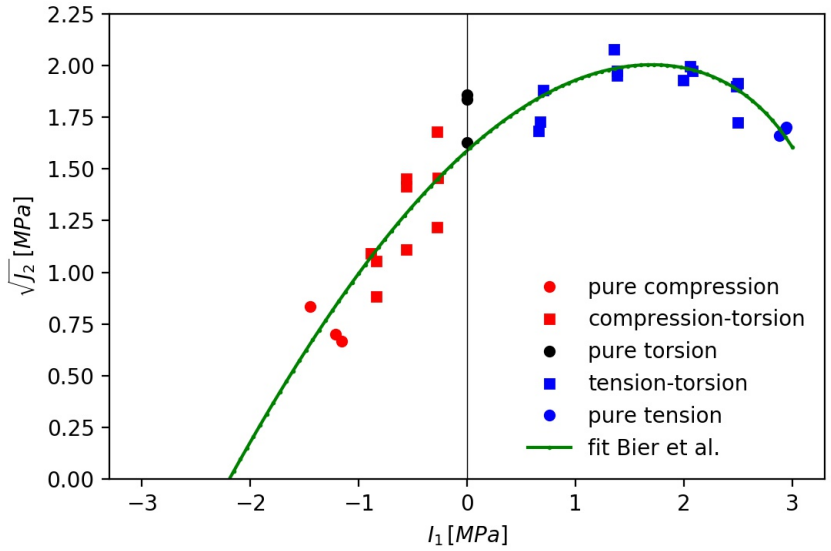

Figure 4.27: Extrapolation of the failure surface of Bier et al. [10, 11, 52] towards the axis of negative first principal invariants I_1 in order to equilibrate the shifting of the failure surface, according to Concas et al. [23].

Chapter 5

Conclusions

The present work deals with the experimental investigation of the mechanical properties of PVC foams through different methods, which were barely or never used on PVC foams.
The first part of this work was done at the Department of Mechanical, Chemical and Materials Engineering, University of Cagliari, Italy. It concerns the execution of compression tests, the application of the DIC technique for the strain measurement and the subsequent determination of the compressive modulus of the Divinycell® HP PVC foam grade with two different nominal densities (65 and 160 kg/m^3 for the HP60 grade and the HP160 grade, respectively). This was done consistently with other authors [16, 88, 123], who determined the compressive modulus of other PVC foam grades by averaging strains maps obtained by optical full-field non-contact methods. Strains were also calculated from displacement data of the actuator, i.e. for obtaining global strain values. The strain measurement method shows to be fundamental, since it draws to greatly different values of the compressive modulus. Therefore, the aim of the first part of this work was to find the reasons for the different compressive moduli obtained and which method would be the most reliable. Further sources of errors in evaluating the compressive modulus were described. For example, exhibiting a pseudo-elastic response, the compressive stress-strain curve has not a single slope, thus, based on the portion of the stress-strain diagram, the corresponding slope alters the determination of the compressive modulus. Further analyses involve the evaluation of the compliance and the calculation of strains from the DIC by considering eighteen small ROIs. The ROIs are positioned in different places over the whole surface of the specimen.
Concerning the compliance, the ASTM normative [25] recommends the calculation of the compressive modulus from displacement data after the elimination of the

compliance. Nonetheless, the reported tests demonstrate the negligible contribution of the compliance.

By calculating the strains from eighteen different ROIs, the inhomogeneity of the strain fields over the whole surface confirms the importance of distinguishing between local strains and global strains for PVC foams and, more broadly, any cellular materials. Hence, the compressive moduli should be determined only from global strain values, contrary to the method presented by the literature [16, 88, 123].

The second part of this work was done at the Chair of Applied Mechanics, Saarland University (Lehrstuhl für Technische Mechanik, Universität des Saarlandes), Germany and is described in the work of Concas et al. [23]. Uniaxial (tension, compression, torsion) and multiaxial (combined tension-torsion and combined compression-torsion) tests were performed on cylindrical specimens of the Divinycell® HP100 PVC foam grade for investigating the in-plane mechanical behaviour, which is not fully studied yet. Failure data and the elastic moduli, i.e. the Young's modulus, the compressive modulus and the shear modulus were calculated. Similarly to the work of Jung and Diebels [64, 65] relating aluminium foams, the yield function proposed by Bier et al. [10, 11, 52] appears to be suitable for fitting failure data of PVC foams, too. A methodology based on the 3D-DIC for the inspection of deformation bands during tests has been described, by mentioning all issues that have been encountered for improving the procedure. The method allows the monitoring of almost 360° of the specimen. Results of such a procedure are shown through local strain maps of three uniaxial tests, i.e. tension, compression and torsion, and two multiaxial tests, i.e. combined tension-torsion test and combined compression-torsion test, in which the uniaxial preload reaches 50% of the tensile failure load and the compression failure load, respectively. The analysis of local strain maps and, more precisely, deformation bands is essential for predicting the failure, as well as for the throughout understanding of the material behaviour. The presented method permits also to observe possible irregularities during the test, e.g. misalignment of the bushings. As might be expected, trends of deformation bands are greatly influenced by the buckling of the specimen, that occurs in uniaxial compression tests. Whereas for tensile tests deformation bands exhibit a slightly wavy trend in addition to a main deformation band perpendicular to the loading axis and positioned where the fracture of the specimen arises. For each loading case, in which the torsional load is involved, deformation bands are positioned in two diametrically opposite wedges of the specimen. This feature could not be observed by a stereoscopic system equipped with less than four pairs of cameras and is linked to the orthotropy of PVC

foam panels. Cells are elongated towards the through-thickness direction and the specimen axis is perpendicular to the through-thickness direction. Hence, both the longest and the shortest size of the foam cells can be found along the contour of the specimen round cross-section. Thus, there would be struts of the cells with different sizes that would deform by different magnitudes [23]. This leads to the gathering of deformation bands and higher strain gradients in two diametrically opposed wedges of the specimen. This feature is equally visible in torsion tests and combined tension-torsion tests and appears slightly attenuated in combined compression-torsion tests. From the above-mentioned considerations, the 3D-DIC by the 8-camera system is thus a valuable tool for investigating the deformation mechanism in multiaxial loading cases. Nevertheless, this method has still some drawback. It has been already mentioned that an adequate positioning of lamps is essential for an efficient correlation. But the positioning of light sources is demanding due to the experimental set-up and, especially, the cylindrical geometry of the specimen, which causes the presence of brighter areas and shadowed areas in the opposite side. Increasing the number of light sources, i.e. lamps would be detrimental because of the appearance of further glares. The only solution consists in putting the light sources far enough away from the 8-camera system, similarly to the distance of ceiling lights from the whole fixture.

Bibliography

[1] *Composite Materials Handbook. Volume 6. Structural Sandwich Composites*. SAE International, 2013.

[2] H Altenbach and VA Kolupaev. Classical and non-classical failure criteria. In *Failure and damage analysis of advanced materials*, pages 1–66. Springer, 2015.

[3] M Arcan, Z Hashin, and A Voloshin. A method to produce uniform plane-stress states with applications to fiber-reinforced materials. *Experimental Mechanics*, 18(4):141–146, 1978.

[4] MF Ashby, T Evans, NA Fleck, LJ Gibson, JW Hutchinson, and HNG Wadley. *Metal foams: a design guide*. Butterworth-Heinemann, 2000.

[5] Eric Greene Associates. Marine composites. core materials and adhesive. `http://www.ericgreeneassociates.com/images/Core_Materials_and_Adhesives.pdf`, 24-09-2018.

[6] C Atas and C Sevim. On the impact response of sandwich composites with cores of balsa wood and PVC foam. *Composite Structures*, 93(1):40–48, 2010.

[7] F Aymerich. Composite materials for wind turbine blades: issues and challenges. In *SYSWIND Summer School, University of Patras*, 2012.

[8] RS Ayyagari and M Vural. Multiaxial yield surface of transversely isotropic foams: Part I — Modeling. *Journal of the Mechanics and Physics of Solids*, 74:49–67, 2015.

[9] D Benderly and S Putter. Characterization of the shear/compression failure envelope of Rohacell foam. *Polymer Testing*, 23(1):51–57, 2004.

[10] W Bier, MP Dariel, N Frage, S Hartmann, and O Michailov. Die compaction of copper powder designed for material parameter identification. *International Journal of Mechanical Sciences*, 49(6):766–777, 2007.

[11] W Bier and S Hartmann. A finite strain constitutive model for metal powder compaction using a unique and convex single surface yield function. *European Journal of Mechanics-A/Solids*, 25(6):1009–1030, 2006.

[12] J Blaber, B Adair, and A Antoniou. Ncorr: open-source 2D digital image correlation matlab software. *Experimental Mechanics*, 55(6):1105–1122, 2015.

[13] J-S Blazy, A Marie-Louise, S Forest, Y Chastel, A Pineau, A Awade, C Grolleron, and F Moussy. Deformation and fracture of aluminium foams under proportional and non proportional multi-axial loading: statistical analysis and size effect. *International Journal of Mechanical Sciences*, 46(2):217–244, 2004.

[14] LG Brazier. On the flexure of thin cylindrical shells and other "thin" sections. *Proceding of the Royal Society of London A*, 116(773):104–114, 1927.

[15] M Burman and D Zenkert. Fatigue of foam core sandwich beams-1: undamaged specimens. *International journal of fatigue*, 19(7):551–561, 1997.

[16] MF Caliri Júnior, GP Soares, RA Angélico, R Canto Bresciani, and V Tita. Study of an anisotropic polymeric cellular material under compression loading. *Materials Research*, 15(3):359–364, 2012.

[17] LA Carlsson and GA Kardomateas. *Structural and failure mechanics of sandwich composites*. Springer Science & Business Media, 2011.

[18] F Chen, X Chen, X Xie, X Feng, and L Yang. Full-field 3D measurement using multi-camera digital image correlation system. *Optics and Lasers in Engineering*, 51(9):1044–1052, 2013.

[19] L Chen, D Rende, LS Schadler, and R Ozisik. Polymer nanocomposite foams. *Journal of Materials Chemistry A*, 1(12):3837–3850, 2013.

[20] X Chen, W Zhao, XL Zhao, and JZ Xu. Failure test and finite element simulation of a large wind turbine composite blade under static loading. *Energies*, 7(4):2274–2297, 2014.

[21] RM Christensen, DC Freeman, and SJ DeTeresa. Failure criteria for isotropic materials, applications to low-density types. *International Journal of Solids and Structures*, 39(4):973–982, 2002.

[22] M Colloca, G Dorogokupets, N Gupta, and M Porfiri. Mechanical properties and failure mechanisms of closed-cell PVC foams. *International Journal of Crashworthiness*, 17(3):327–336, 2012.

[23] F Concas, S Diebels, and A Jung. Multiaxial failure surface of PVC foams and monitoring of deformation bands by three-dimensional digital image correlation. *Submitted.*, 2018.

[24] Correlated Solutions, Inc. Minimizing noise and bias in 3D DIC. `http://www.correlatedsolutions.com/supportcontent/dic-noise-bias.pdf`, 24-09-2018.

[25] ASTM D1621-10. *Standard test method for compressive properties of rigid cellular plastics.* 2010.

[26] IM Daniel and J-M Cho. Characterization of anisotropic polymeric foam under static and dynamic loading. *Experimental mechanics*, 51(8):1395–1403, 2011.

[27] IM Daniel, JS Fenner, BT Werner, and J-M Cho. Characterization and modeling of polymeric foam under multi-axial static and dynamic loading. In *Experimental and Applied Mechanics, Volume 4*, pages 123–134. Springer, 2017.

[28] IM Daniel and EE Gdoutos. Failure modes of composite sandwich beams. In *Major Accomplishments in Composite Materials and Sandwich Structures*, pages 197–227. Springer, 2009.

[29] M Danielsson and JL Grenestedt. Gradient foam core materials for sandwich structures: preparation and characterisation. *Composites Part A: Applied Science and Manufacturing*, 29(8):981–988, 1998.

[30] Dantec Dynamics GmbH. Istra 4D Software Manual Q-4xx System. Manual Version: 2.8.5. Software Version: 4.4.4.459. 2016.

[31] JM Davies. *Lightweight sandwich construction*. Blackwell Science, 2001.

[32] VS Deshpande and NA Fleck. Multi-axial yield behaviour of polymer foams. *Acta materialia*, 49(10):1859–1866, 2001.

[33] DIAB. Divinycell® HCP Technical Data. http://www.diabgroup.com/en-GB/Products-and-services/Core-Material/Divinycell-HCP, 10-09-2018.

[34] DIAB. Divinycell® HP Technical Data. http://www.diabgroup.com/en-GB/Products-and-services/Core-Material/Divinycell-HP, 16-04-2018.

[35] DIAB. Divinycell® HT Technical Data. http://www.diabgroup.com/en-GB/Products-and-services/Core-Material/Divinycell-HT, 29-08-2018.

[36] DIAB. Divinycell® HP Technical Data, 2011. http://www.brenntag.com/media/documents/bsi/product_data_sheets/material_science/diab/divinycell_hp_pds.pdf, 24-09-2018.

[37] DIAB International AB. Guideline to Core and Sandwich. http://www.diabgroup.com/en-GB/Products-and-services/Core-Material, 29-08-2018.

[38] A Donnard, S Guérard, L Mahéo, P Viot, and G Rio. Multiaxial experiments with radial loading paths on a polymeric foam. *Polymer Testing*, 67:441–449, 2018.

[39] M Doyoyo and T Wierzbicki. Experimental studies on the yield behavior of ductile and brittle aluminum foams. *International Journal of Plasticity*, 19(8):1195–1214, 2003.

[40] RW Dyson. *Engineering polymers*. Springer Science & Business Media, 1991.

[41] EVONIK. Facing new challenges. Rohacell® for aviation and aerospace. http://www.rohacell.com/product/rohacell/en/markets/aviation-aerospace/, 29-08-2018.

[42] N-C Fahlbusch, W Becker, VA Kolupaev, and G Geertz. Nonlinear material behaviour and failure of closed-cell polymer foams. *Acta Mechanica*, 227(11):3113–3121, 2016.

[43] EE Gdoutos, IM Daniel, and K-A Wang. Multiaxial characterization and modeling of a PVC cellular foam. *Journal of Thermoplastic Composite Materials*, 14(5):365–373, 2001.

[44] EE Gdoutos, IM Daniel, and K-A Wang. Failure of cellular foams under multiaxial loading. *Composites Part A: Applied Science and Manufacturing*, 33(2):163–176, 2002.

[45] LJ Gibson and MF Ashby. *Cellular solids: structure and properties*. Cambridge University Press, 1999.

[46] LJ Gibson, MF Ashby, J Zhang, and TC Triantafillou. Failure surfaces for cellular materials under multiaxial loads—i. modelling. *International Journal of Mechanical Sciences*, 31(9):635–663, 1989.

[47] G Gioux, TM McCormack, and LJ Gibson. Failure of aluminum foams under multiaxial loads. *International Journal of Mechanical Sciences*, 42(6):1097–1117, 2000.

[48] J Graham-Jones and J Summerscales. *Marine applications of advanced fibre-reinforced composites*. Woodhead Publishing, 2016.

[49] RJ Green. A plasticity theory for porous solids. *International Journal of Mechanical Sciences*, 14(4):215–224, 1972.

[50] DIAB Group. GS Guidelines. Technical Center. `http://www.fiberglasssupply.com/pdf/core/GSGUIDELINES.pdf`, 24-09-2018.

[51] N Gupta. A functionally graded syntactic foam material for high energy absorption under compression. *Materials Letters*, 61(4-5):979–982, 2007.

[52] S Hartmann and W Bier. High-order time integration applied to metal powder plasticity. *International Journal of Plasticity*, 24(1):17–54, 2008.

[53] Z Hashin. Analysis of composite materials—a survey. *Journal of Applied Mechanics*, 50(3):481–505, 1983.

[54] L Herbeck, M Kleineberg, and C Schöppinger. Foam cores in RTM structures: manufacturing aid or high-performance sandwich? In *23rd SAMPE Europe International Conference, Paris*, 2002.

[55] P Hogg. Wind turbine blade materials. In *SUPERGEN Wind Phase 1 final Assembly, University of Loughborough*, 2010.

[56] MS Hoo Fatt. Composite sandwich structures for shock mitigation and energy absorption. Technical report, The University of Akron Akron United States, 2016.

[57] MS Hoo Fatt, AJ Jacob, X Tong, and A MacHado-Reyes. Crushing behavior and energy absorption of PVC foam: an anisotropic visco-elastic-plastic-damage model. *21st International Conference on Composite Materials, Xi'an, 20-25th August*, 2017.

[58] K Imielińska, L Guillaumat, R Wojtyra, and M Castaings. Effects of manufacturing and face/core bonding on impact damage in glass/polyester–PVC foam core sandwich panels. *Composites Part B: Engineering*, 39(6):1034–1041, 2008.

[59] FM Jensen, A Kling, and JD Sorensen. Change in failure type when wind turbine blades scale-up. In *5th Sandia Wind Turbine Blade Workshop, Albuquerque, NM, USA*, 2012.

[60] FM Jensen, PM Weaver, LS Cecchini, H Stang, and RF Nielsen. The Brazier effect in wind turbine blades and its influence on design. *Wind Energy*, 15(2):319–333, 2012.

[61] Z Jiang, K Yao, Z Du, J Xue, T Tang, and W Liu. Rigid cross-linked PVC foams with high shear properties: the relationship between mechanical properties and chemical structure of the matrix. *Composites Science and Technology*, 97:74–80, 2014.

[62] H Jin, W-Y Lu, S Scheffel, TD Hinnerichs, and MK Neilsen. Full-field characterization of mechanical behavior of polyurethane foams. *International Journal of Solids and Structures*, 44(21):6930–6944, 2007.

[63] P Johnson. Strain field measurements with dual-beam digital speckle photography. *Optics and lasers in engineering*, 30(3-4):315–326, 1998.

[64] A Jung and S Diebels. Yield surfaces for solid foams: A review on experimental characterization and modeling. *Special Issue: Experimental Solid Mechanics - Part II*, 41(2):e201800002.

[65] A Jung and S Diebels. Microstructural characterisation and experimental determination of a multiaxial yield surface for open-cell aluminium foams. *Materials & Design*, 131:252–264, 2017.

[66] A Jung, J Luksch, S Diebels, F Schäfer, and C Motz. In-situ and ex-situ microtensile testing of individual struts of Al foams and Ni/Al hybrid foams. *Materials & Design*, 153:104–119, 2018.

[67] A Jung, M Wocker, Z Chen, and H Seibert. Microtensile testing of open-cell metal foams—Experimental setup, micromechanical properties. *Materials & Design*, 88:1021–1030, 2015.

[68] LM Kachanov. *Foundations of the theory of plasticity*. North-Holland Publishing Co., Amsterdam, 1971.

[69] TH Kidd, S Zhuang, and G Ravichandran. In situ mechanical characterization during deformation of PVC polymeric foams using ultrasonics and digital image correlation. *Mechanics of Materials*, 55:82–88, 2012.

[70] PC Kim, DG Lee, IS Seo, and GH Kim. Low-observable radomes composed of composite sandwich constructions and frequency selective surfaces. *Composites Science and Technology*, 68(9):2163–2170, 2008.

[71] SJ Kim, JW Shin, H-G Kim, T-U Kim, and S Kim. The modified brazier approach to predict the collapse load of a stiffened circular composite spar under bending load. *Aerospace Science and Technology*, 55:474–481, 2016.

[72] A Kossa. A new biaxial compression fixture for polymeric foams. *Polymer Testing*, 45:47–51, 2015.

[73] S Laustsen, E Lund, L Kühlmeier, and OT Thomsen. Failure behaviour of grid-scored foam cored composite sandwich panels for wind turbine blades subjected to realistic multiaxial loading conditions. *Journal of Sandwich Structures & Materials*, 16(5):481–510, 2014.

[74] S-T Lee. *Foam extrusion: principles and practice*. CRC press, 2000.

[75] QM Li, RAW Mines, and RS Birch. The crush behaviour of Rohacell-51WF structural foam. *International Journal of Solids and Structures*, 37(43):6321–6341, 2000.

[76] GT Lim, V Altstädt, and F Ramsteiner. Understanding the compressive behavior of linear and cross-linked poly (vinyl chloride) foams. *Journal of Cellular Plastics*, 45(5):419–439, 2009.

[77] DD Luong, D Pinisetty, and N Gupta. Compressive properties of closed-cell polyvinyl chloride foams at low and high strain rates: Experimental investigation and critical review of state of the art. *Composites Part B: Engineering*, 44(1):403–416, 2013.

[78] H Mang and G. Hofstetter. *Festigkeitslehre*. Springer Verlag Wien GmbH, 2004.

[79] A May-Pat and F Avilés. Long term water uptake of a low density polyvinyl chloride foam and its effect on the foam microstructure and mechanical properties. *Materials & Design*, 57:728–735, 2014.

[80] L Mishnaevsky Jr and O Favorsky. Composite materials in wind energy technology. *Thermal to Mechanical Energy Conversion: Engines and Requirements, EOLSS Publishers: Oxford, UK*, 2011.

[81] A Miyase and SS Wang. Test method development and determination of three-dimensional stiffness properties of polyvinyl chloride structural foams. *Journal of Composite Materials*, 52(5):679–688, 2018.

[82] D Mohr and M Doyoyo. Analysis of the Arcan apparatus in the clamped configuration. *Journal of Composite Materials*, 36(22):2583–2594, 2002.

[83] D Mohr and M Doyoyo. A new method for the biaxial testing of cellular solids. *Experimental Mechanics*, 43(2):173–182, 2003.

[84] DRJ Owen and E Hinton. *Finite elements in plasticity: theory and practice*. Pineridge Press Limited, 1980.

[85] H Parkus. *Mechanik der festen Körper. 2. Auflage*. SpringerWienNewYork, 1966.

[86] L Peroni, M Avalle, and M Peroni. The mechanical behaviour of aluminium foam structures in different loading conditions. *International Journal of Impact Engineering*, 35(7):644–658, 2008.

[87] MS Rajput, M Burman, and S Hallström. Distinguishing between strain measurement procedures during compressive testing of foam materials. In *20th International Conference on Composite Materials Copenhagen, 19-24th July 2015*. International Committee on Composite Materials, 2015.

[88] MS Rajput, M Burman, J Köll, and S Hallström. Compression of structural foam materials–Experimental and numerical assessment of test procedure and specimen size effects. *Journal of Sandwich Structures & Materials*, page 1099636217690500, 2017.

[89] P Reu. All about speckles: aliasing. *Experimental Techniques*, 38(5):1–3, 2014.

[90] D Ruan, G Lu, LS Ong, and B Wang. Triaxial compression of aluminium foams. *Composites Science and Technology*, 67(6):1218–1234, 2007.

[91] RL Sadler, M Sharpe, R Panduranga, and K Shivakumar. Water immersion effect on swelling and compression properties of Eco-Core, PVC foam and balsa wood. *Composite Structures*, 90(3):330–336, 2009.

[92] M Sauceau, J Fages, A Common, C Nikitine, and E Rodier. New challenges in polymer foaming: A review of extrusion processes assisted by supercritical carbon dioxide. *Progress in Polymer Science*, 36(6):749–766, 2011.

[93] M Shafiq, RS Ayyagari, M Ehaab, and M Vural. Multiaxial yield surface of transversely isotropic foams: Part II — Experimental. *Journal of the Mechanics and Physics of Solids*, 76:224–236, 2015.

[94] AH Shi, GC Zhang, HT Pan, ZL Ma, and CH Zhao. Preparation and properties of rigid cross-linked PVC Foam. In *Advanced Materials Research*, volume 311, pages 1056–1060. Trans Tech Publ, 2011.

[95] H Shima, M Sato, and S-J Park. Suppression of Brazier effect in multilayered cylinders. *Advances in Condensed Matter Physics*, 2014, 2014.

[96] A Siriruk, YJ Weitsman, and D Penumadu. Polymeric foams and sandwich composites: Material properties, environmental effects, and shear-lag modeling. *Composites Science and Technology*, 69(6):814–820, 2009.

[97] J Sloan. Core for composites: Winds of change, 2010. `http://www.compositesworld.com/articles/core-for-composites-winds-of-change`, 24-09-2018.

[98] R Stewart. At the core of lightweight composites. *Reinforced Plastics*, 53(3):30–35, 2009.

[99] G Stoilov, V Kavardzhikov, and D Pashkouleva. A comparative study of random patterns for digital image correlation. *Journal of Theoretical and Applied Mechanics*, 42(2):55–66, 2012.

[100] FC Stoll. Optimal design of sandwich core for wind turbine blade buckling resistance. In *32nd ASME Wind Energy Symposium*, page 0175, 2014.

[101] MA Sutton, JJ Orteu, and H Schreier. *Image correlation for shape, motion and deformation measurements: basic concepts, theory and applications*. Springer Science & Business Media, 2009.

[102] Swarthmore College. Basic filters. `https://www.swarthmore.edu/NatSci/mzucker1/e27_s2016/filter-slides.pdf`, 03-06-2018.

[103] VL Tagarielli, VS Deshpande, and NA Fleck. The high strain rate response of PVC foams and end-grain balsa wood. *Composites Part B: Engineering*, 39(1):83–91, 2008.

[104] ST Taher, JM Dulieu-Barton, and OT Thomsen. Compressive behavior of PVC foam in elevated temperature using digital image correlation and a modified Arcan fixture. In *Proc., 19th Int. Conf. on Composite Materials (ICCM), Canadian Association for Composite Structures and Materials, Boucherville, QC, Canada*, 2013.

[105] ST Taher, OT Thomsen, and JM Dulieu-Barton. Characterization of compressive properties of polymer foam materials using DIC and a modified Arcan fixture. In *Imaging Methods for Novel Materials and Challenging Applications, Volume 3*, pages 249–254. Springer, 2013.

[106] ST Taher, OT Thomsen, JM Dulieu-Barton, and S Zhang. Determination of mechanical properties of PVC foam using a modified Arcan fixture. *Composites Part A: Applied Science and Manufacturing*, 43(10):1698–1708, 2012.

[107] OT Thomsen. Sandwich materials for wind turbine blades - present and future. *Journal of Sandwich Structures & Materials*, 11(1):7–26, 2009.

[108] H Toftegaard and A Lystrup. Design and test of lightweight sandwich T-joint for naval ships. *Composites Part A: Applied Science and Manufacturing*, 36(8):1055–1065, 2005.

[109] TC Triantafillou, J Zhang, TL Shercliff, LJ Gibson, and MF Ashby. Failure surfaces for cellular materials under multiaxial loads—II. Comparison of models with experiment. *International Journal of Mechanical Sciences*, 31(9):665–678, 1989.

[110] SW Tsai and EM Wu. A general theory of strength for anisotropic materials. *Journal of Composite Materials*, 5(1):58–80, 1971.

[111] University of Auckland. Gaussian filtering. `https://www.cs.auckland.ac.nz/courses/compsci373s1c/PatricesLectures/Gaussian%20Filtering_1up.pdf`, 03-06-2018.

[112] University of Colorado Boulder. Review of continuum mechanics: field equations, 2018. `https://www.colorado.edu/engineering/cas/courses.d/NFEM.d/NFEM.Ch08.d/NFEM.Ch08.pdf`, 24-09-2018.

[113] DR Veazie, KR Robinson, and K Shivakumar. Effects of the marine environment on the interfacial fracture toughness of PVC core sandwich composites. *Composites Part B: Engineering*, 35(6-8):461–466, 2004.

[114] PS Veers, TD Ashwill, HJ Sutherland, DL Laird, DW Lobitz, DA Griffin, JF Mandell, WD Musial, K Jackson, M Zuteck, A Miravete, SW Tsai, and JL Richmond. Trends in the design, manufacture and evaluation of wind turbine blades. *Wind Energy: An International Journal for Progress and Applications in Wind Power Conversion Technology*, 6(3):245–259, 2003.

[115] C Voglis and IE Lagaris. A rectangular trust region dogleg approach for unconstrained and bound constrained nonlinear optimization. In *WSEAS International Conference on Applied Mathematics*, page 7, 2004.

[116] T Walz. Review of the state of the art of whole field optical measurement techniques for strain analysis. In *Seventh International Symposium on Precision Engineering Measurements and Instrumentation*, volume 8321, page 832145. International Society for Optics and Photonics, 2011.

[117] P Wang, F Pierron, and OT Thomsen. Identification of material parameters of PVC foams using digital image correlation and the virtual fields method. *Experimental Mechanics*, 53(6):1001–1015, 2013.

[118] Y Wang and AM Cuitiño. Full-field measurements of heterogeneous deformation patterns on polymeric foams using digital image correlation. *International Journal of Solids and Structures*, 39(13-14):3777–3796, 2002.

[119] H-S Yu. *Plasticity and geotechnics*, volume 13. Springer Science & Business Media, 2007.

[120] J Yu, L Song, F Chen, P Fan, L Sun, M Zhong, and J Yang. Preparation of polymer foams with a gradient of cell size: further exploring the nucleation

effect of porous inorganic materials in polymer foaming. *Materials Today Communications*, 9:1–6, 2016.

[121] M Zaslawsky. Multiaxial-stress studies on rigid polyurethane foam. *Experimental Mechanics*, 13(2):70–76, 1973.

[122] D Zenkert and J Bäcklund. PVC sandwich core materials: mode I fracture toughness. *Composites science and technology*, 34(3):225–242, 1989.

[123] S Zhang, JM Dulieu-Barton, RK Fruehmann, and OT Thomsen. A methodology for obtaining material properties of polymeric foam at elevated temperatures. *Experimental Mechanics*, 52(1):3–15, 2012.

[124] Z Zhou, Z Wang, L Zhao, and X Shu. Uniaxial and biaxial failure behaviors of aluminum alloy foams. *Composites Part B: Engineering*, 61:340–349, 2014.

[125] OC Zienkiewicz and RL Taylor. *The Finite Element Method. Volume 2: Solid Mechanics*. Butterworth-Heinemann, 2000.